The University Of Sheffield.

The Effect of Surface Roughness and Free Stream Turbulence on the Flow and Heat Transfer around a Circular Cylinders.

Student:
Ahmed Al-Rubaiy

Supervisor:
Dr. Robert Woolley

Dissertation Submitted to the Department of Mechanical Engineering,

University of Sheffield in partial fulfilment of the requirements for the

Degree of

Doctor of Philosophy

April 9, 2018

Abstract

Given the significance of numerous practical applications in thermo-fluid mechanics for circular cylinders in cross-flow and the lack of research on the effect of surface's roughness and free-stream turbulence on heat transfer from cylinders in cross-flow, a study on these effects is necessary. This work aims to gain a deeper understanding of the individual and common effects of roughness and turbulence intensity on the boundary layers around the cylinder and their effects on local and total heat transfer enhancement. For that purpose, wind-tunnel experiments were used with four levels of surface's roughness ($0 < \epsilon/D \leqslant 7.25x10^{-3}$) and different levels of turbulence intensity (2.2% - 9.7%).

The Reynolds number was varied at a range of $16000 \leqslant Re \leqslant 87000$. The test cylinder had an outer diameter of 50 mm and a length of 100 mm, producing an aspect ratio ($L/D = 2$) in the cross-flow direction and a blockage ratio ($D/B = 0.4$). A hot wire anemometer system was used to perform the velocity field measurements and to obtain the mean and fluctuating velocity information. A micro-foil heat flux sensor was used to measure local heat flux. The study also extended to creating a surface temperature map using an IR thermal camera.

From the results, it has been found that the boundary layers around the cylinder are most strongly influenced by free-stream turbulence and surface roughness which play an essential role in enhancing thermal performance by increasing turbulence in the boundary layer. The existence of these two factors augmented the heat transfer, but the surface roughness had a greater influence than the free stream turbulence. The value of the critical Reynolds number was also affected where it decreased according to surface roughness and/or free stream turbulence values. Combining the effects of roughness and turbulence intensity led to multiplying the heat transfer; an increase of turbulence intensity from 2.2% to 9.7% resulted in an 80% increase in the mean heat transfer at Re= $7.5x10^4$ at the high surface roughness ($\epsilon/D = 7.25x10^{-3}$).

Acknowledgements

I would like to acknowledge the following people for their support and guidance during my doctoral study and writing of this dissertation at ˝The University of Sheffield˙, Sheffield, UK.

First of all, I would like to thank my supervisor: Dr Robert Woolley, who accepted to supervise this dissertation. His teaching, patience, and encouragement throughout my doctoral study were invaluable.

I would like to extend my gratitude to everyone in the department who have aided this study, particularly to the technician Mr Oliver P Cooper for his assistance me during my research.

Furthermore, I would like to thank all colleagues of the university for contributing to such an inspiring and pleasant atmosphere.

I would also like to acknowledge the Iraqi government, Ministry of Higher Education and Scientific Research, and The University of Diyala, for supporting my tuition and fees during this research work.

Away from work, special thanks go to my best friends Mohammed Yaseen and Zaid Emad, for helping me get through the difficult times, and for all the support, and care they provided.

Finally, I am very grateful to the support and encouragement from my family in Iraq, very great appreciation to my elder brother for always being there for me as a friend as well as my deep and sincere gratitude to my wife Hanan Al-Zinkee, my son Ayman and my sweet daughter Rawan for their continuous and unparalleled love, help and support. You should know that your support and encouragement was worth more than I can express on paper.

Contents

List of Figures

Page

List of Tables

Page

Nomenclature

List of Abbreviations:

Symbol	Description	Definition	Units
Fsp	Front Stagnation Point	–	–
FST	Free Stream Turbulence	–	–
Rsp	Rear Stagnation Point	–	–

Greek Symbols:

Symbol	Description	Definition	Units
α	Thermal diffusivity	$\frac{\kappa}{\rho c_p}$	m^2/s
β	Blockage ratio	$\frac{H}{D}$	1
δ	Hydrodynamic boundary-layer thickness	–	m
δ_1	Displacement thickness	–	m
δ_2	Momentum thickness	–	m
δ_T	Thermal boundary later thickness	–	m
ϵ	Surface roughness	–	m
η	Distance normal to and measured from the surface of the circular cylinder	–	m
κ	Thermal conductivity	–	W/mK
λ	Wavelength	–	nm
μ	Dynamic viscosity		Ns/m^2
ν	Kinematic viscosity	–	m^2/s
ω	Pressure gradient parameter	–	–
ρ	Density	–	kg/m^3
σ	Stefan Boltzmann constant	–	$W/(m^2K^4)$
τ	Shear Stress	–	N/m^2
θ	Angular position	–	deg
v	η-component of velocity in the boundary layer	–	m/s

ε	Surface emissivity	–	1

Latin Symbols:

Symbol	Description	Definition	Units
$\bar{p}$	Pressure coefficient	$\frac{2(p_\theta - p_\infty)}{\rho u_\infty^2}$	1
D	Cylinder diameter	–	m
p_∞	Static pressure of free stream	–	N/m^2
q	Heat flux	–	W/m^2
T_f	Film temperature	$\frac{T_s + T_\infty}{2}$	K
AR	Aspect ratio cylinder	$\frac{L}{D}$	1
$\acute{u}$	Turbulent Fluctuation	–	–
$\bar{u}$	Turbulence Strength	u_{rms}	m/s
λ_x	Dissipation length scale	–	m
A_s	Surface area	–	m^2
C_D	Drag coefficient	$\frac{F_D}{\frac{1}{2}\rho u^2 A}$	1
C_f	Skin drag coefficient	$\frac{2\tau_w}{\rho U_\infty^2}$	$--$
c_p	Specific heat of the fluid	–	J/kgK
C_P	Pressure coefficient	$\frac{2\Delta P}{\rho U_\infty^2}$	$--$
C_{Df}	Friction drag coefficient	–	$--$
F	Frequency of vortex shedding	–	Hz
F_D	Drag force	–	N
H	Test section height	–	m
h	Forced convection heat transfer coefficient		W/m^2K
I	Current	–	A
IR	Infrared band	–	–
L	Length of the cylinder	–	m
L_D	Hydraulic diameter	–	m

L_x	Turbulent length scale	–	m
Nu	Nusselt number	$\frac{hD}{k}$	1
Nu_θ	Local Nusselt number	–	1
p_θ	Local pressure on cylinder surface	–	N/m^2
P_e	Electrical power	–	W
Pr	Prandtl number	$\frac{\mu C_p}{\kappa}$	1
Q_L	Local heat transfer	–	W
Q_{Cond}	Conduction heat transfer	–	W
Q_{Conv}	Convection heat transfer	–	W
Q_{Rad}	Radiation heat transfer	–	W
Q_{tot}	Total heat transfer(heat losses)	–	W
Re	Reynolds number	$\frac{UD}{v}$	1
Re_c	Critical Reynolds number	–	1
s	Distance along the curved surface of the circular cylinder measured from the forward stagnation point	–	m
S_t	Strouhal number	$\frac{fL_D}{u}$	1
t	Time	–	s
T_s	Surface temperature	–	K
T_u	Turbulence Intensity	$T_u = \frac{\bar{u}}{U_{mean}}$	%
T_∞	Free-stream temperature	–	K
u	Longitudinal velocity	–	m/s
u	s-component of velocity in the boundary layer	–	m/s
U_∞	Approach velocity	–	m/s
$U_{(o)}$	Potential flow velocity just outside the boundary layer	$= 2U_\infty \sin\theta$	m/s
U_{mean}	Mean velocity	–	m/s

UV	Ultraviolet band	–	–
V	Voltage	–	V
v	Vertical velocity	–	m/s

Subscripts:

Symbol	Description	Definition	Units
∞	Free stream conditions (main flow)		
$Cond$	Conduction		
$Conv$	Convection		
f	Film condition		
L, θ	Local condition		
Rad	Radiation		
s	Surface, wall		

CHAPTER 1

Introduction

1.1 Introduction

The fluid flow over cylinder is one of the most important classic problems in thermo-fluid mechanics and has been well examined due to its widespread occurrence in various applications and in many forms. The circular cylinder structure can be used in groups and alone in heat exchange equipment, gas compressors, gas or steam turbines, and different turbo-machinery and aerodynamic systems.

A comprehensive understanding of the flow dynamics around the cylinders, like separation of the thermal boundary layers, the wake region, the free shear layer, and vortices dynamics, is further complicated, especially with interactions between the shear layers and Karman vortex [1]. The problem is made more complex by many formations resulting from different flow patterns and the result of their interactions. There are several environmental factors that can affect the boundary layers' development around circular cylinders, such as various surface irregularities (roughness), free-stream turbulence, and acoustics. When the levels of these circumferential impacts are not large, the developing process is well recognized by the (normal) transition sequence, including the laminar separation bubble, laminar turbulent separation, turbulent transition, shear layer, and Karman instabilities.

Most of the published research is concerned with the influence of geometric cylinder parameters on overall or local heat transfer coefficients, and drag coefficients. Some researchers were interested in the flow direction (angle of attack) and others in the effects of oscillatory flow (free stream turbulence) on the boundary layer. Free stream turbulence and cylinder roughness have been identified as the major causes of travelling and stationary flow instability. There are also signs that interaction between these two factors may meaningfully influence flow disturbance development that leads to enhancing heat transfer.

At the early stages of flow measurements, researchers utilised various techniques in data recording. For the last two decades, a great deal of on-line data acquisition systems, like infra-red (IR) systems, have been developed for computers . Such systems contribute to forming the data-base for boundary-layer research and give important information regarding the understanding of the heat transfer and flow behaviour in the heat exchange systems. However, although there is a great deal of research, factors that affect thermal boundary layers are not completely understood. Some of these factors are free-stream turbulence, surface roughness, wall temperature, pressure gradient, blockage ratio, and even the local Mach number. Therefore, this study has focused on the two most important factors: free stream turbulence and surface roughness.

1.2 Motivation for this study

Although wall roughness is a defining feature in many practical fluid engineering applications, most of the research on boundary layers has focused on smooth walls. Both experimental technicalities and numerical methodologies have been used to examine the outstanding features of boundary layer flow around smooth cylinders. Surface roughness in boundary layers and free stream levels have been observed to cause a considerable modification of the flow structure and turbulent transport phenomena in the region close to the roughness elements. These modifications may include enhanced mass, heat, and momentum transfer. However, the impacts of roughness and free-stream turbulence (FST) on separated and reattached flows are not well understood.

1.3 Objective and scope of research

The objective of this experimental study is to obtain a better understanding of flow and heat transfer around a circular cylinder. This understanding will allow for a clear interpretation of boundary layers analysis and heat transfer efficiency in this complex flow and will provide answers to questions regarding the importance of free-stream turbulence and surface roughness in heat transfer enhancement. The main purpose of the present study is to investigate the impact of turbulence level (FST) and wall roughness at different Re numbers ($1.6x10^3$ - $8.7x10^4$) on flow field and on the boundary layer around circular cylinders.

This objective was achieved using an experimental methodology. Specifically, local surface temperature and local heat flux around the cylinder were measured over four levels of wall roughness (smooth, fine, middle, and rough) with different level of turbulence in the free stream (2.2% - 9.7%). Particular emphasis has been placed on the interaction between free stream turbulence and the flow field in the wake region. In addition, the study extends to investigate the surface temperature distribution map of cylinders. A novel technique (IR thermal camera) was used for that purpose.

Hot Wire Anemometer system was employed to measure mean velocities and turbulent intensities, Heat Flux Sensor was used to calculate local heat transfer coefficient and thermocouples was used to perform the temperature measurements.

Briefly, the study focused on heat transfer from the smooth cylinder, then the effect of turbulence intensity and the roughness together and individually on local and overall heat transfer from the circular cylinder.

CHAPTER 2

Background, Experimental Evidence

2.1 Theoretical Background

2.1.1 Flow across a circular cylinder

The hypothesis of an ideal fluid depends on the probability of slip between the fluid and the surface without internal friction between boundary layers (the absence of the boundary layer). The velocity distribution of an ideal fluid across a cylinder is represented by [2]:

$$U(o) = U_{\infty}(sin\theta)[1 + (\frac{R_o}{R})^2] \tag{2.1}$$

where R_o is the distance from the cylinder axis to its surface, R is the distance from the cylinder axis to the point considered, and u_{∞} is the main velocity. It is clear that the tangential velocity u_x declines with the distance from the surface and reaches its maximum amount on the surface of the cylinder ($R = R_o$):

$$U(o) = 2U_{\infty}sin\theta \tag{2.2}$$

It is obvious that the velocity is zero at the front and rear stagnation points and maximum value at $\theta = 90^o$. The velocity is relating the longitudinal pressure gradient by the Euler equation:

$$-\frac{dp}{dx} = \rho u \frac{du}{dx} \tag{2.3}$$

The value of the pressure distribution on the cylinder surface is determined by substitution of (2.2) into (2.3):

$$P = \frac{p_{\theta} - p_{\infty}}{\rho U_{\infty}^2/2} = 1 - 4sin^2\theta \tag{2.4}$$

where p_{∞} is the static pressure in the channel.

Equation (2.4) suggests that pressure is inversely proportional to velocity, and pressure has a maximum value at stagnation points and a minimum at the central section. A result of asymmetrical pressure distribution around the cylinder surface, Figure 2.1, the cylinder offers no resistance to the flow of an ideal fluid and thus a zero value for the force on the cylinder. The real fluids case is different where the pressure distributions are non-symmetrical because of the influence of viscosity. The non-symmetrical pressure distribution brings a net force on the cylinder and this force has the substantial impact on the pressure drop across the cylinder and the viscous interaction of the fluid and the cylinder surface is the main cause of existence the boundary layer, more details in Appendix A.

2.1.2 The initial system of governing equations

The fluid dynamics and heat transfer in a steady, and two-dimensional boundary layer are governed by the following partial differential equations [2]:

Continuity:

$$\frac{\partial(\rho u)}{\partial x} + \frac{\partial(\rho v)}{\partial y} = 0 \tag{2.5}$$

Momentum:

$$\rho\left(u\frac{\partial u}{\partial x} + v\frac{\partial u}{\partial y}\right) = \frac{\partial \tau}{\partial y} - \frac{\partial p}{\partial x} \tag{2.6}$$

Energy:

$$c_p\rho\left(u\frac{\partial T}{\partial x} - v\frac{\partial T}{\partial y}\right) = \frac{\partial q}{\partial y} \tag{2.7}$$

with the boundary conditions which are corresponding to an isothermal surface, i.e.:

$$u = v = o,\ T = T_s \quad at\ y = 0 \tag{2.8}$$

$$u = u_\infty,\ T = T_\infty \quad at\ y = \infty \tag{2.9}$$

Where the x and y denote the horizontal and vertical coordinates, respectively, and u and v denote the horizontal and vertical fluid velocities, respectively, and T is the temperature. Further details can be found in Appendix A.

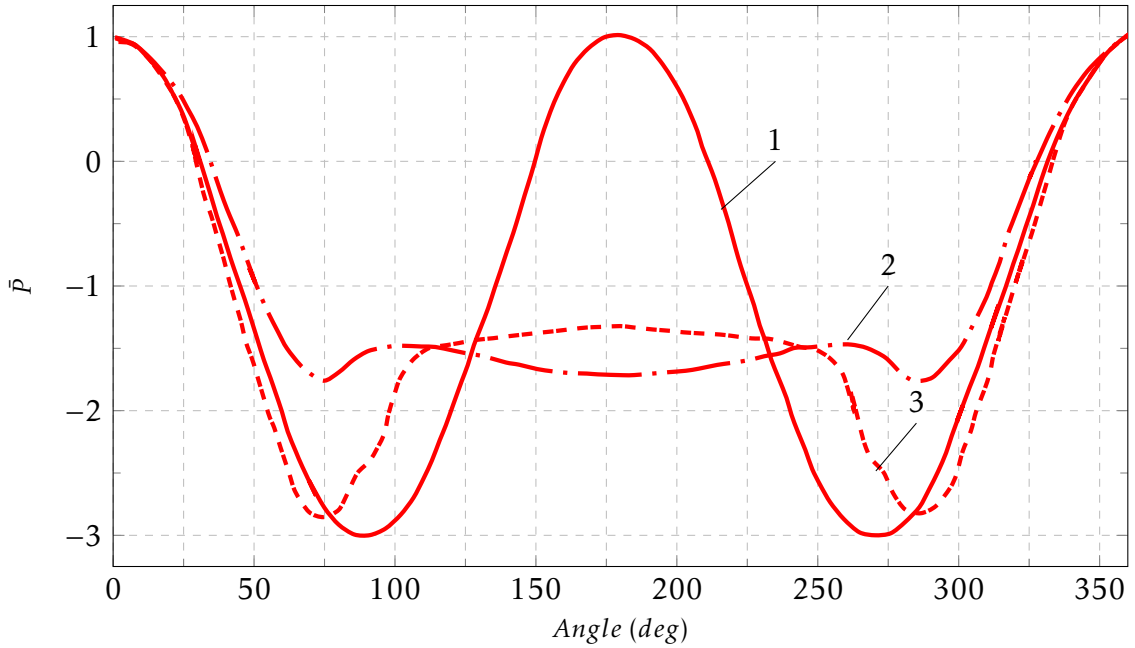

Figure 2.1: Pressure distribution around circular cylinder: 1- potential flow (analysis); 2- subcritical flow of air ($Re = 8x10^4$) (experiment); 3- critical flow of water ($Re = 2x10^5$) (experiment) [2].

2.2 Fluid Flow and Heat Transfer Characteristics

The flow rate plays a key role in the nature of flow around the cylinders as they where both the location of the flow separation from the cylinder surface and position of laminar-turbulent transition point depend on the Reynolds number. Figures 2.2 and 2.3 show the interaction between a cylinder surface and a fluid flow. The flow rate passes through four ranges: the sub-critical, the critical, the super-critical and the trans-critical regimes (see Figure 2.4), which are characterized by a unique boundary-layer behaviour. With an increase in the Reynolds number, the drag coefficient rapidly drops because the separation point shifts downstream. This range is termed the critical flow regime and Re_{cr} is denoted the critical Reynolds number when the drag coefficient shows a minimum value.

The flow pattern around the cylinders in cross flow significantly affects heat transfer. The variation in the local Nusselt number (Nu_θ) around the surface of a cylinder in cross flow has been determined [3] and is shown in Figure 2.5. On the x axis is the angular position around the cylinder. For all Reynolds numbers, the Nusslet number is high at 0^o where a stagnation point is formed as the flow meets the surface. At sub-critical flow, as the angle increases, Nu decreases due to the thickening of the laminar boundary layer. The Nusselt number reaches a minimum between 80^o and 90^o, then (Nu_θ) rises with increasing θ because of the extreme mixing in the wake region (the separated flow) [2, 3]. The point of separation

is identified from the graph of local heat transfer where Nu numbers reach the first minimum value. Following this point, the local Nu number grows due to the extensive turbulence that occurs over the rear half of the cylinder.Nonetheless, at sub-critical flow, the local Nu number over the front part is larger than the rear part and increases with Reynolds numbers, which happens due to the fact that the swirls recirculate some portions of the heated fluid [2, 4, 5]. **Zukauskas** [2] reported that the zone beyond the cylinder consists initially of separated boundary layers then vortices which rotate in the same location or are shed orderly from the surface and thus exhibit vortex street phenomenon. **Zijnen** [6] demonstrated the weak adoption of the average Nu number from the rear half of the cylinder on the Reynolds number and suggested the linear relationship ($Nu = 0.001Re$) to determine Nu.

At the critical flow, the boundary layer slips laminarly until θ reaches about 110^o where the flow changes significantly. The laminar boundary layer separates at this point to form a free shear layer (see Figure 2.2), which promptly transits downstream to turbulent flow. Lastly, the free shear layer re-attaches to the surface, which are manifested as separation bubbles which help to improve the heat transfer due to the increased exchange of the mainstream to the surface. The separation point moves downstream to the angular position $\theta = 140$ which leads to a significant gaining of the static pressure in the rear half then reduce the drag coefficient. At the same time, the local heat transfer rate gradually increases beyond separation point [7].

In the super-critical flow range, the drag coefficient grows up again (see Figure 2.4). the separation bubbles area disappear, and the laminar boundary layer direct transit to the turbulent. With further increasing Reynolds number (trans-critical flow), the laminar- turbulent transition displace on the front half causing the separation point moves upstream and increase the drag force.

Many studies focused on the relationship between heat transfer rate and mass flow rate [7–13]. **Sanitjai and Goldstein** [11], **Buyruk** [12] and **Zukauskas** [7] reported an upstream shifting of the location of minimum Nu as well as an increase in local and overall Nu when Re is increased, while some studies [8–10] indicated that the second minimum point was a result of the re-attaching shear layer in the wake area as part of the laminar boundary layer nature. **Kraabel et al.** [9] found that, at laminar flow (sub-critical), the free shear layer might reattach. The periodic swirls did not become fully turbulent, and the swirl - forming zone was away from the rear cylinder surface. Thus, the influences of the re-attached periodic swirls and free shear layer on heat transfer were comparatively weak. Additionally, he clarified that the turbulent shear layers that accompanied larger Re numbers gave higher mixing than the laminar shear layers that accompanied low Re numbers. The measurements of **Sanitjai and Goldstein** [11] showed an increase in convection heat transfer from the rear half, especially the rear stagnation point (Rsp) of the cylinder, compared to the front half, and **Norberg** [13] found that the mixing and turbulence at the back of the

cylinder increase with Re.

Flow and pressure measurements on smooth and rough cylinders for the sub-critical up to super-critical Re number range were covered in numerous studies [14–24]. By analogy, the studies at high Re numbers (trans-critical regime) were moderately rare [17, 24–32]. Since it was hard to build up the required flow conditions for the trans-critical regime in a wind tunnel, in the greater part of these investigations, either the velocity of the flow was very high and, therefore, compressibility impacts were included [28] or the diameter of the cylinder was extremely large, which increased the effect of the blockage ratio (D/H). This brought about a wide scatter in the measured information such as pressure coefficient, drag coefficient, and Strouhal number [24].

With the beginning of boundary layer studies, the impacts of blockage ratio on both the fluid dynamics and heat transfer from cylinders under various thermal boundary conditions have been the subject of several investigations [2,7,12,33,34].

Buyruk et al. [12] examined the effect of the blockage of a single tube in the tunnel. They predicted that the local heat transfer coefficient and pressure distributions would change dramatically for blockage ratios more than 0.7, and the average Nusselt number increases by about 10 % when the blockage ratio increases from 0.131 to 0.5, while **Peller** [34] suggested that the increasing in heat transfer about 23 % which is an appropriate average of various workers ($\Delta Nu/Nu_{\beta=0} = 0.23$). **West and Apelt** [33], examined the impacts of differing the aspect ratio (L/D) and blockage ratio on pressure distributions. They observed that the significant distortion for the flow accompanies blockage ratio more than 16% and a decrease in aspect ratio influences the pressure coefficient, however, blockage ratio has the greater effect compared with aspect ratio. **Zukauskas, and Ziugzda** [2], correlated the effects of channel blockage and different free-stream geometries on the flow profile and heat transfer region around the circular cylinders. They have expressed the distribution of velocity outside the boundary layer in terms of blockage ratio to evaluate the distribution of heat transfer. **Zukauskas and others** [7] reported that increasing the channel blockage from 0 to 80% prompted the separation point to move downstream to $\theta = 100^o$, and the minimum pressure to be migrated from $\theta = 70^o$ to 90^o. Their theoretical calculations showed that increase the blockage ratio lead to increase the heat transfer from the frontal half of the cylinder.

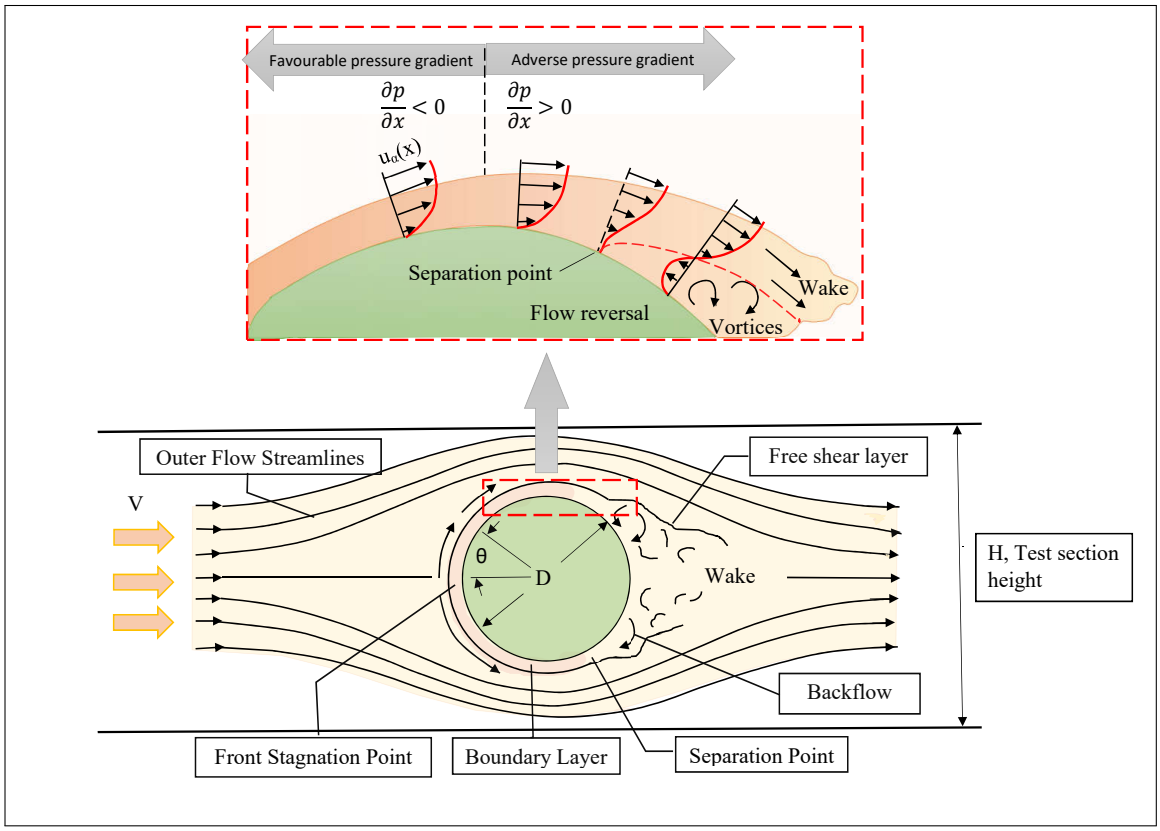

Figure 2.2: Boundary layer formation and separation around a circular cylinder [35].

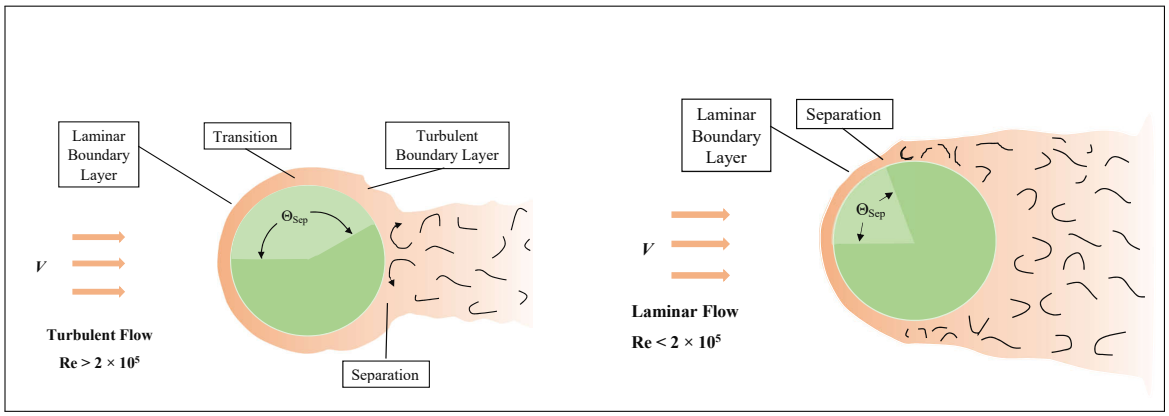

Figure 2.3: The effect of flow rate on separation [36].

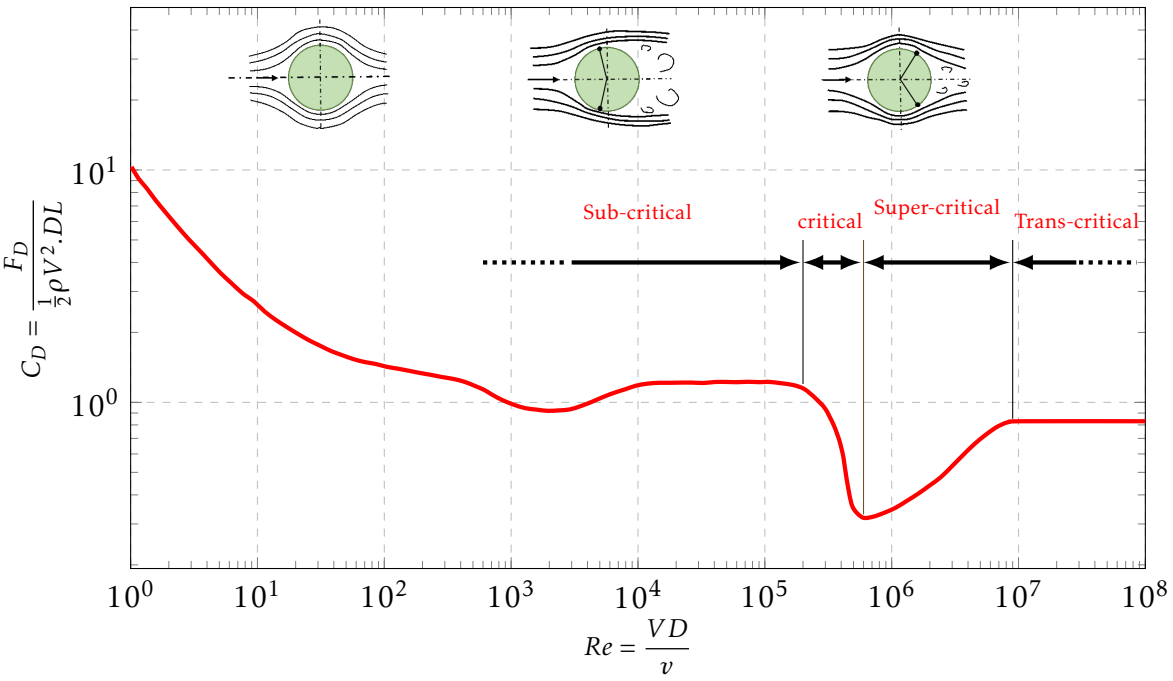

Figure 2.4: The hydraulic drag coefficient as a function of the Tu. [2].

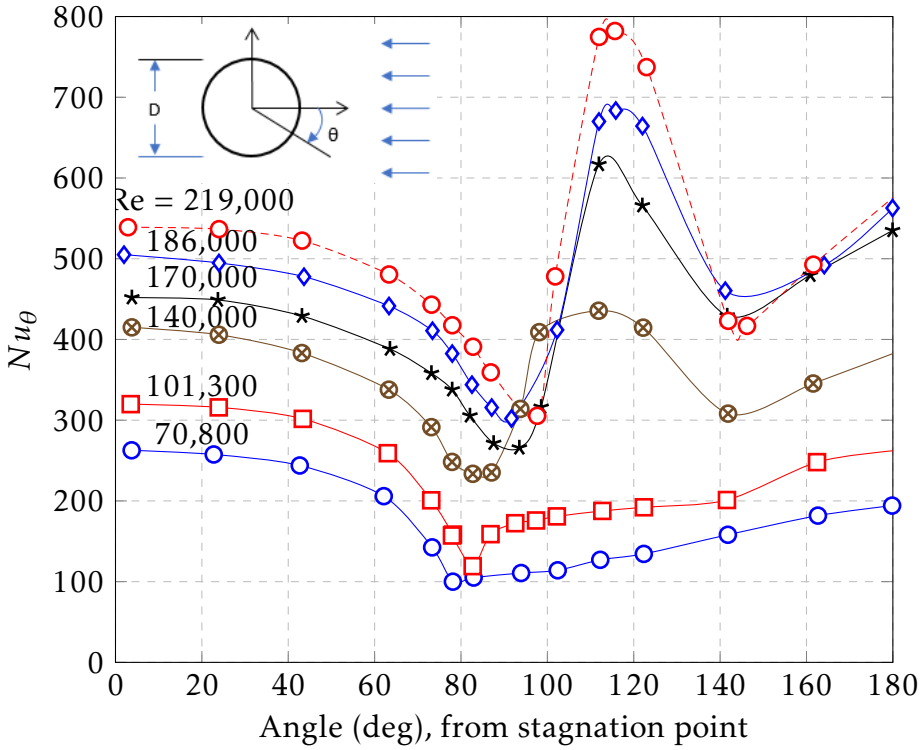

Figure 2.5: Difference of the local heat transfer coefficient over the circumference of a circular cylinder in cross flow of air [3].

2.2.1 Effect of Free-Stream Turbulence and Surface Roughness

Laminar-turbulent transition does not take place concurrently in all areas around a circular cylinder, but a series of transitions occur over a wide range of local Re numbers. The transition flow relies on the upstream velocity distribution, surface roughness, surface geometry, surface temperature, and the fluid kind, among others, and primarily on mainstream velocity [36, 37]. The heat exchange between a cylinder and the flow around it can be increased by augmenting the disturbance in the thermal boundary layer, which is considered as the first reason for heat transfer resistance. This disturbance might have occurred either by an external effect, such as increasing FST, or by an increase in the internal turbulence in the boundary layer itself through roughening of the cylinder surface. The existence of optimal geometries of the roughness elements on the heat transfer surface may even prompt the entire destruction of the boundary layer [2, 38]. Only two of the most common disturbances in practical usage will be debated in this section: turbulence intensity FST and surface roughness. Figure 2.6 and Figure 2.7 show the effect of turbulence level of mainstream and surface roughness ,respectively, on the coefficient of drag.

2.2.1.1 Effect of Free-Stream Turbulence

The turbulence in the main stream is described by three parameters: T_u turbulence intensity, L_x turbulence scale and T_f frequency spectrum of random velocity fluctuations. The affecting factors T_u and L_x affect various transition states in a various way. In most practical uses, the main stream is turbulent, however most of the research has been accomplished in wind tunnels free of turbulence. Low levels of disturbance can impact significantly in several transition conditions. The dominant factor is T_u turbulence intensity and L_x turbulence scale can be important in a few flow systems [39].

The impact of the turbulence length scale L_x on local Nu_θ number stays highly controversial. Some previous researchers [40, 41] noticed that the integral length scale encounters a critical value of heat transfer and thus the Nusselt number will consistently diminish with expanding integral length scale. Some other [42, 43] recommend a negative relation between the turbulence length scale and heat transfer.

Numerous experiments [44–51] have been led to examine the issue of flat plate boundary layer with respect to the free stream turbulence. They showed that the initial disturbances in the boundary layers are quickly affected by increasing the turbulence intensity of free-stream, while laminar to turbulent transition takes place by randomly forming in turbulent spots. As a result, the breakdown is occurred rapidly by vortices traveling cross-flow. They also presented the linking between the transient growth and streaky structure. This number of experiments covered many new concepts for the early improvement of instability to secondary

instability and breakdown. The main results of these studies are as follows:

- An increase in turbulence intensity accompanied by the promotion of transient growth which is correlated with the streaky structures. Transient growth has a significant role in the boundary layer response. The surface roughness can enhance these impacts as well.

- The Response of boundary layer is non linearly when free-stream turbulence increasing. In the transition region, the thickness of the boundary layer decreases slightly under the laminar flow field and then increases faster in the turbulent flow.

- Due to the incidence of the turbulent spots, the momentum losses are always smaller than in the turbulent flow due to the decrease of skin drag friction.

When boundary layer separation happens close to the front part of a cylinder, there is a high probability that these layers will reattach again on a downstream segment of the cylinder. This relies on upon the cylinder dimensions (blockage and aspect ratios), and level of free stream turbulence [39].

With an increase in turbulence intensity, the critical Reynolds number is decreased extensively, Figure 2.6. This affects the separation position and the profile of the heat transfer curve in the wake region [2, 52–54]. According to **Scholten and Murray** [54, 55], at an angular distance from $\theta \approx 85^o$ *to* $\theta \approx 150^o$, a slight hump in the Nu number distribution on the cylinder wake region due to secondary vortices in this region, Figure 2.8 . After this point, $\theta \approx 150^o$, the second increase in the Nu number appears because of the high shear force created by the unsteady flow and the irregular vortex shedding in the wake.

Much of the focus of the previous studies on the heat transfer rate was on the stagnation region [2, 52, 53, 56, 57]. **Vanfossen et al,** [56] showed that when the turbulence intensity is increased, Nusselt number increases at the front stagnation point and in the boundary layer over the front of the cylinder, and **Sanitjai** [57] reported that as turbulence level increases, the Nusselt number increases at the front stagnation point, however, decreases at the back stagnation point as a result of a smaller wake-width brought on by the deferral of separation. In addition, free stream turbulence increases the heat transfer coefficient and accelerates the laminar to turbulent transition. While **Sak et al,** [43] and **Peyrin et al,** [58] indicated that increases in free turbulence intensity lead to increase heat transfer rate at Reynolds number larger than 10^4 and Laminar - turbulent transition does not occur at low Reynolds numbers range, however, the turbulence intensity still effects clearly, and its effect tends to be larger for higher Reynolds numbers.

In particular, the effect turbulence generated by grid on flow behaviour and lift force at cylinder sections has been treated by [59, 60]. By using (PIV), **Westin et al**, [60] provided database with respect to the cylinder wake region, It has been found that the shear stresses have normal values nearer to the vortices

centre , while the maximum stress are present around the vortices, and owing to the blockage ratio, the drag coefficient is found greater than in unconfined flow conditions. **Blackburn and Melbourne** [59] reported that at low free-stream turbulence (turbulence intensity Tu= 4.6%), periodic vortex shedding transpires in the sub-critical and critical flow fields, while at high turbulence intensity, vortex shedding occurs beyond the critical flow field regimes.

A previous studies in the turbulence intensity have shown its effect on the heat transfer at most positions around a circular cylinder. Present work is an experimental study of the combined effect of surface roughness and the mainstream turbulence intensity on the local and overall heat transfer from a circular cylinder and their effect on thermal boundary layer. In particular, the possibility of an interaction between these two effects is investigated.

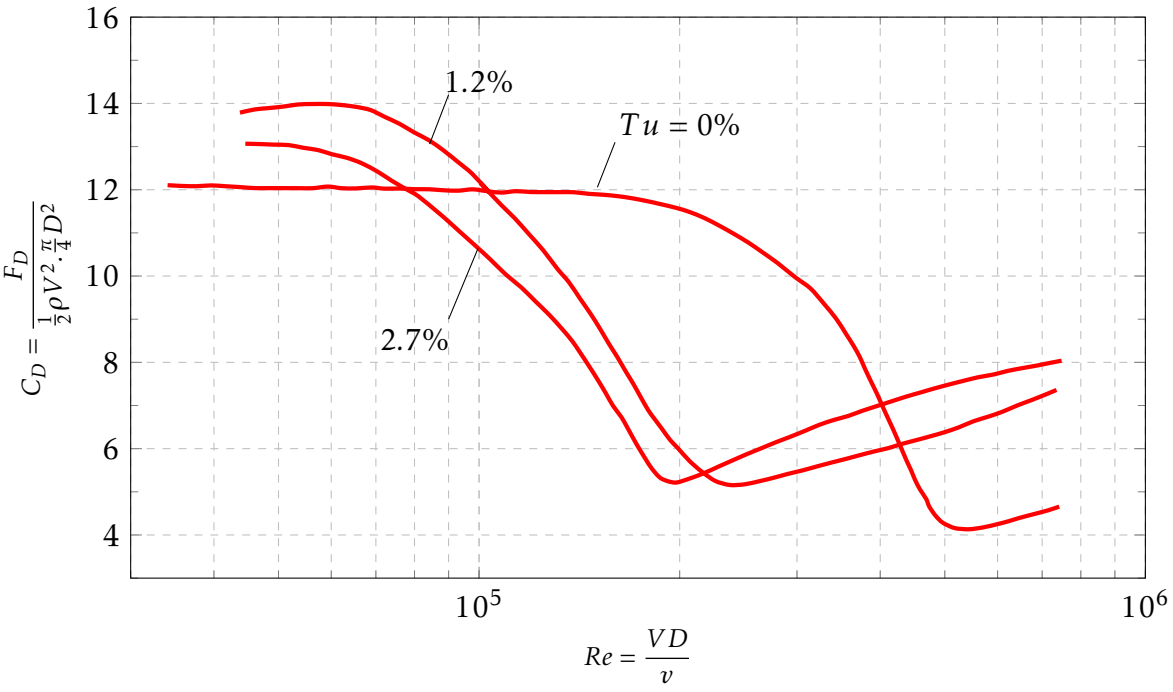

Figure 2.6: The hydraulic drag coefficient as a function of the Tu. [2].

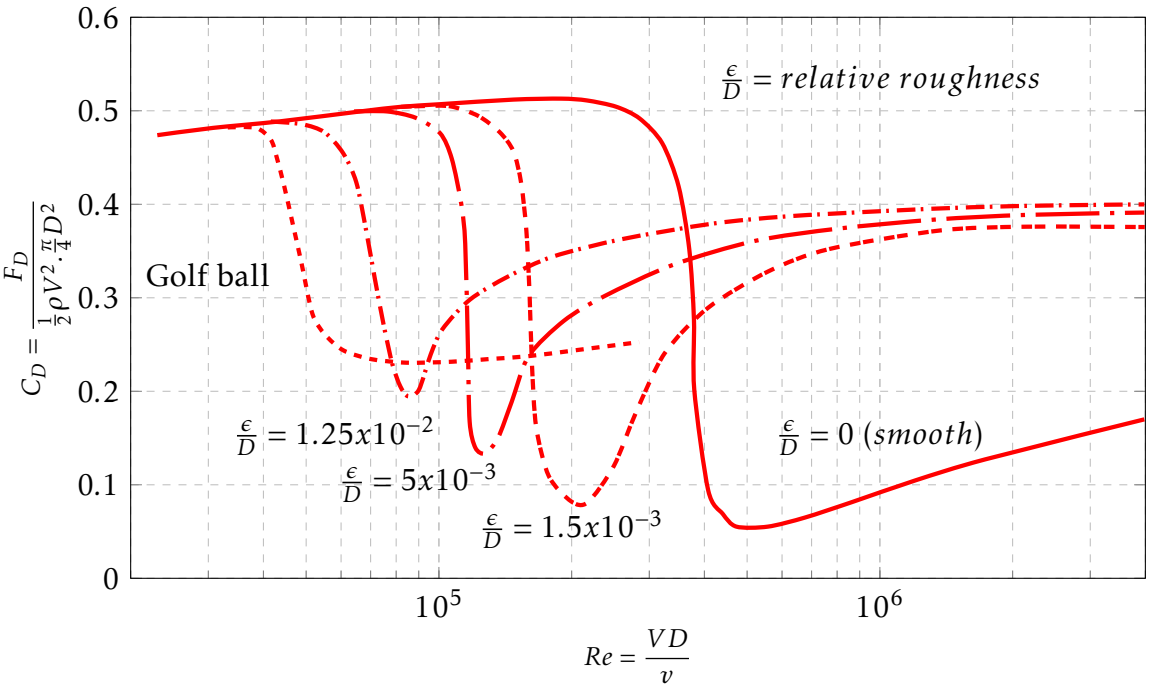

Figure 2.7: The effect of surface roughness on the drag coefficient of a sphere [61]

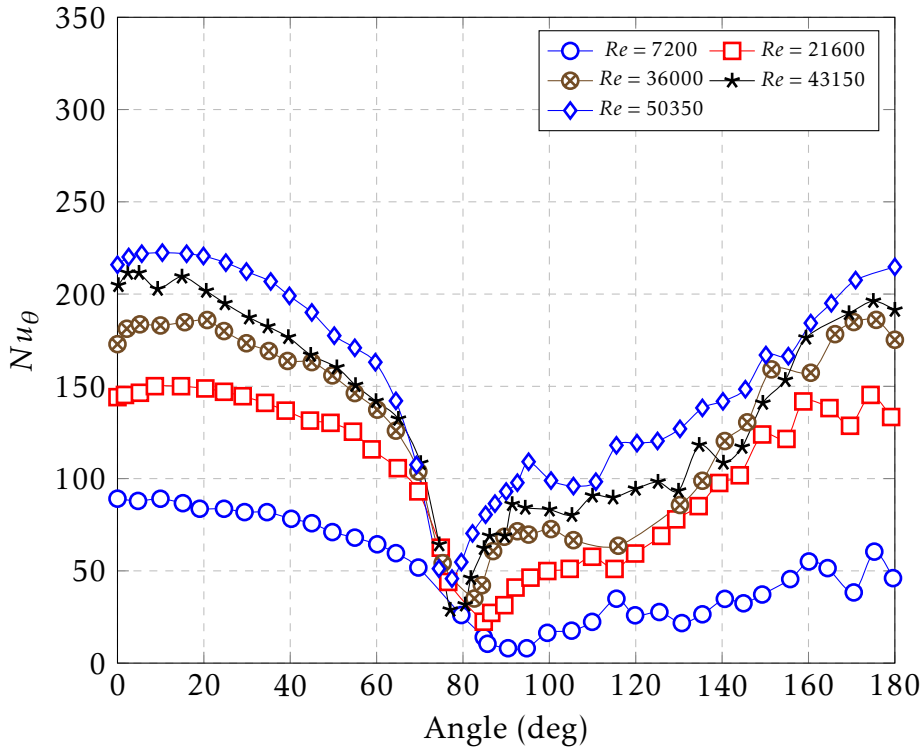

(a)

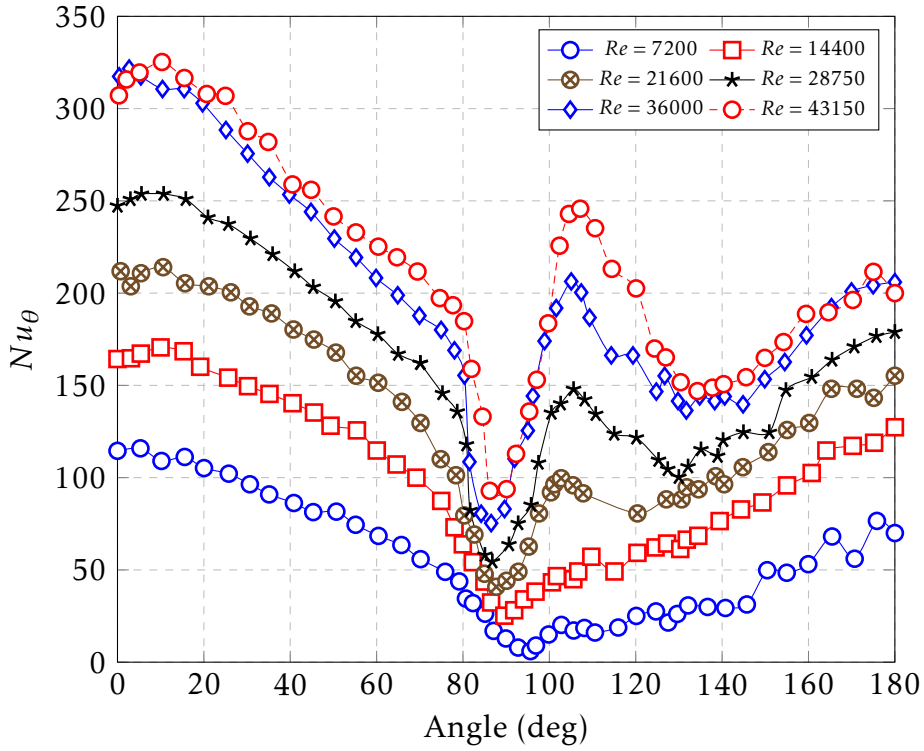

(b)

Figure 2.8: Comparison of local Nusselt numbers from measurements with values obtained from Scholten at $\beta = 0.2$: (a) Low turbulence level Tu= 0.5 [54], (b) High turbulence level Tu = 8.5 [55].

2.2.1.2 Effect of Surface Roughness

The surface roughness can be described by at least two Influential parameters: the first is the relative size of the roughness, ϵ and the other is the texture of the roughness. The majority of the previous studies were performed on the roughened surfaces described by the ϵ/D parameter (relative roughness). Generally, the roughness of surfaces increases the coefficient of drag in turbulent flow regime. However, for blunt bodies (like a sphere, and circular cylinder), increasing the roughness of the surface might reduce the coefficient of drag. [36], Figure 2.7. As shown in this figure, the lower limit of the drag coefficient and critical Reynolds numbers dependent upon the roughness conditions..

Different elements of surface roughness have been examined to illuminate the impact of surface roughness on both flow characteristics and heat transfer rate. The most popular roughness shapes that usually used with wind tunnel studies involve the following: sand-paper [14–16, 27, 62], sand-grain [63, 64], arrays of rods [65, 66], and regular arrangements of pyramids [17, 38, 67, 68].

The impact of surface roughness on the thermal boundary layer and heat transfer coefficient around the circular cylinder has been investigated in several experimental works [17, 27, 38, 65, 67, 68], and numerical studies [69–71]. The works related to the effect of surface roughness on hydrodynamic fields such as lift and drag coefficient, velocity characteristics and pressure drop, it can be found in studies [14–16, 72].

Achenbach [17, 27, 38] carried out a series of experimental studies to investigate the impact of surface roughness on heat transfer and flow field around a circular cylinder at different flow regimes. A two-roughness technique was reproduced by sand paper warping around the cylinder (it is described in [27] and by using regular arrangements of pyramids [17, 38]. In these studies the variation of the relative roughness (ϵ/D) was 1.1×10^{-3} to 9×10^{-3}.

Achenbach´s results [27] showed that the drag coefficient is not influenced by both ϵ/D and Re number if the values of both of them are large enough. However, it continues to depend upon relative roughness even at high Re, when the ϵ/D is not high enough and the value of drag coefficient is lower for small relative roughness. Achenbach´s experiments [17, 38] showed that the subcritical flow range was not affected clearly by the surface roughness, Figure 2.10. However, the roughness factor played a significant role in the local and total heat transfer coefficient in critical and super-critical flow conditions (an increase in the relative roughness was accompanied by augmenting in heat transfer), Figure 2.9, and in trans-critical flow, surface roughness increase heat transfer by a factor approximately 2.5.

Because of the surface roughness, the boundary layer pattern around the cylinder surface undergoes to sharp changes [73]. **Achenbach**, [38] and **Zukauskas**, [2, 73] reported that the beginning of the critical flow regime strongly depends on the roughness of the surface and occurs at lower Re number with bigger roughness elements, Figure 2.10. At low Re numbers, the laminar boundary layer surrounds rough surface parameters totally and the surface roughness does not affect on total

heat transfer, while at bigger Re numbers, where the boundary layer is thinner than the height of roughness parameters and total heat transfer is completely dependent on surface roughness.

The temperature profiles and the local heat transfer coefficient in the boundary layer were measured to examine the impact of the roughness on the natural convection along a vertical cylinder [68]. Experimental results show that due to the surface roughness which increases of the real surface area, the local heat transfer rate for water decreases slightly about 5% in the laminar region and increases slightly about 5% in the turbulent region.

The studies [65, 67] focused on the impact of the relative roughness on the convective heat transfer coefficient. Kolar's results [67] show that the surface roughness reduces the mean velocity and increases the friction factor as well as the heat transfer coefficient that increases just as much as to compensate the loss of the kinetic energy when compare under the same pressure drop in a smooth surface. While **Gomelauri** [65] reported that the increase of heat transfer coefficient reached a maximum value when the spacing to height ratio of roughness element (repeated-rib) was equal to 13 and this result did not depend on the cross section of the roughness element.

The effect of the roughness of the surface on the flow separation and development of the boundary layer has been implemented in a number of research papers [14, 15]. **Batham** [14] conducted measurements at the critical Reynolds number for both a smooth cylinder and a cylinder with sandpaper roughness. It was found that the free-stream turbulence leads to an increase in the level of vortex energy for the rough cylinder. On the other hand, turbulence in the behind of the cylinder has high intensity (in excess of 10%) at Reynolds numbers of 1.11×10^5 from a rough cylinder while at a smooth cylinder Reynolds numbers reach $2.35 \times l0^5$. In a uniform flow field, the impact of the roughness on the boundary-layer development and mean-pressure distributions are explained by **Guven** [15], who used five sandpaper sizes over the Reynolds-number range $7 \times l0^4$ to $5.5 \times l0^5$. This study shows that even at high Reynolds numbers, the roughness of the surface has a substantial effect on the mean-pressure distribution. Also, the relationship between surface roughness, pressure-distribution, and drag coefficient factors may be described based on boundary layer behavior. Particularly, it also is shown that the higher roughness makes the boundary layer thicker, and then a larger distortion in momentum around the cylinder.

An analysis of preceding papers shows that the fundamental question in these studies dealing with the influence of rough surface on comparatively turbulent flow regime. In low Re flows, the impact of roughness on the heat transfer coefficient was weak. Although the wide investigations on the laminar flow performance in heat transfer around the circular cylinder, such as **Lange** [74–76], there has been a limited debate regarding the effect of the roughness of cylinder surface on heat transfer coefficient for laminar flow fields. With the extensive progress in mini- and micro-fluidic systems, and thus the fluid flow is laminar

because of the miniature size of the design, investigators have shown a growing attention in the heat transfer from rough surfaces in laminar flow fields [77–80]. Generally, in these studies, the rough surface is modelled directly by using different shapes blocks periodically spread on the surfaces except in [81], who used different way (radial fins) to modelling the effect of roughness to enhance of heat transfer around the cylinder.It was found that short fins minimize the heat transfer rate of a cylinder. While with long fins, this influence is reversed, where the magnification of the surface can compensate for this influence. Also, the results suggest that for a specific value of Re number and fin height there was an optimum number of fins to get the maximum Nu number.

Comparable with the direct modelling of roughness, different investigations have been suggested to calculate the influence of surface roughness. Particularly, **Koo** [82] proposed an equivalent concept of a layer of porous material for modelling the rough near-surface region. By using the same technique, **Bhattacharyya** [83] investigated the effect of a thin porous wrapping around the circler cylinder on the increase of surface heat transfer rate. He revealed that the heat transfer rate from the cylinder could meaningfully decrease using a slim porous layer has same thermal conductivity as the cylinder.

All the studies analysed so far in this section, regarding the influence of cylinder roughness on heat transfer, nevertheless, all suffer from a matter that they did not investigate the effect of free stream turbulence on heat transfer from a rough cylinder in a cross-flow.

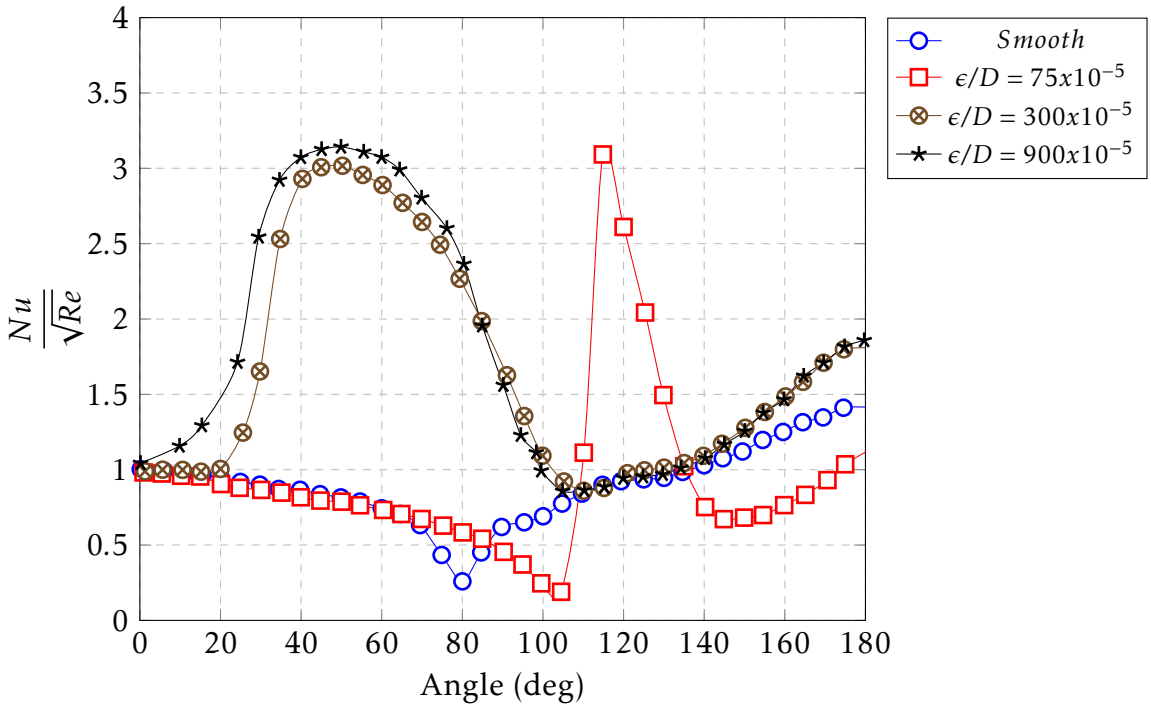

Figure 2.9: Variation of local heat-transfer coefficient at $Re = 2.2x10^5$ and different roughness parameter, [27].

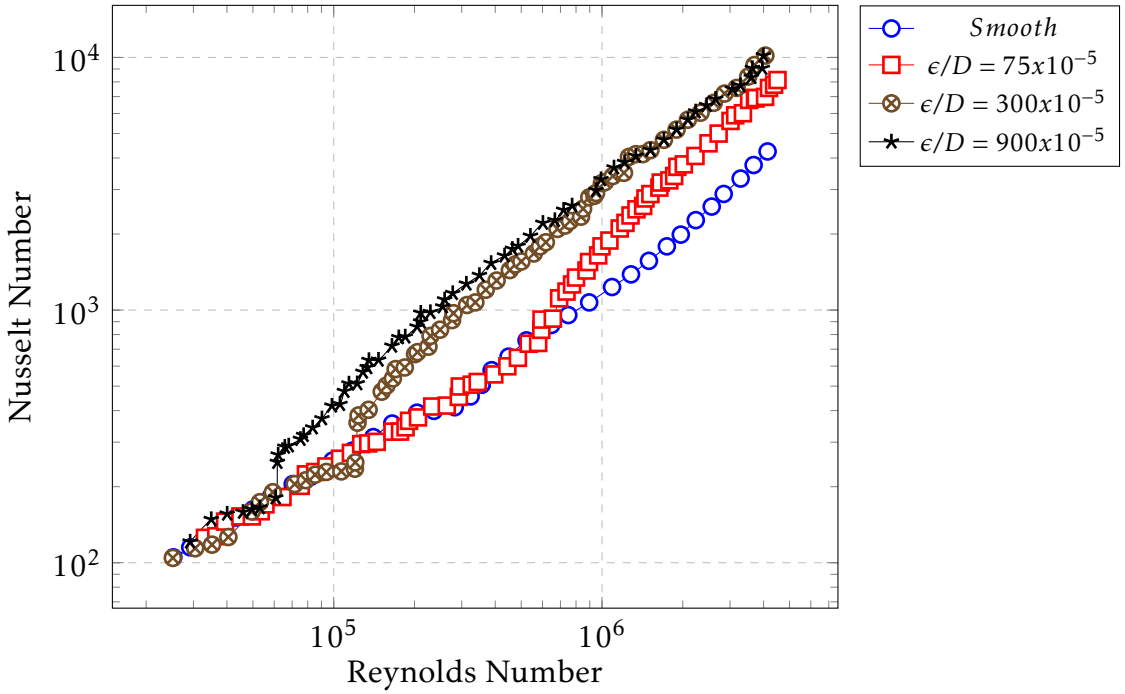

Figure 2.10: The total heat transfer coefficient as a function of Reynolds number and different roughness parameter (ϵ/D), [27].

2.2.2 The empirical correlations of heat transfer

Presently there are a number of offered empirical correlations to evaluate local and average heat transfer around a smooth heated cylinder (Table 2.1). These relations have been arranged by using two different fluid properties bases. One set uses the cylinder surface temperature to estimate the fluid and flow properties and the other set use film temperature. Most of the earlier researchers have studied the heat transfer of forced convection over a circular cylinder varying from high diameters to thin wire with a wide range of Reynolds numbers and various fluids, following is a brief outline of the most common empirical correlations, which are used for a circular cylinder in cross-flow. Some of the correlations and experimental data were replotted in Figure 2.11.

Table 2.1: The empirical correlations of the local and average Nusselt number around smooth cylinder

Author	Correlation		Range of Reynold	Range of Prandtl
Churchill and Bernstein [84]	$Nu = 0.3 + \frac{0.62Re^{1/2}Pr^{1/3}}{[1+(0.4/Pr)^{2/3}]^{1/4}} \times \left[1 + (\frac{Re}{282{,}000})\right]^{4/5}$	(1)	$100 - 10^7$	$Re.Pr > 0.2$
Morgan [85]	$Nu = 0.148Re^{0.633}Pr^{\frac{1}{3}}$	(2)	$5\times10^3 - 5\times10^4$	–
Zukauskas [7]	$Nu = 0.26Re^{0.6}Pr^{0.37}\left[\frac{Pr}{Pr_w}\right]^{0.25}$	(3)	$10^3 - 2\times10^5$	–
Sparrow [86]	$Nu = 0.25 + (0.4Re^{1/2} + 0.06Re^{2/3})Pr^{0.37}\left[\frac{\mu}{\mu_w}\right]^{1/4}$	(4)	$1 - 10^5$	–
Khan [87]	$Nu = 0.593Re^{1/2}Pr^{1/3}$	(5)	$1 - 10^5$	$\geqslant 0.71$
Whitaker [88]	$Nu = (0.4Re^{1/2} + 0.06Re^{2/3})Pr^{0.4}\left[\frac{\mu}{\mu_w}\right]^{1/4}$	(6)	$1 - 10^5$	$0.67 - 300$
Perkons and Leppert [89]	$Nu\left[\frac{\mu}{\mu_w}\right]^{0.25} = (0.31Re^{0.5} + 0.11Re^{0.67})Pr^{0.4}$	(7)	$40 - 10^5$	$1 - 300$
Achenbach [38]	$Nu = 0.18Re^{0.63}$	(8)	$> 10^4$	0.72
Sanitjai and Goldstein [11]	$Nu = 0.446Re^{0.5}Pr^{0.35} + 0.528((6.5e^{Re/5000})^{-5} + (0.031Re^{0}.8)^{-5})^{-1/5}Pr^{0}.42$	(9)	$2\times10^3 - 10^5$	$0.7 - 176$
	$Nu_0 = 1.11Re^{0.5}Pr^{0.35}$	(10)	$2\times10^3 - 10^5$	$0.7 - 176$
Sarma, and Sukhatme [90]	$Nu_0 = 0.91Re^{0.5}$	(11)	> 1200	–

The Frossling factor ($Nu/\sqrt{Re}$) is provided from **Frossling** [91] as a function of the angular position from the front surface of a cylinder. In the laminar boundary layer region $\theta \leqslant 60^o$, theory and experiment come to an agreement where the Nusselt number is proportional to $\sqrt{Re}$. Generally, In the incompressible fluid flow (Pr=0.7), the Frossling number may be used to normalized Nusselt number.

Churchill and Bernstein [84], based on large number of experimental data, they proposed semi-empirical correlation, Eq.(1) in table 2.1, where all properties are estimated at the film temperature. This relation is quite comprehensive equation that covered entire range of Re and Pr number. **Morgan** [85] showed an extensive evaluation of literature on convection from smooth circular cylinders and recommended her own correlation equation.(2). Most early studies were interested with overall Nusselt number from circular cylinders that was reviewed

in [7, 85], correlation Eqs(2)-(3), respectively. From previous studies for circular and non-circular cylinders, **Sparrow et al.** [86] collected the data on average Nusselt number and proposed the correlation Eq.(4). All fluid properties in this equation are calculated at the free-stream temperature and μ_w is calculated at the temperature of the cylinder surface.

Whitaker [88] recommends the comprehensive correlation Eq.(6). Which all properties (except μ_w) are evaluated at average fluid temperature. Eq.(6) is valid for $\mu/\mu_w = 0.25 - 5.2$. **Achenbach** [38] investigated experimentally the impact of surface roughness on the Nusselt number around a cylinder and he proposed a correlation, Eq. (8) for smooth surface cylinder. **Sanitjai and Goldstein** [11] studied the local and average heat transfer from a cylinder. They proposed an empirical correlation to predict the average Nusselt number Eq.(9) and heat transfer of stagnation point Eq.(10) , Also, **Sarma, and Sukhatme** [90] presented equation (11) for heat transfer of stagnation point.

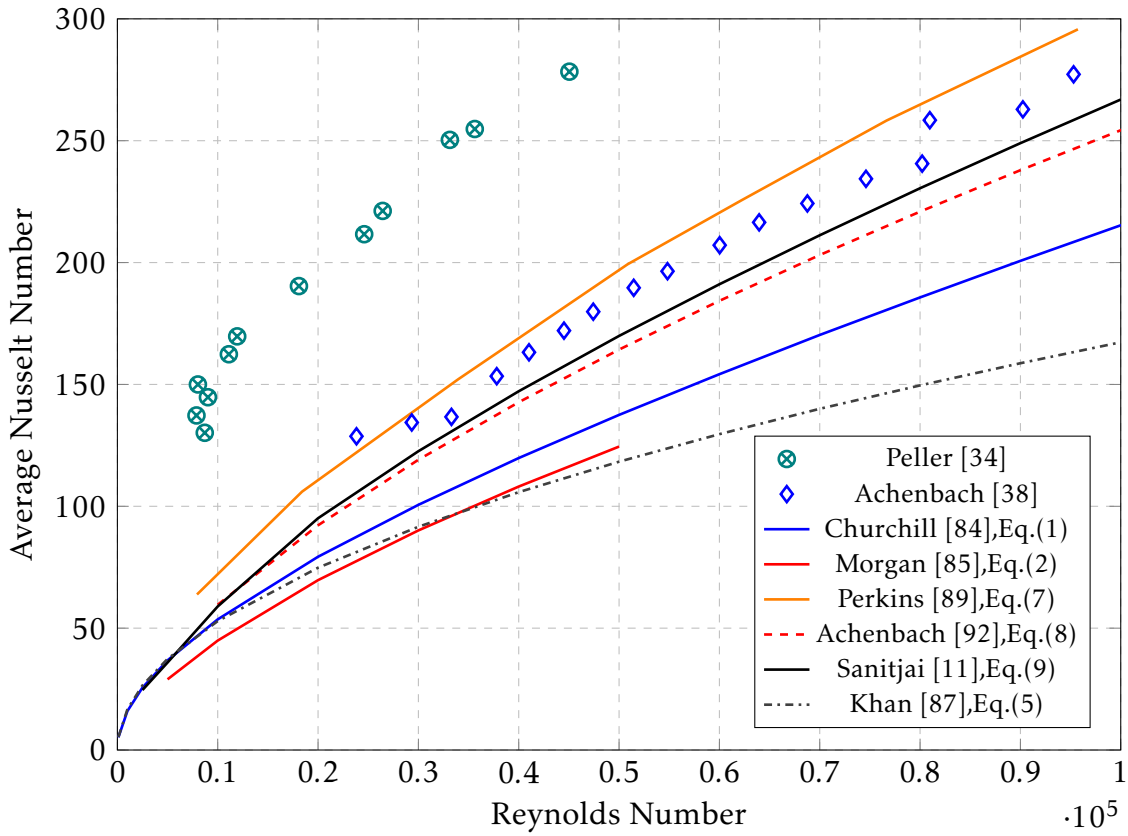

Figure 2.11: Total Nusselt number as a function of Reynolds number for smooth circular cylinder in cross flow.

CHAPTER 3

Experimental Arrangement and Instrumentation

Experiments were carried out in an open-circuit wind tunnel. The apparatus consisted of a Perspex working section through which air was being drawn by two centrifugal fans. The test cylinder (0.05 m outer diameter and 0.125 m long) were inserted horizontally into the working section at right angles to the direction of airflow and positioned half-way between the floor and the roof of the test section. The air entered the apparatus by way of a bell-mouth to ensure smooth entry of the air to the testing chamber. To prevent fan induced bulk flows from the fan back into the test section, honeycomb flow straightener was placed after the test section. A traversing mechanism available on top of the test section for moving and controlling the instruments.The apparatus is shown in Figure 3.1 and Table 3.1 provides specifications of the centrifugal fans.

Table 3.1: Fans specification

Fan Type	Max Air Flow **m^3/hr**	Fan Speed **rpm**	Intake Dim. **cm (inch)**	Power **watt**	Max. Current **A**	Voltage **V**
Gryphon	1200	2850	20.32(8)	750	5.8	220-240
Alpak	1200	2800	20.32(8)	750	4.5	220-240

3.1 Wind Tunnel

The open-circuit wind tunnel was made from carbon steel, it was approximately 2.5 m (long), consisted of a 125 mm square cross section becoming 200 mm circular cross section , a test section was a rectangular duct (200 mm long) and 125 mm cross-section: Details of the test section was shown in Table 3.2 . The walls were (20 mm thick-clear acrylic plexiglass). The test cylinder was fastened horizontally, 1250 mm from the wind tunnel entrance. A graduated throttle valve in the fan duct discharge was used to adjust the flow velocity. The velocity range (without the cylinder in the test section) ranging from 3 m/s to 31 m/s corresponding to a cylinder-diameter Reynolds number of $10,000 - 102,000$.

A pitot tube and HWA probe were positioned of the test section. It could be traversed in the wind tunnel providing information on the velocity profile. In addition, to full check of flow in the cross section, five traversing holes were provided, and for exploring the wake flow pattern, at traversing position is provided downstream of the cylinder [93].

Mid plane mean velocity profiles of the test section are shown in Figures 3.2, 3.3 and 3.4 and the pressure drop is shown in Figure 3.5. The maximum cross-sectional variations in the approach velocity, were ±4% (mostly ±0.5%) of the mean over the traversed area. The velocity profile was considered to be sufficiently uniform. the presence of the test cylinder resulted in a more uniform velocity distribution although the velocity was slightly reduced.

Table 3.2: Details of the test section and test cylinder

1- Test section	
Material	Plexiglas
Working cross-section	12.5×12.5 mm^2
Thickness	20 mm
Fluid	Air - approximately 23^oC
2- Test cylinder	
Material	Aluminum $6082T_6$
Diameter	50 mm
Length	100 mm
Aspect ratio	2
Blockage ratio	0.4

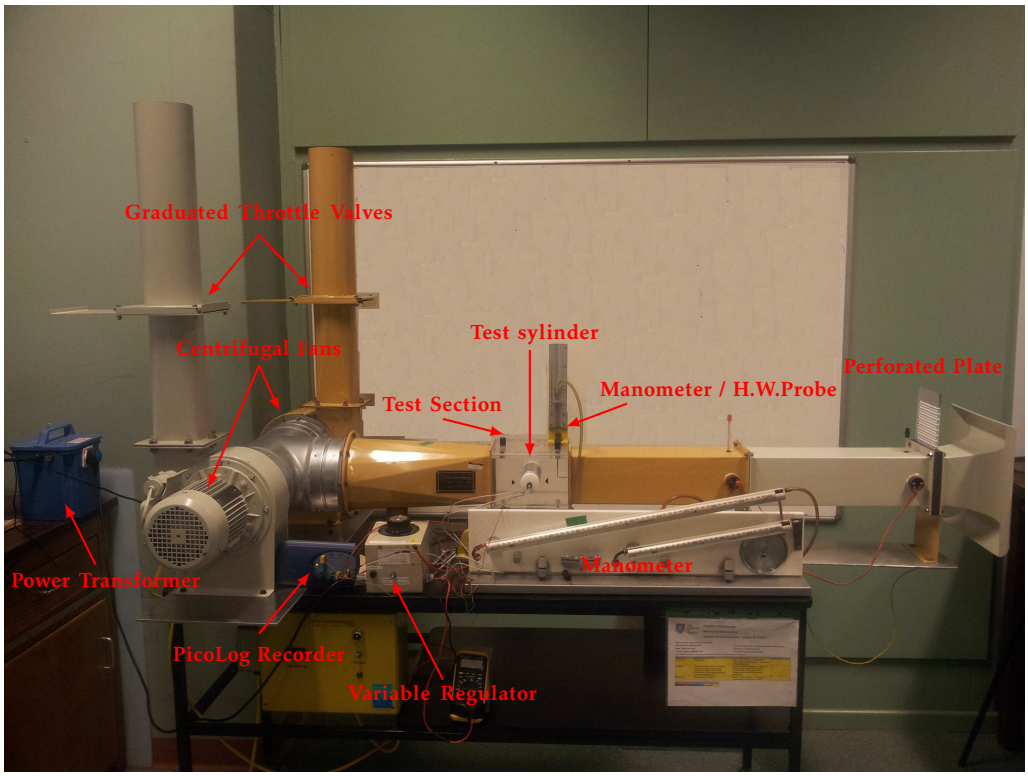

Figure 3.1: The experimental test rig and instrumentation for air flow and heat transfer studies of a cylinder.

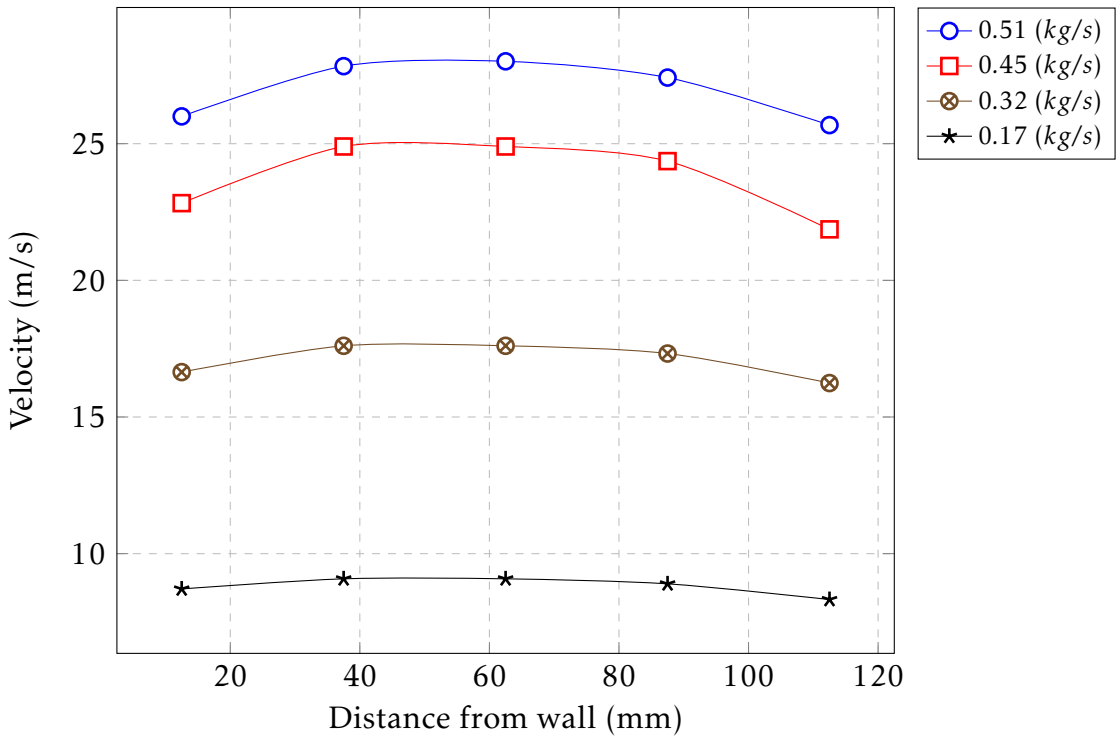

(a)

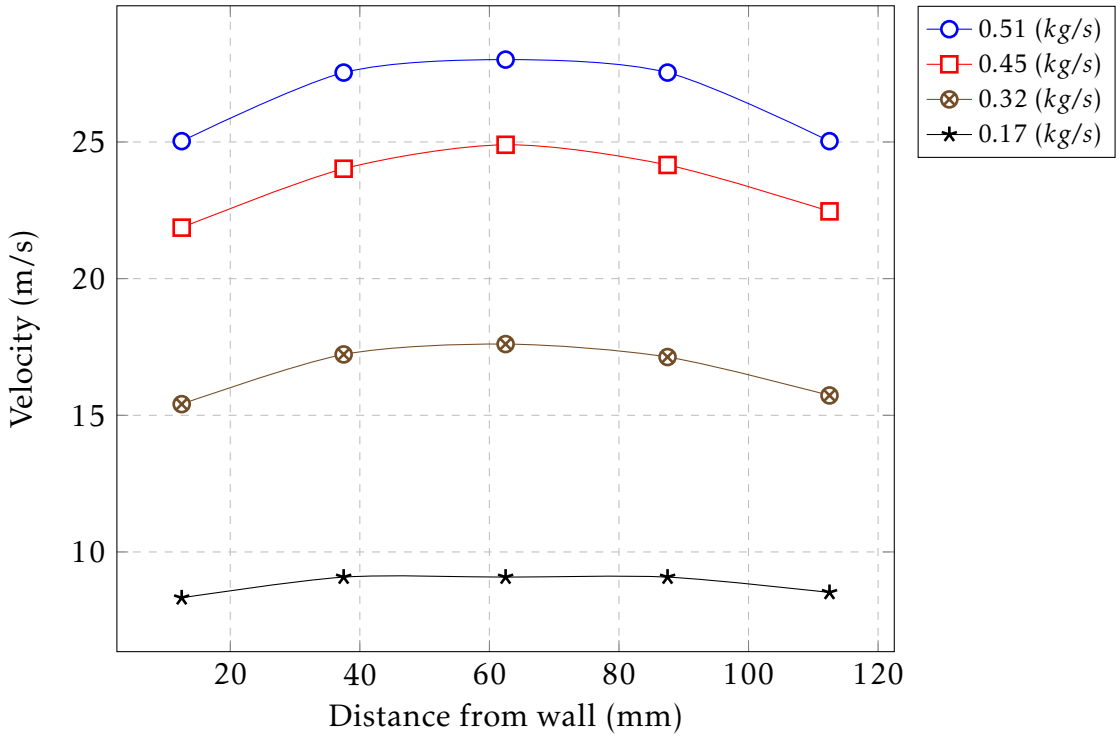

(b)

Figure 3.2: Velocity profile with different mass flow rate at mid working section without cylinder measured on (a) horizontal line (b) vertical line.

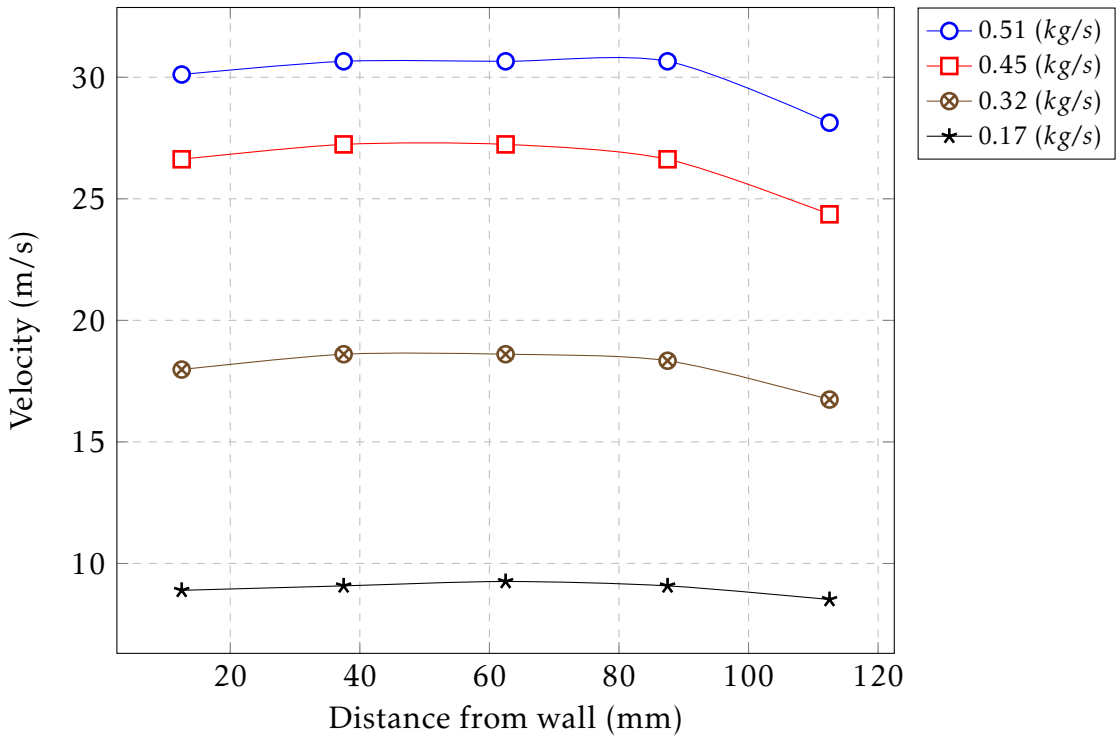

(a)

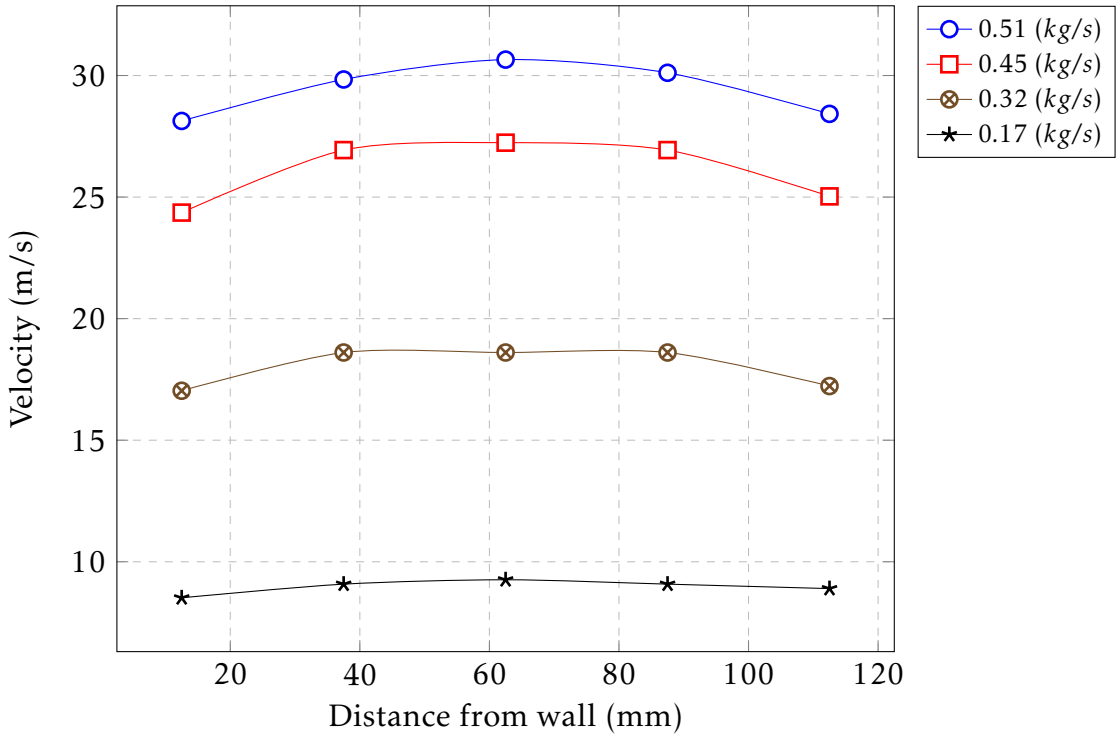

(b)

Figure 3.3: Velocity profile with different mass flow rate at mid working section with cylinder measured on (a) horizontal line (b) vertical line.

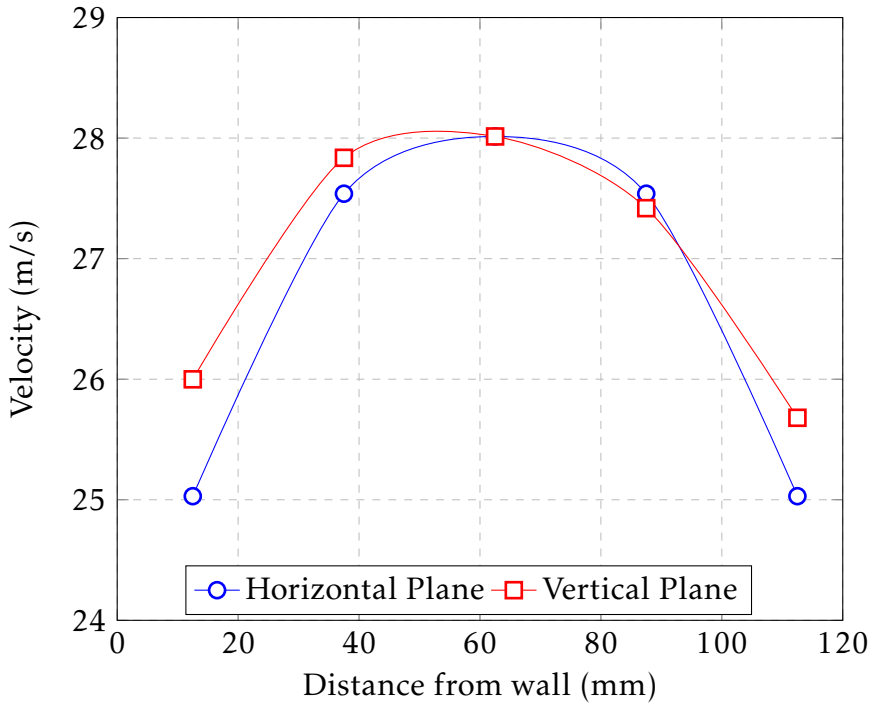

Figure 3.4: Velocity distribution in a section normal to the flow upstream from the test cylinder at mid working section at max. mass flow rate (0.51 kg/s)

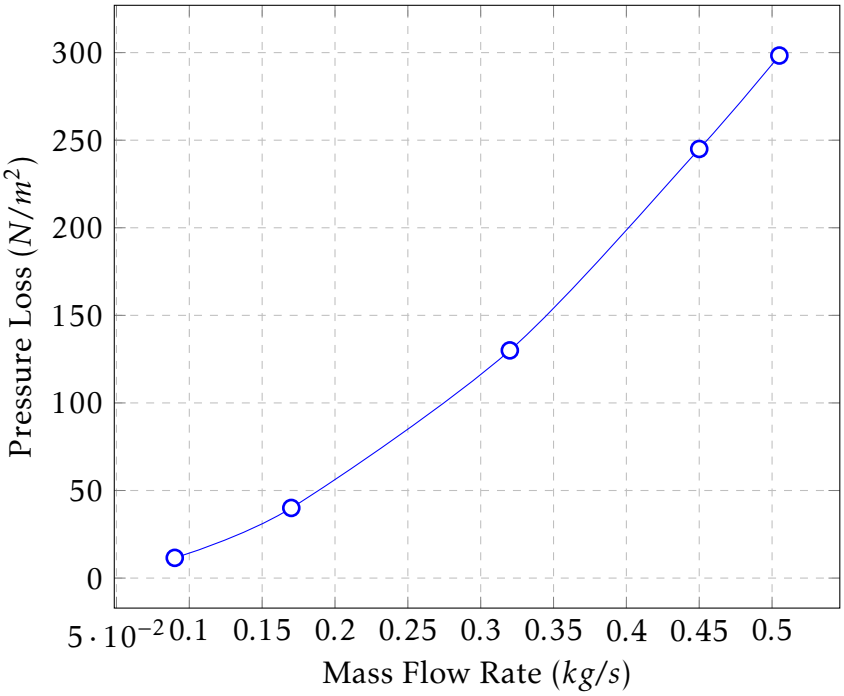

Figure 3.5: Pressure drop across the cylinder plotted against mass flow rate.

3.2 Heated Cylinder

Tested were performed using a heated cylinder (50 mm outer diameter and 10 mm inner diameter) of aluminium type (6082T6), 100 mm long mounted between two extension rods of Teflon (PTFE): The diagram of the test cylinder was shown in Figure 3.6. The effective ratio (aspect ratio = L/D) of the cylinder was 2 and the blockage ratio (β) $D/B = 0.4$. The PTFE mounts also served as insulators, reducing axial conduction losses. A circular graduated flange was fitted in the heated cylinder to allow the cylinder to be rotated about its central axis whilst in the wind tunnel in 10^o increments. A protractor was mounted on the test section wall to set the angle, as illustrated in Figure 3.7.

The aluminium was polished to achieve a smooth surface for the smooth cylinder. Details of the test section and test cylinder was shown in Table 3.2. A cartridge heater installed in the centre of the aluminium cylinder acted as a heat source. The heater was supplied from AC power transformer. The RS 37259 a voltmeter with ±0.1% sensitivity was used to acquire the highly accurate heater voltages. The variable regulator was used to maintain constant surface temperature over the length of the cylinder.

To achieve constant surface temperature, the test cylinders were manufactured from aluminium, which has a high thermal conductivity ($k = 180 W/mK$) and the cylinder wall has thick (20 mm) which working as heat store to recompense for the temperature differences because of changing the circumferential heat flux.

The fundamental assumptions in the analysis was:

1. The heat transfer was two-dimensional and steady flow (infinite cylinder).
2. The radial heat flux at the internal diameter of the cylinder was constant.
3. Inner temperature of the cylinder was equal to the surface temperature of the cartridge.
4. The electrical power was fully converted into heat which was dissipated by convection and radiation.
5. The differences in surface temperature were only due to the local variations of the heat transfer coefficient.

3.2.1 Cartridge Heater

A 400 W cartridge heater manufactured by Invotec was used, Figure 3.8. The cartridge also contained a thermocouple (type-J), which gave the heater temperature. It was embedded in the core of the heater at the mid-span [94]. For ensuring access to the steady state and as an alternative to a surface thermocouple which its

reading fluctuation due to the effect of free-stream turbulence, this thermocouple was used.

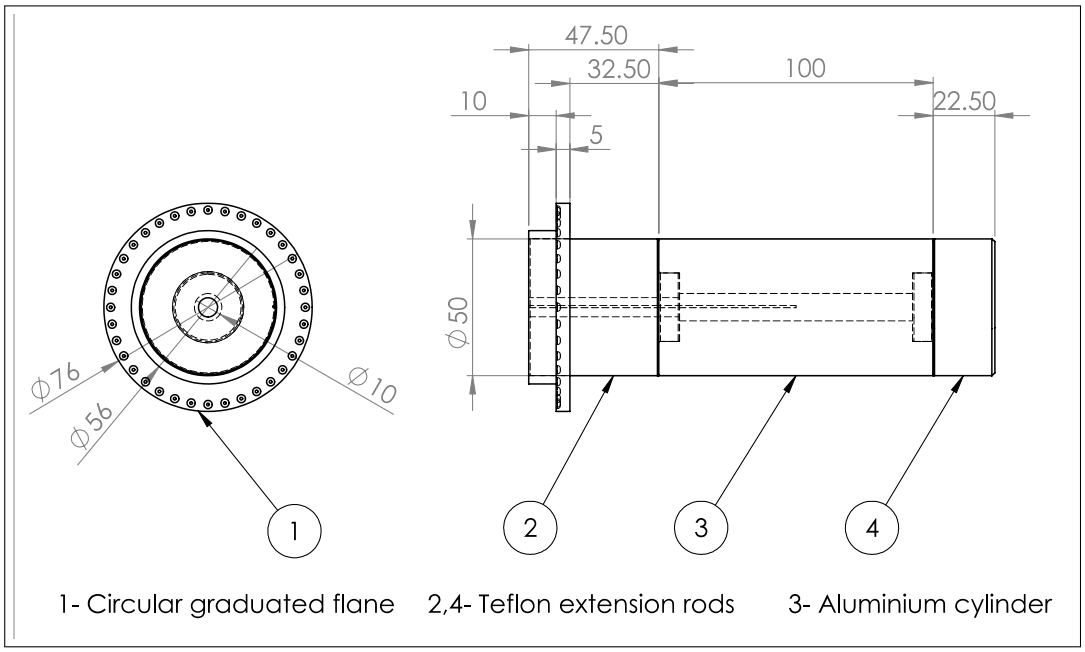

Figure 3.6: A schematic diagram of the test cylinder

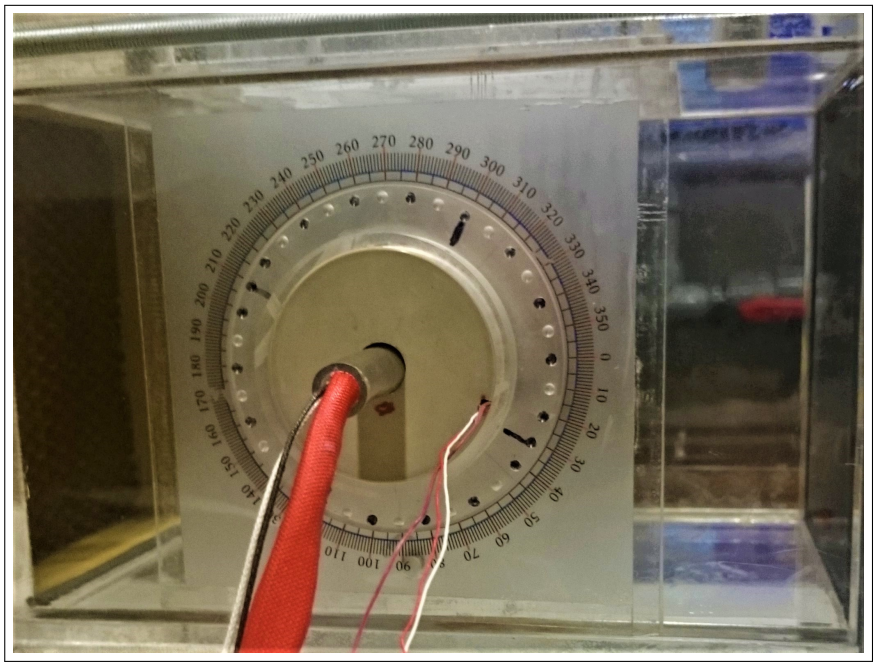

Figure 3.7: A circular graduated flange and a protractor mounted on test section

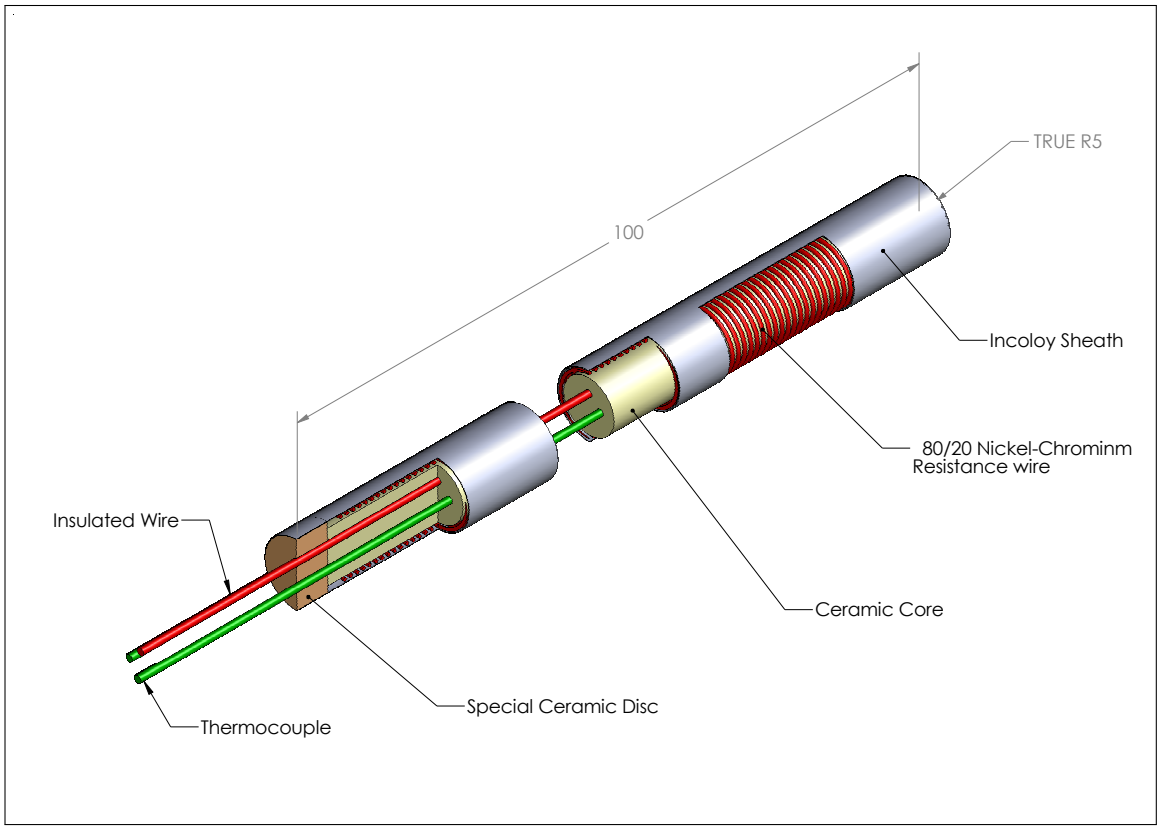

Figure 3.8: A Diagram of High-Density Cartridge Heaters [94].

3.2.2 Thermocouple Arrangement

Mercury-in-glass thermometer and thermocouple at the air, the inlet and outlet temperature of the air is determined. Local surface temperatures are obtained from heat flux sensor (see section 3.3).

The output from the thermocouples junction and heat flux sensor were logged on a computer through data acquisition system 8 channels of a PicoLog data logger (USB TC-08). The thermocouples reading were calibrated against a reference thermometer, cartridge thermocouple gives an uncertainty of $\pm 0.35\ ^{o}C$ and surface thermocouple give an uncertainty of $\pm 0.2\ ^{o}C$ in each temperature reading.

3.3 Heat flux Sensor

The heat flux sensor used was thin film sensor (manufactured by Rdf Corporation) it measured both the surface temperature and heat flux. The sensor was flexible and could be attached to flat or curved surfaces. The key features of the sensor are shown in Figure 3.9. The heat flux is determined by measuring the temperature difference across a micro-foil of polyamide (Kapton) of known thermal conductivity [95]. In order to increase the sensitivity (magnitude and resolution) of the electrical signal for the smallest possible surface area, five pairs of thermocouple junctions were arranged on opposite sides of the film, as shown in Figure 3.10.

A Type T thermocouple junction is also incorporated on the sensor. To protect this junction, it is inserted between two layers of thin Kapton film. The total thickness of the sensor was around 0.3 mm. The heat flux measurement area was 5 mm by 16 mm. The maximum operating temperature of 260 ^oC, limited by the polyamide components of the sensor. Table (3.3) shows main specifications of heat flux sensor. A more detailed descriptions of this type of sensors is given by Ortolano and Hines [96].

Table 3.3: Specifications of heat flux sensor [95]

Specifications	
Nominal sensitivity	**3.488 μ V/ (W/m^2)**
Maximum recommended heat flux	**113 kW/m^2**
Response time	**0.4 s**
Thermal capacitance	**1021 J / (m^2 -^{o}C)**
Thermal impedance	**0.002 ^{o}C/ (W/m^2)**
Maximum operating temperature	**260 ^{o}C**

The flux sensor was calibrated at the Rdf Corporation for the temperature range of -200 ^oC to 200 ^oC at a base temperature of 21 ^oC, and a multiplication factor is provided as shown in Figure 3.11. The nonlinear nature of this is a result of changes in the thermal properties of the sensor. The procedure to determine the heat flux from the voltage signal of a sensor is described in detail [97] and [98].

The voltage differential created by the sensor (e_s) is proportional to the heat flux crossing through the sensor (q_s) the constant (c) is determined by:

$$q_s = \frac{e_s}{c} \tag{3.1}$$

The manufacturer supplied calibration constant (c) for this heat flux meter is 3.488 $\mu V/(W/m^2)$.

A RdF micro-foil heat flux sensor is mounted on the centre - plane of the heated cylinder by using two-sided adhesive tape. The sensor is then connected to the data acquisition system to monitor the heat flux and surface temperature at the specific point. The Single-Channel Terminal Board plug was connected to a channel on the TC-08 to convert it to a high-resolution data logger (20-bit) and to let measuring heat flux voltage signals.

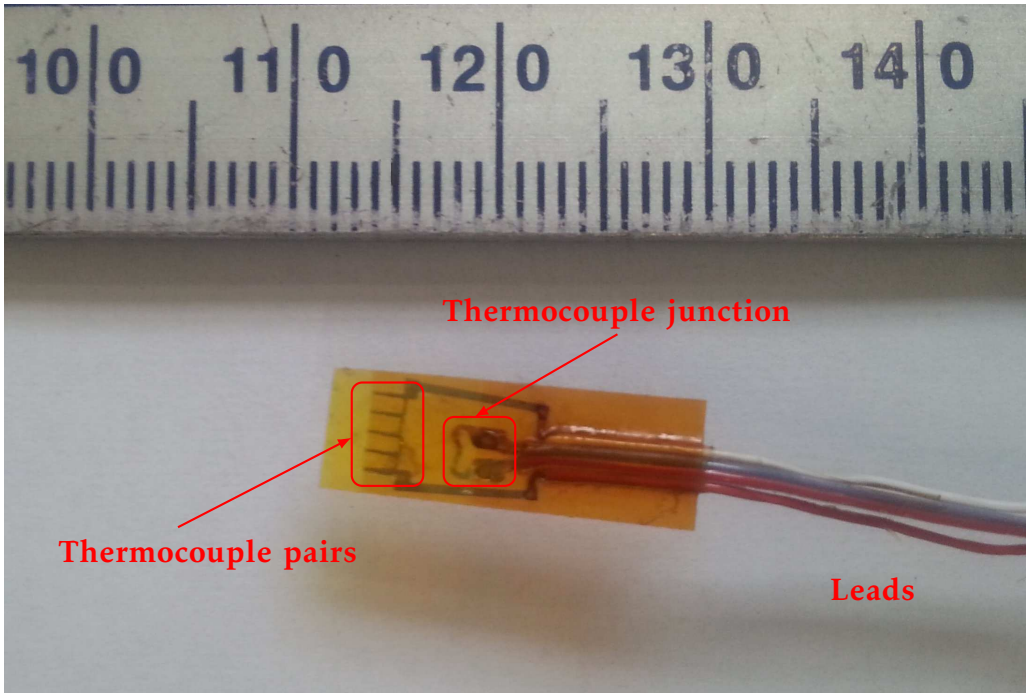

Figure 3.9: The heat flux sensor.

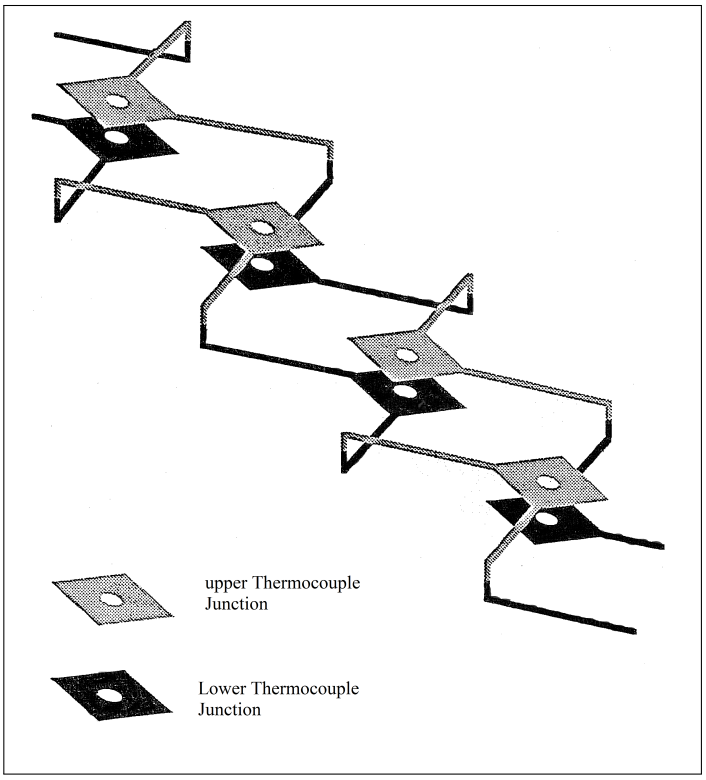

Figure 3.10: Deyails of the heat flux sensor thermocouple pairs and connections [99]

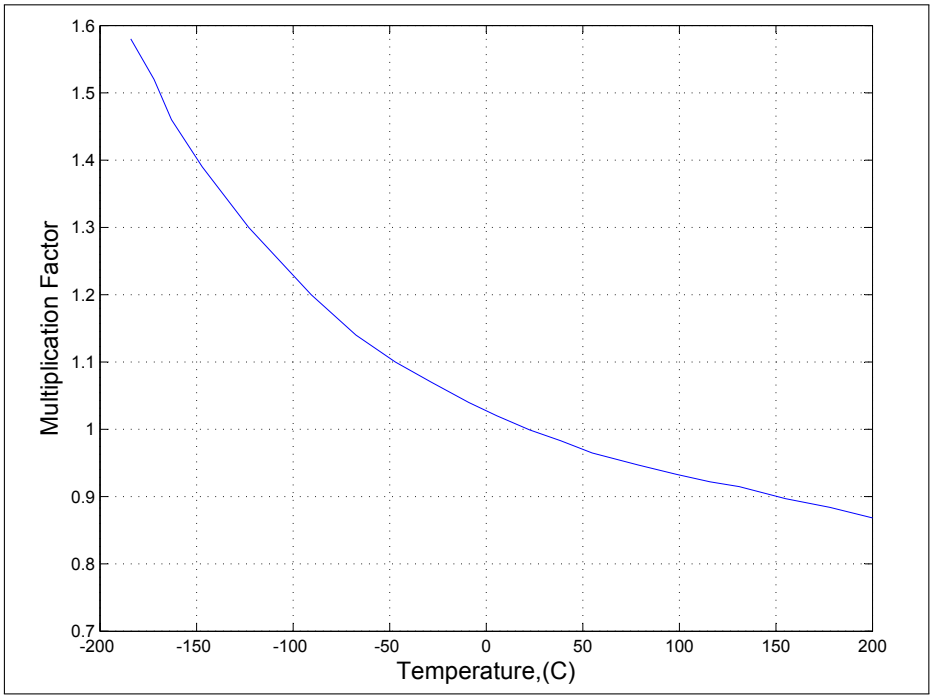

Figure 3.11: RdF Heat Flux Sensor Calibration Curve

3.4 Turbulence level

3.4.1 Hot wire system

The determination of all turbulence quantities was carried out using hot-wire probe (DISA type 55P16) and a constant temperature hot-wire anemometer (MiniCTA 54T30). The data was sent to the PC by means of a National Instrument (NI 9215) board compact with (NI cDAQ-9171) which has a 16-bit ADC resolution and conversion time 4.4 μs. All signal data were acquired using Labview software. A calibrator unit ($TSI, Inc., Model 1125$) was used to calibrate the hot-wire (Section 3.4.3). Turbulence statistical quantities like turbulence intensity and integral length scale were all provided by using data analysis programs (MATLAB and NI DIAdem) (see the example in Appendix B to calculate the turbulence fluctuation velocity, the integral time scale, and dissipation length scale).

3.4.2 Turbulence-Generating Grid

To promote free-stream turbulence to the desired intensity, perforated plates (3 mm thick, 125 mm wide and 125 mm high.) made from Perspex were used. Perforated plate are chosen instead of grid because they enable to create a flow that approximated isotropic and homogeneous flow, even for a high turbulence intensity of free stream [43, 100, 101], and hence the lateral scale of the streamwise velocity component is nearly half the longitudinal one (in agreement with isotropic turbulence theory [39]). The FST homogeneity is essential in order to have the same circumstances all around the test section.

Based to a prior experimental work [43] and for obtaining nearly isotropic turbulence downstream grids, the solidity ratios were selected according to special design requirements. **De Silva**, [102] declared that the solidity ratio of grids generating turbulence should be less than < 60%, to achieve almost isotropic turbulence.

Turbulence nature downstream from perforated plates cannot be specified in theory but is known that it depends on the solidity area ratio and the perforation diameter. The disparity of these two factors with various levels of mass flow rate led to achieving different combinations of turbulence intensities and turbulence length scales at various downstream positions. Table 3.4 shows the different perforations patterns which were tested to chose some of them in the present study. Each plate was varied in hole diameter, hole spacing, and a number of holes to provide different solidity. These perforated plates were located in upstream drawers that are easily changed during runs and positioned normal to the flow, Figure 3.12. Technically, the same technique and the same experimental procedure were applied as those described in [43, 58, 101, 103, 104].

The perforated plates were positioned at the different distances from the

beginning of the test section to get a variety of turbulence features. The variation of the turbulence intensity Tu as a function of the distance from the entrance of the test section for the seven of plates is shown in Figure 3.13, and the pressure drop due to these plates is shown in Figure 3.14. Preliminary experiments have shown that the turbulence intensity increases with the diameter of plate perforations and decreases with the distance from the promoter, while the pressure loss depends on plate solidity. Thus, Plates 1, 5,6,7 were chosen at about 100 mm upstream from the entrance of the working section to get lowest pressure losses and a good variety of turbulence characteristics. The schematic diagram of these plates are shown in Figure 3.15 and the turbulence properties are shown in Table 3.5.

Table 3.4: Details of turbulence generating grids (Perforated plate)

Plate No.	Hole diameter (mm)	Hole number	Plate solidity
1	◯ 12.5 (Circle)	81	36.4%
2	◯ 12.5 (Circle)	64	50%
3	◯ 12.5 (Circle)	49	61.5%
4	◯ 20 (Circle)	25	50%
5	□ 11.2 (Square)	81	35%
6	□ 15.3 (Square)	49	26.6%
7	□ 22.6 (Square)	25	18.3%

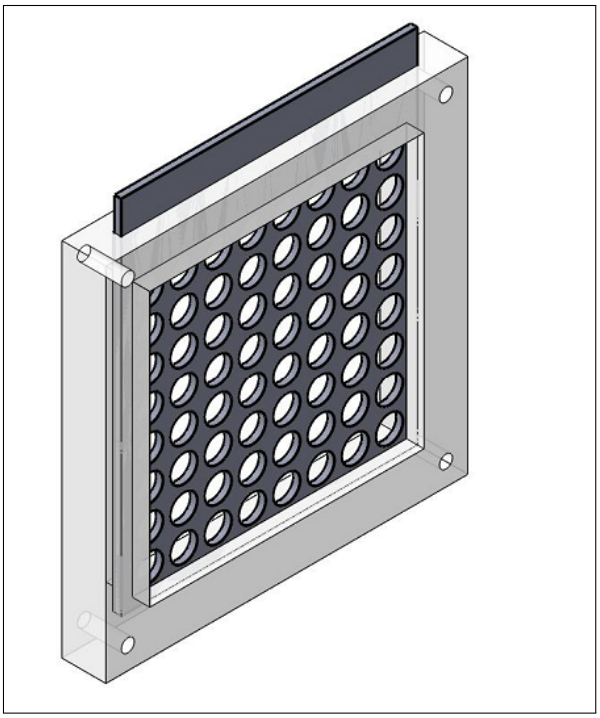

Figure 3.12: Diagram of the perforated plate in drawer.

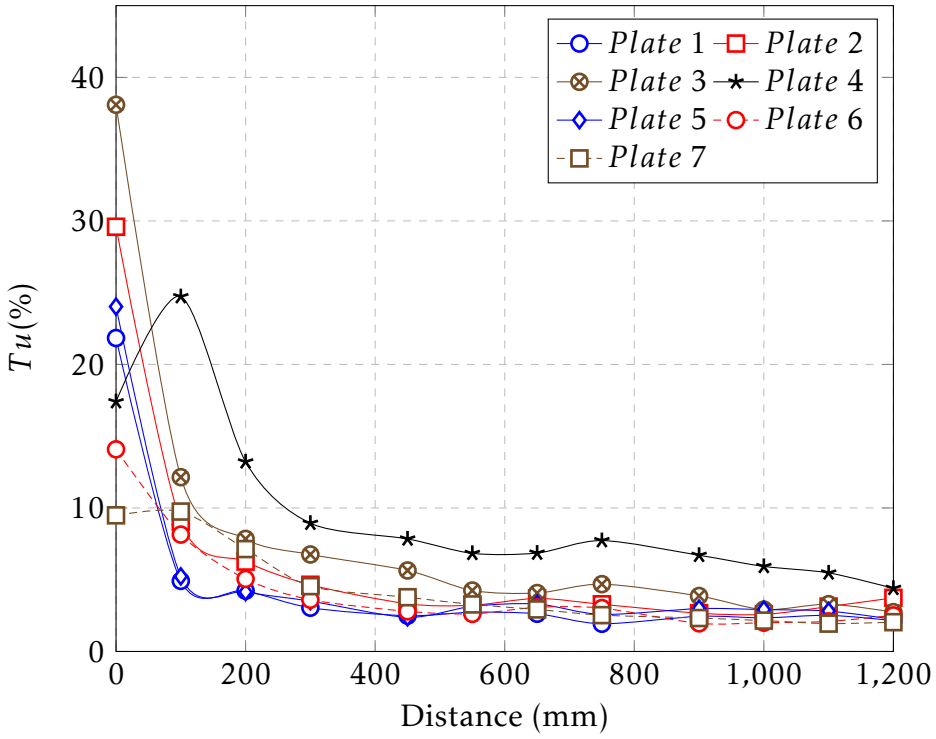

Figure 3.13: Variation of turbulent intensity with the distance of perforated plate from test section.

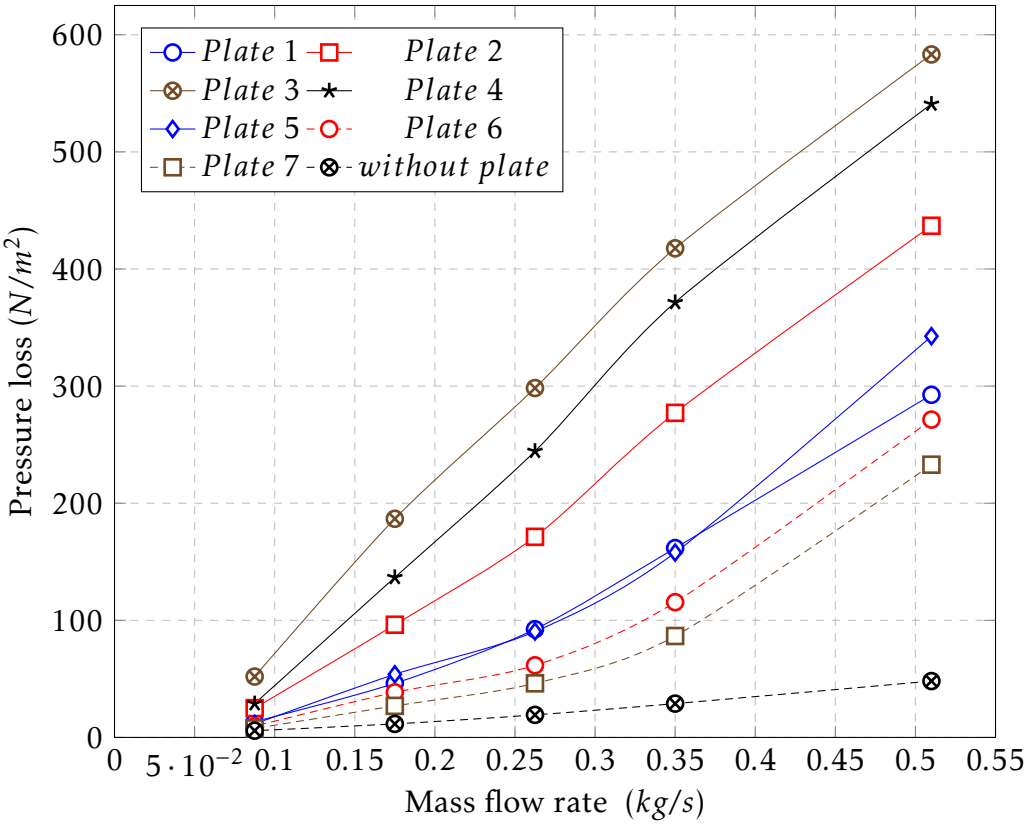

Figure 3.14: Pressure loss due to the different types of perforated plates at various flow rates.

Table 3.5: Details of turbulence intensity and integral length scale.

Plate No.	**Turbulent intensity** Tu (%)	**Integral length scale** Lx (mm)
without plate	2.2	≈ 55
1	4.9	7
5	5.2	11.1
6	8.1	15.3
7	9.7	25.2

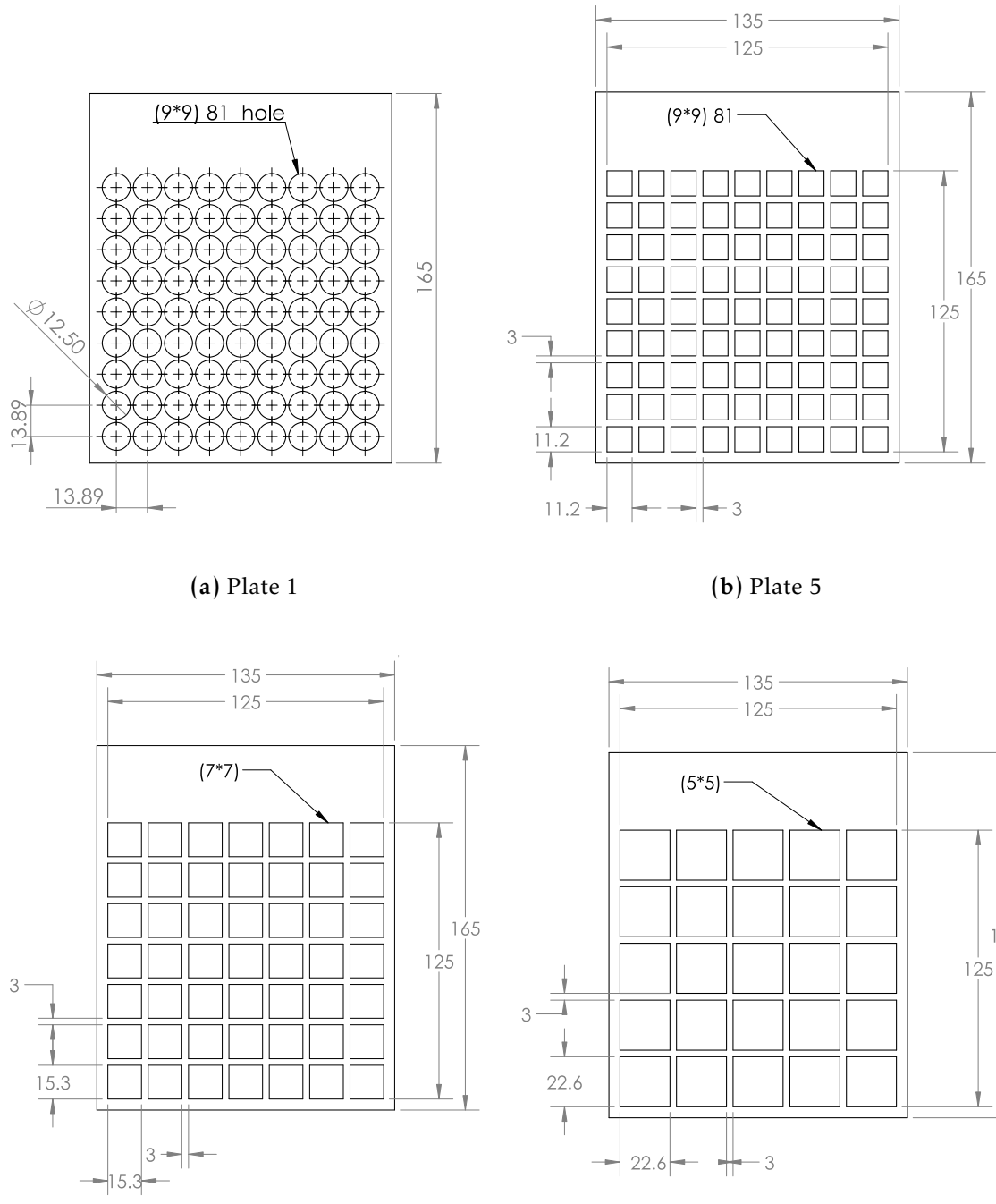

(a) Plate 1

(b) Plate 5

(c) Plate 6

(d) Plate 7

Figure 3.15: Schematic diagram of the perforated plates patterns (Plates 1,5,6, and 7. (All dimensions in mm)

3.4.3 Hot-Wire Probe Calibration and operating Principles

The hot wires calibration is done either by procedures depend on known heat transfer laws or a completely empirical procedure [105]. The empirical procedure consists of getting the hot wire output voltage as a function of many variables and this procedure is seldom used because of time consumption. The other procedure that based on a heat transfer law from the hot wire assumes for the case of forced convection and for isothermal fluids [106], the correlation in this method between the voltage output of the hot wire probe E and the velocity component U in the mean-flow direction is:

$$E = F(U) \tag{3.2}$$

The purpose of a calibration is to get a set of measurements point (E, U) over the selected velocity range. To guarantee appropriate accuracy it is common practice to perform $10-20$ readings of (E and U) equally spaced over the required velocity range [107].

A calibrator unit ($TSI, Inc., Model1125$) was used to calibrate the hot-wire. The schematic of the experimental set-up and the relevant dimensions are shown in Figure 3.16.

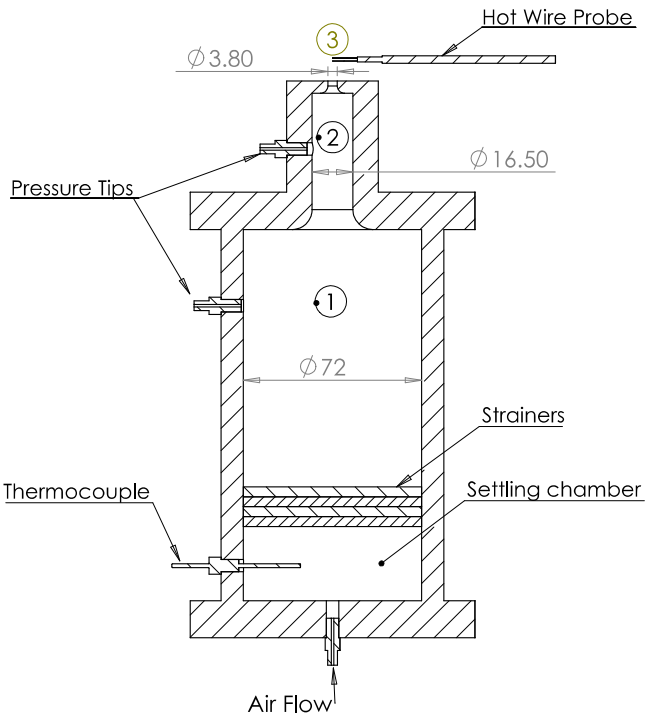

Figure 3.16: The schematic of the experimental set-up and the relevant dimensions

The calibrator contains a settling chamber with a contoured nozzle, allowing a very smooth and laminar air flow at the exit section and a set of control valves, pressure and temperature transducers and a probe holder, to calibrate the hot wire at the straight to the air flow and the center of the nozzle exit section.

Flow control valve is used to adjust the air flow. A K-type thermocouple is used to measure the air temperature inside the chamber. The temperature of air reached the constant temperature by passing it through the internal heat exchanger with auxiliary fan, the temperature was required to calculate the density of air and compensate the hot-wire calibration if it deviated from the over-heat adjustment. Air pressure was measured by a differential manometer which had a range of 0.00 Pa to 5000 Pa and an accuracy of ±1 % and is able to set velocities from 0.5 m/s to 91 m/s.

By applying Bernoulli's equation between two sections, the velocity can be calculated.

$$P_1 + \frac{1}{2}\rho u_1^2 + \rho g h_1 = P_3 + \frac{1}{2}\rho u_3^2 + \rho g h_3 \tag{3.3}$$

By using continuity equation between section 1 and 3, we get:

$$u_1 A_1 = u_3 A_3 \tag{3.4}$$

The diameter ratio between cylinder 1 and the nozzle is 18.95 (72/3.8), by assuming the maximum velocity in the nozzle is 25 m/s, we get:

$$u_1 = \frac{u_3 A_3}{A_1} = \frac{25 \times 14.44}{5184} \approx 0 \tag{3.5}$$

Position the hot wire (Point 3) is about one diameter (4 mm) downstream from the nozzle at the center, in that case, the static pressure is equal to the atmospheric pressure, therefore by measuring that ΔH is 0, the mean velocity, U, was calculated through the relationship:

$$P_{tot} - P = \frac{1}{2}\rho u^2 \tag{3.6}$$

where P_{tot} is the total pressure, P is the static pressure, and ρ is the air density.

To guarantee a sufficient accuracy for hot wire anemometer, it is necessary to reduce the calibration errors and select suitable curve fit. King 's law (Eq. 4.8) [108] has been used extensively to describe the correlation between the anemometer voltage and the fluid velocity. In this method, to get the selected velocity, it is important to use a data inversion process [109]. instead of King 's law many previous investigations George et al. [110] have indicated that good approximation may be obtained with a polynomial relationship:

$$u = c_1 + c_2 E + c_3 E^2 + c_4 E^3 + c_5 E^4 \tag{3.7}$$

where U is the air velocity, E is the hot wire anemometer voltage output and c_1 to c_5 are the polynomial constants. Here a fourth order polynomial has been used and is shown in Figure 3.17.

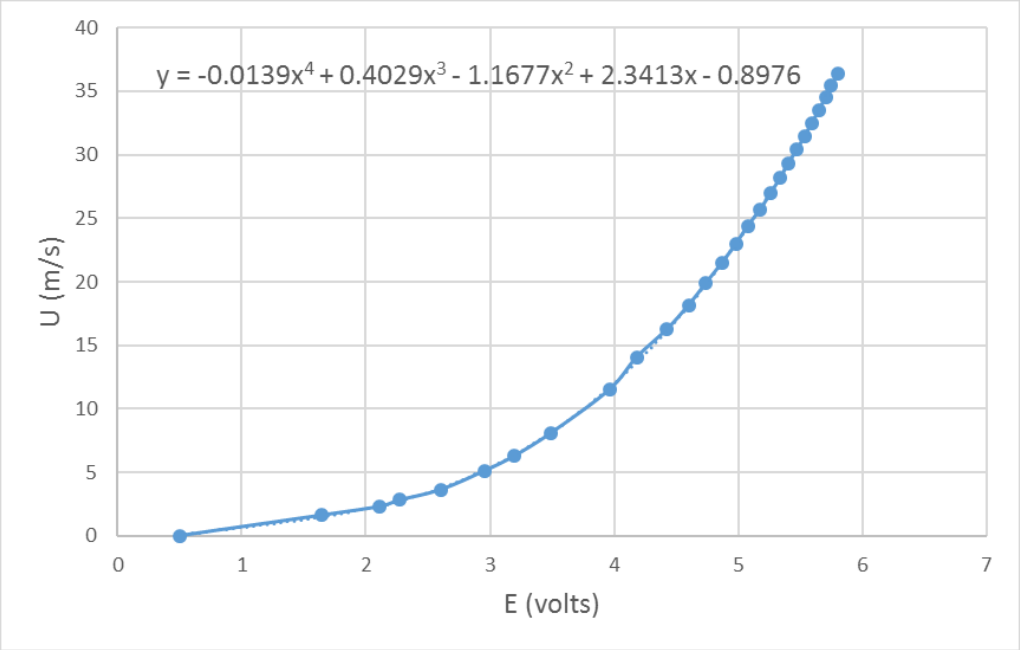

Figure 3.17: Hot-wire probe calibration curve

To reduce the effect of the velocity turbulent and the electronic noise, the voltage data were collected over 60 s period and the sampling rate was logged at 5 kHz. The turbulence level was less than 1% in the potential core. The hot wire calibration takes about two hours, and therefore the calibration had to be done repeatedly during the measurements because the hot wires tend to attract dust that leads to a change of the resistance of the wire then increasing the error percentage.

3.5 Surface roughnesses

Previous workers have used sandpaper strips or emery paper to give a homogenous roughness for flow measurement [111–114]. However this method was not suitable for heat-transfer experiments. In this work the roughness was produced by knurling the surface of the aluminium cylinder. Roughness manufactured by this technique results in regularly shaped of pyramids, with a rhomboidal base. The same method was used by **Achenbach** [17, 38]. Photograph of smooth and rough cylinders is shown in Figure 3.18.

The latest technology used to measure the roughness of the surface is the optical techniques and the computer vision systems which have many advantages compared to the stylus instruments. They are less expensive, a non-contact method (non-destructive technique) and have the capability of measuring roughness parameters in three-dimensional coordinates to survey the surface topography qualitatively. Therefore, Keyence VHX-5000 digital microscope was used to measure the pyramid features and also demonstrated some asymmetries, as it seen in Figures (3.20 - 3.23). Additionally, it was used to calculate the surface area of rough cylinders and compares it with the smooth one, Figure 3.24 shows digital photograph for calculating the surface area of middle roughness cylinder ($\epsilon/D = 3.25 \times 10^{-3}$).

3.5.1 Roughness statistically

Varied statistical parameters were utilized to analyse surface roughness information. Some of them are quickly described in below. Table 3.6 shows the statistical roughness parameters that considered having the strongest effect on the flow and Figure 3.19 shows the comparison between the roughness profile for the cylinders surfaces. For more details regarding these and other roughness parameters can be discovered in [115–118].

The arithmetic mean (effective height) of surface roughness in Table (3.6) is the average absolute values of surface height deviations from the mean value.

$$Mean\ (\epsilon) = \frac{1}{N}\sum_{i=1}^{N}|h_i - \bar{h}| \tag{3.8}$$

where $\bar{h}$ is the mean surface elevation ($\sum h_i/N$) and N denote the data points number in the surface scan. This essential parameter which is an effective and simple tool for looking at roughnesses of surface. It was used to determine the relative surface roughness of the cylinders in this study.

the root- mean-square (ϵ_{rms}) is another tool to quantify the surface height data distributed around the mean height, computed as

$$\epsilon_{rms} = \sqrt{\frac{1}{N}\sum_{i=1}^{N}(h_i - \bar{h})^2} \tag{3.9}$$

The impacts of peaks and valleys on the boundary layer growing are expected to be different. The roughness pattern trend toward peaks or valleys is determined by the parameters height distribution skewness (Sk) which is mathematically described as the third moment of the height distribution of elements about their mean value:

$$Sk = \frac{1}{N.\epsilon_{rms}^3}\sum_{i=1}^{N}(h_i - \bar{h})^3 \tag{3.10}$$

Negative values of skewness indicate that the roughness distribution is on average less from the mean elevation in comparison to elements depths (i.e. The surface height distribution It tends to be a flat surface with pits). Conversely, positive values indicate the inverse (a flat surface with lumps).

The kurtosis is the fourth order central moment and indicates to the degree of data spread to describe the flatness of the roughness density function, it is quantified by:

$$Ku = \frac{1}{N.\epsilon_{rms}^4}\sum_{i=1}^{N}(h_i - \bar{h})^4 \tag{3.11}$$

A normal distribution has kurtosis 3. If the surface with a relatively large number of pits and bumps (more peaked than a normal distribution), the kurtosis will be greater than 3. Whereas the kurtosis is less than 3 if an approximately flat surface with some pits and bumps.

Table 3.6: Dimensions and surface statistics of the roughness patterns.

/	**Rough**	**Middle**	**Fine**	**Smooth**
Lower roughness height (mm)	0.32	0.14-0.15	0.03-0.04	/
Larger roughness height (mm)	0.39	0.165-185	0.11	/
Arithmetic mean,Eq.(3.8), (Effective height) (μm)	361.96	162.55	56.61	6.23
ϵ_{rms} (μm),Eq.(3.9)	406.56	196	65.34	7.04
Skewness (Sk),Eq.(3.10)	-0.58	-0.15	-0.28	0.635
Kurtosis (Ku),Eq.(3.11)	2.13	1.747	1.68	2.92
Pitch (mm)	1.6	1.1	0.65	/
Helix angle	75^o	75^o	75^o	/
(A_{Rough}/A_{Smooth})	**1.4**	**1.2**	**1.126**	1
Relative roughness (ϵ/D)	7.25×10^{-3}	3.25×10^{-3}	1.13×10^{-3}	1.25×10^{-4}

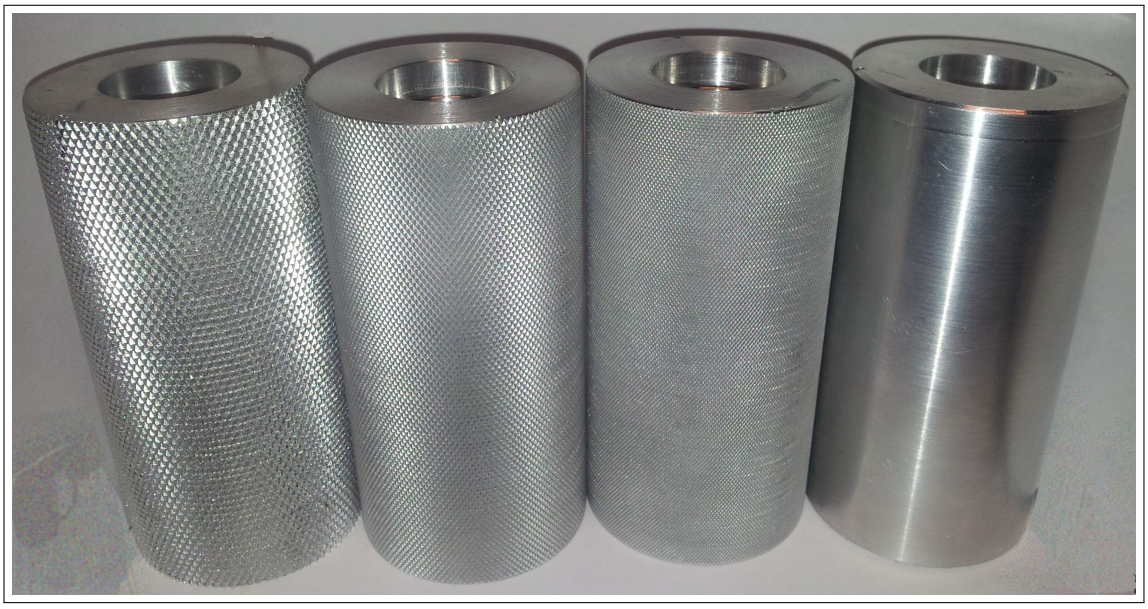

Figure 3.18: Smooth and rough cylinders.

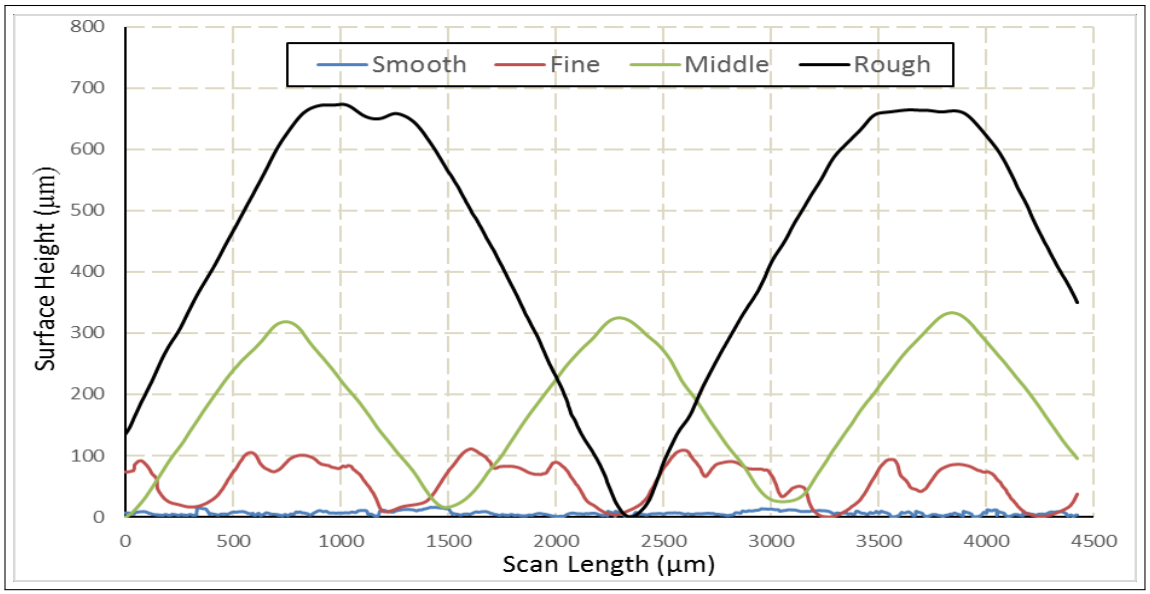

Figure 3.19: Surface profiles of cylinders.

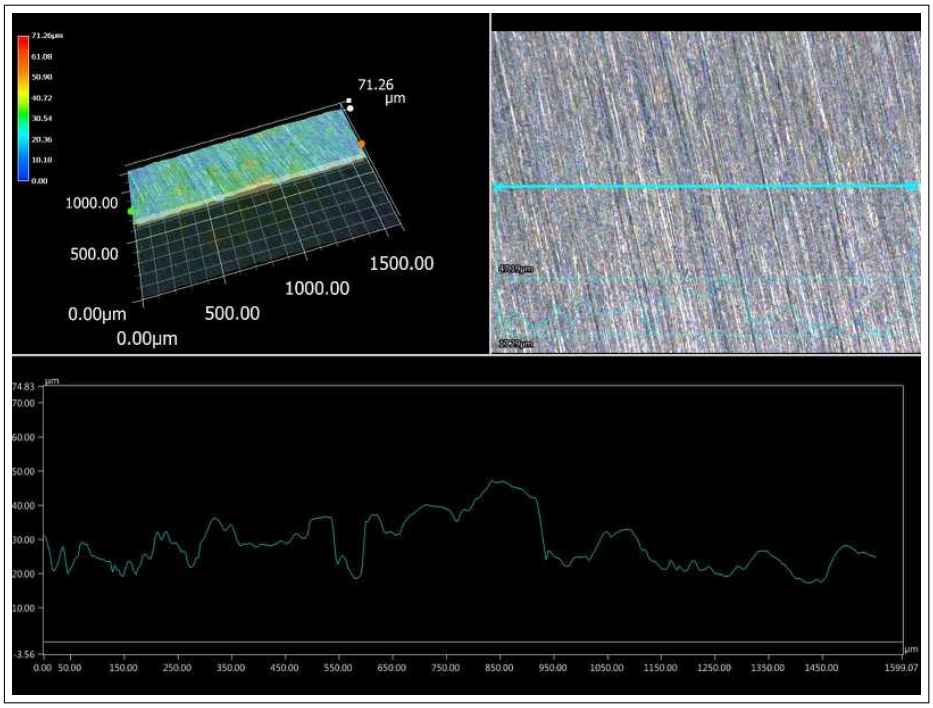

Figure 3.20: Keyence VHX digital microscope photographs , and surface profile of smooth cylinder.

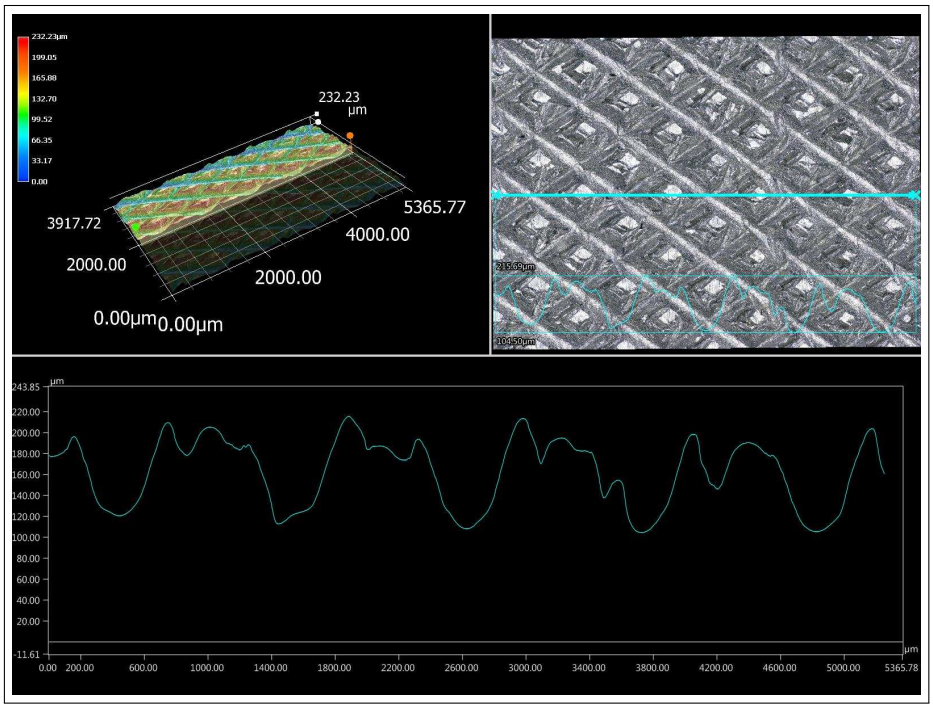

Figure 3.21: Keyence VHX digital microscope photographs , and surface profile of fine roughness cylinder ($\epsilon/D = 1.13 \times 10^{-3}$).

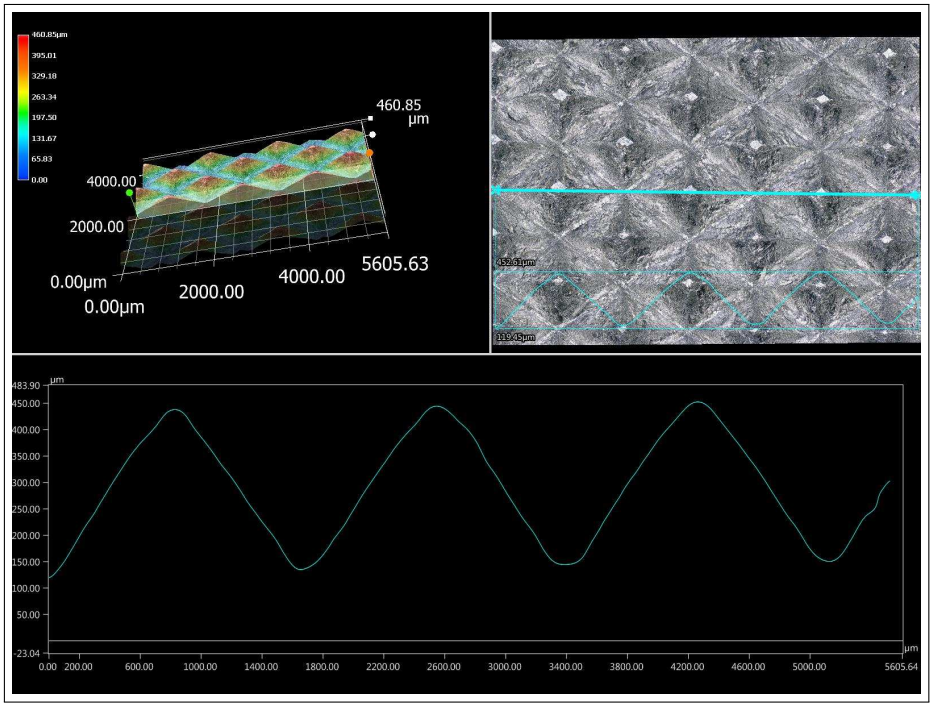

Figure 3.22: Keyence VHX digital microscope photographs , and surface profile of middle roughness cylinder ($\epsilon/D = 3.25 \times 10^{-3}$).

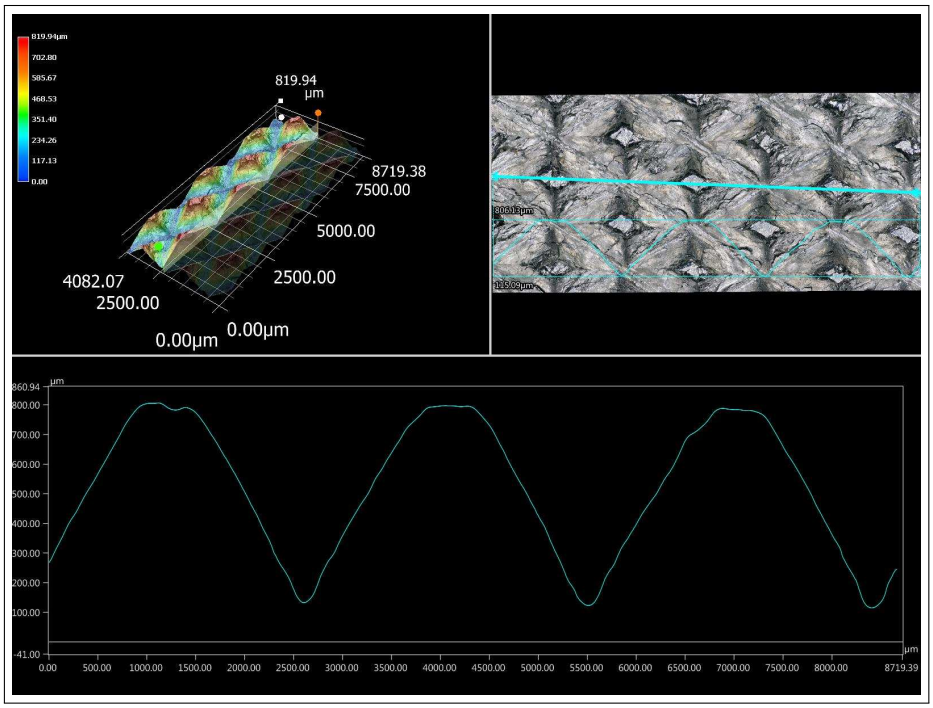

Figure 3.23: Keyence VHX digital microscope photographs , and surface profile of high roughness cylinder ($\epsilon/D = 7.25 \times 10^{-3}$).

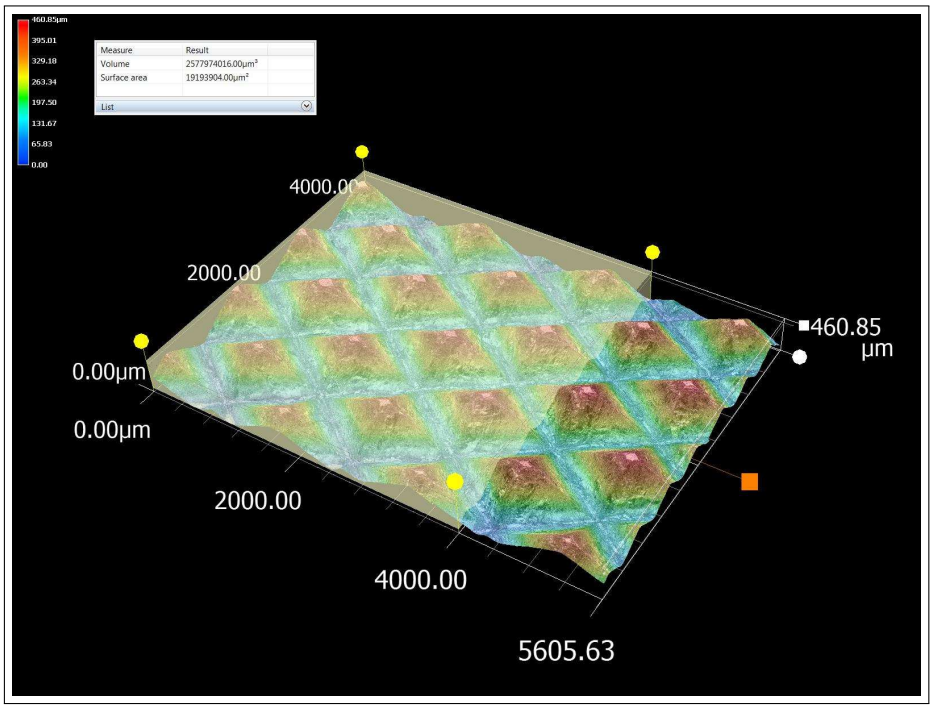

Figure 3.24: Keyence VHX digital microscope photograph for calculating the area of middle roughness ($\epsilon/D = 3.25 \times 10^{-3}$).

3.6 Data collection

3.6.1 Heat Transfer Data Collection

Overall heat transfer rate.

The convection heat transfer coefficient, h, is calculated by measurement the power input to the internal cartridge heater, Q_{tot}, with computing the effects due to conduction, Q_{cond}, and radiation, Q_{rad}. In steady state conditions, the energy dissipated from the cylinder is equal to the power input, which is equal to the rate of convection heat that transferred to the flow, conduction within the cylinder, and radiation to the surrounding. Thus the heat supply and heat losses from the test cylinder can be written as:

$$Q_{tot} = Q_{conv} + Q_{cond} + Q_{rad} \tag{3.12}$$

Due to the insulators at cylinder ends that have low thermal conductivity and the integration of guard heaters and end insulators, conduction heat loss,Q_{cond}, is neglected.

Thus, the heat transfer by forced convection is estimated as:

$$Q_{conv} = hA_s(T_s - T_\infty) \tag{3.13}$$

Where T_s is the cylinder surface temperature, T_∞ is the free stream temperature taken in the wind tunnel. A_s is the surface area of the cylinder. the heat loss by radiation from cylinder surface to the ambient air is expressed as:

$$Q_{rad} = \varepsilon\sigma A_s(T_s^4 - T_\infty^4) \tag{3.14}$$

Where ϵ is the emissivity of the aluminum surface, which is equal approximately 0.03 [36] and σ is the Stefan-Boltzmann constant($\sigma = 5.67 \times 10^{-8} W/m.K^4$). The heat transfer by radiation is comparatively small in this work, in general, it is less than 5% of the overall heat transfer from the cylinder. To decrease the fixed error in the calculations, heat loss by radiation is included. Substituting Eqs. (3.14) and (3.13) into (3.12) with neglect the conduction loss $Q_{cond} = 0$, that gives;

$$h = \frac{Q_{tot} - \varepsilon\sigma A_s(T_s^4 - T_\infty^4)}{A_s(T_s - T_\infty)} \tag{3.15}$$

The current $I[A]$ and voltage $V[V]$ of the direct current that used for heating of the cylinder are measured. We assumed that the electrical power $P_e = VI$ is fully

converted into heat Q_{tot}. The Nusselt number is defined as the ratio of convection heat transfer to fluid conduction heat transfer at the same conditions.

$$N_u = \frac{hD}{k_{air}} \tag{3.16}$$

Local heat transfer rate.

To calculate the local values of Nu three quantities must be measured:

- The local heat transfer rate, Q_L
- The local wall temperature, $T_s(\theta)$
- The ambient temperature, T_∞

Local heat transfer rate on the heated cylinder and its surface temperature together can be immediately measured by using Micro-Foil Heat flow Sensor. Thus the heat transfer coefficient is estimated as:

$$h_L = \frac{q_L - \epsilon\sigma(T_s^4 - T_\infty^4)}{(T_s - T_\infty)} \tag{3.17}$$

After determining the distribution of the local heat flux and for reducing the error caused by high-temperature differences and highly non-isothermal surfaces, the overall heat transfer coefficient could be determined by dividing the mean value of the local coefficient of heat flux by the mean value of the local surface temperature:

$$h = \frac{\frac{1}{\pi}.\int_0^\pi q_L d_\theta}{\frac{1}{\pi}.\int_0^\pi \Delta T_L d_\theta} \tag{3.18}$$

3.6.2 Flow data collection

For the present study the Reynolds number (the ratio of the inertial forces to the viscous forces for the flow conditions) is defined as:

$$R_e = \frac{Inertia\ force}{Viscous\ force} = \frac{\frac{\rho U^2}{D}}{\frac{\mu U}{D^2}} = \frac{\rho UD}{\mu} = \frac{UD}{\mathcal{V}} \tag{3.19}$$

where U, the upstream velocity (mean velocity), was measured using a Pitot- static tube and HWA system. D, the diameter of the cylinder , was measured by using a digital vernier, and $\mathcal{V}$,kinematic viscosity was specified from tables [36], all air properties were determined at the mean film temperature of ($T_f = T_s + T_\infty/2$) and standard atmospheric pressure. Air at a temperature of about 23^oC was used. Thus the results were presented only for a Prandtl number of 0.71.

3.7 Experimental Procedure

In the absence of airflow, the cylinder was heated electrically until its surface temperature stabilized at 210^oC $(\pm 0.5^oC)$, Figure 3.25 shows heating curve for a typical experiment.

After ensuring the test cylinder surface temperature has reached steady state, the wind tunnel was started and the gate valve was set to the required mass flow rate. At each specific mass flow rate, the cylinder was rotated through 180^o in increments of 10^o. Figure 3.26 shows the coordinate system (0^o at the front of stagnation point). At each angle, the surface temperature was measured. Another set of measurements involved measurement of heat flux density by the heat flux sensor and turbulent level by hot wire anemometer. All these reading was noted after steady state condition is reached (for more details see Appendix C.2). To minimise the mistakes in the data, no less than one hundred value (about 2-3 min) of the heat flux and thermocouple outputs were taken and found the middle value of each reading. Figure 3.27 shows the output fluctuation of heat flux sensor during this period.

Preliminary tests were performed For two power input (Q_{tot} = 5 and 61 watts) to observe the temperature distribution around the circumference of the cylinder. These tests were carried at a flow velocity of 23 m/s and are shown in Figure 3.28. In both cases, the temperature climbed from 0^o reaching a peak value at approximately 90^o and then dropped till the angle was 180^o. The temperature difference was higher for the higher heat flux. As shown by **Achenbach** [92] the maximum temperature difference occurs where the Nusselt number is at its smallest on the surface. The relative temperature difference around the cylinder was about ±4%. This is in good agreement with the values predicted of **Achenbach** [92] and **rao** [119]. It may be concluded that the tests have been performed at the constant surface temperature boundary condition.

The effect of input power on the total heat-transfer rate is presented as a function of the Reynolds number in Figure 3.29. As shown in this Figure that increasing Q_{tot} (from 5 Watt to 61 Watt) does not affect the heat transfer coefficient i.e. Nu number does not depend on Q_{tot}. Changed in total heat transfer Q_{tot} in eq (3.15) leads to increase temperature difference $(T_s - T_\infty)$ and unchanged in h . This will be the case for forced convection, when the temperature difference may effect on physical properties that have only a small influence.

Distributions of the local Nusselt number over the circumference of cylinder at main stream velocity 23 (m/s) shown in Figure 3.30. The results showed that heat transfer distribution is almost symmetric with regard to the lower and upper half of the cylinder due to that the equal main flow in the lower and upper halves of the channel. Therefore, for the rest of the study, the tests are only going to cover one-half of the cylinder.

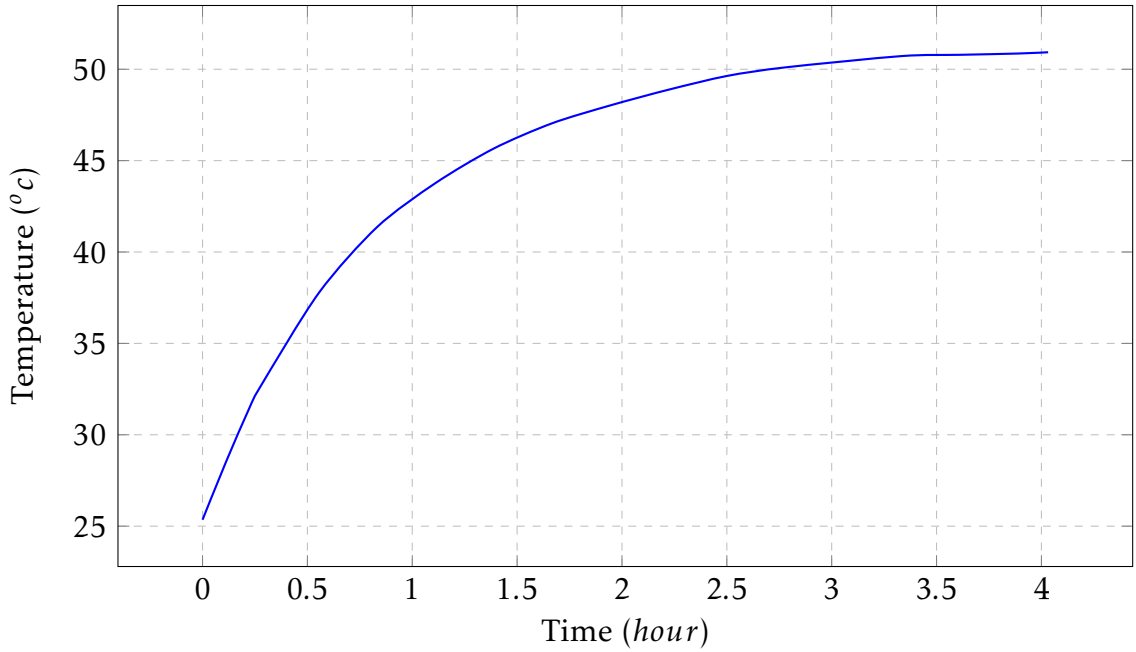

Figure 3.25: Required time to reach the steady state for cylinder surface temperature with power input 3.9 watts at free convection.

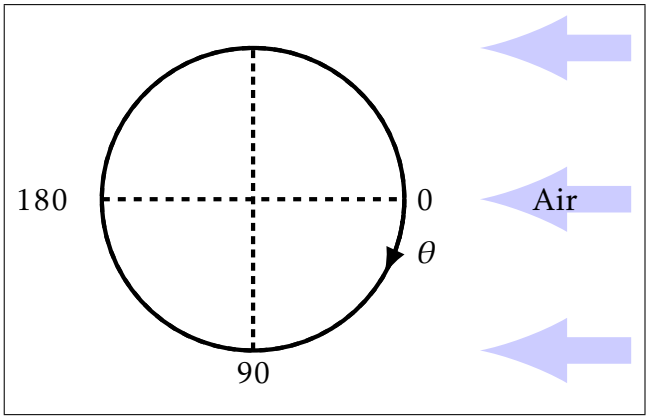

Figure 3.26: The air flow direction with respect to the cylinder.

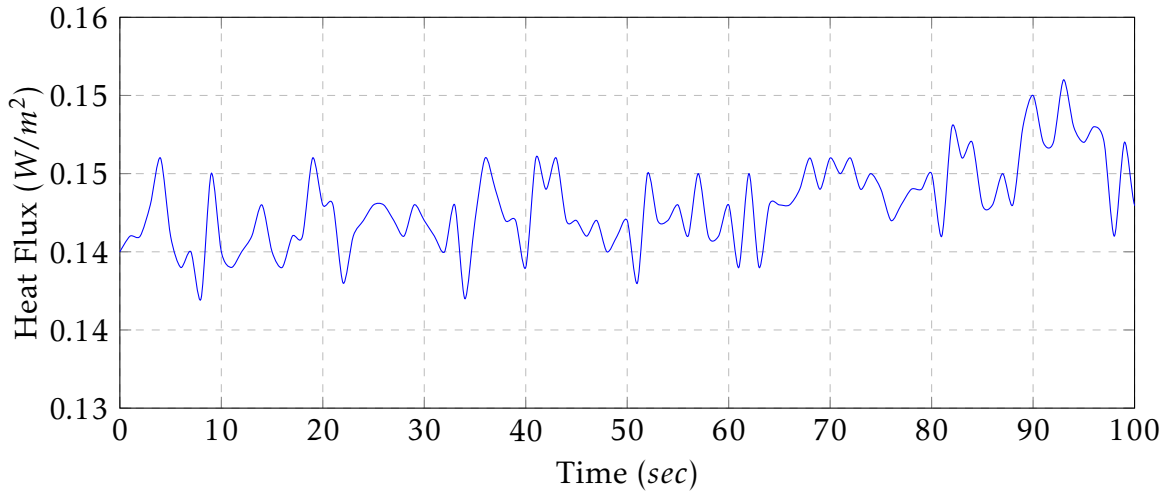

Figure 3.27: Fluctuation of the heat flux measurement at mean stream velocity 23 (m/s).

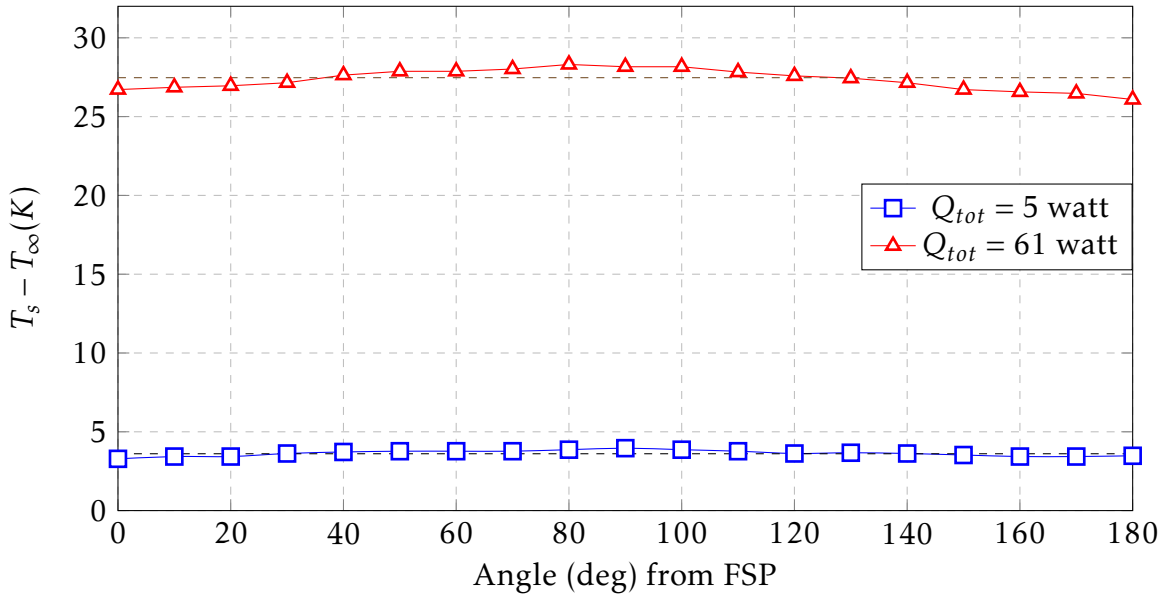

Figure 3.28: Temperature difference ($T_s - T_\infty$) around the circumference of the circular cylinder at power inputs of 5 and 61 W.($U_\infty = 23(m/s)$).

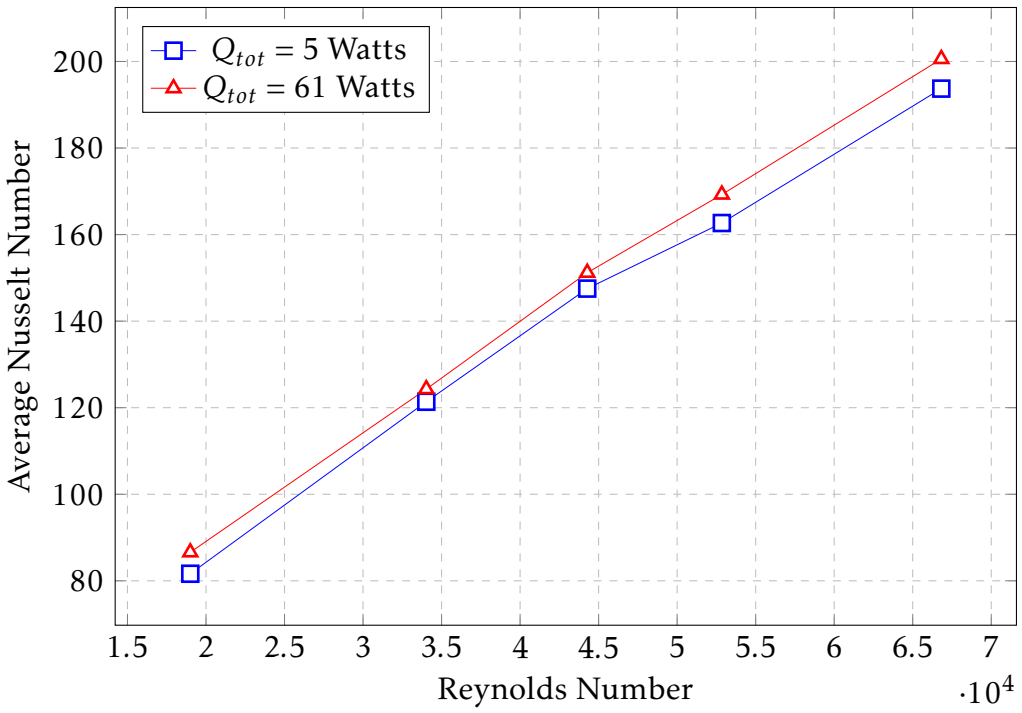

Figure 3.29: Distributions of the local Nusselt number for 360 deg over circumference of cylinder ($U_\infty = 23(m/s)$).

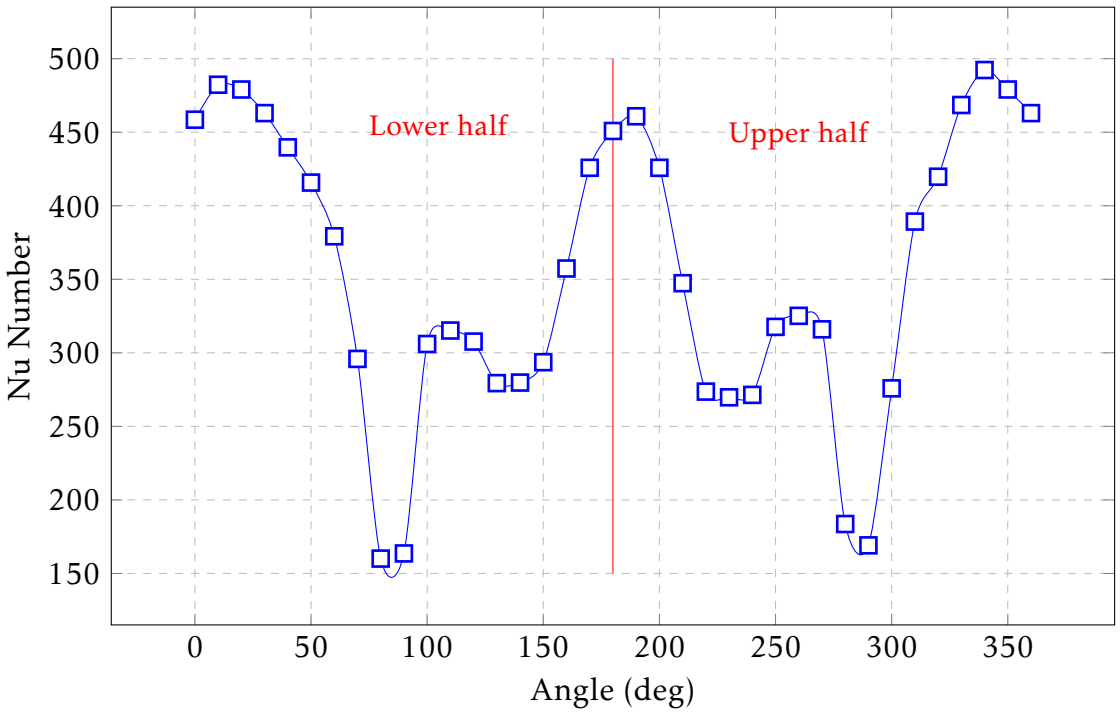

Figure 3.30: Distribution of local Nusselt number in 360 deg at $U_\infty = 23(m/s)$.

CHAPTER 4

Experimental results and discussion

4.1 Smooth Cylinder

4.1.1 Total heat transfer

Shown in Figure 4.1 is the average Nusselt number plotted against the Reynolds number for the two blockage ratios studied. Also shown are empirical correlations and experimental results from previous studies. The Nusselt number was found to increase with Reynolds number in all cases. However, considerable variation in Nu can be observed. The empirical correlations generally predict a lower Nu than was measured in this work. The other experimental results are both lower and higher than the results from this study, However, there are differences in both blockage ratio and turbulence levels in the main stream which are likely to impact on Nu.

A larger blockage ratio results in higher velocities around the cylinder circumference resulting in increased Nu although high blockage ratios are considered undesirable as they indicate that the walls of the wind tunnel are influencing the results. The turbulence level in the main stream also increasing heat transfer rate. The reported values of blockage ratio and turbulence level for the data presented in Figure 4.1 are given in Table 4.1. Shown in Figure 4.2 is the effect of different turbulent levels on Nu for a blockage ratio, $\beta = 0.2$.

For making a better comparison Table (4.2), which lists the percentage of relative deviation of the average Nusselt number at different Re number. The percentage deviation is calculated according to the following expression.

$$Deviation\ (\%) = \left| \frac{Nu_{exp} - Nu_{corr}}{Nu_{exp}} \right| \tag{4.1}$$

It can be seen from Table 4.2 that at high Reynolds number, the Nusselt number is approximately between 8% and 36% higher than the predictions. The present data are lower than the results for lower Reynolds number between 2% – 35% compared with **Sanitjai** [11] and **Perkins** [89] respectively and 3.2% higher compared with **Churchill and Bernstein** [84]. Generally, present results are similar to those of other workers but they were performed at higher blockage ratios so they are slightly higher. This gives confidence in going forward. The rig is behaving as expected and this is satisfactory data to act as a baseline for next cases.

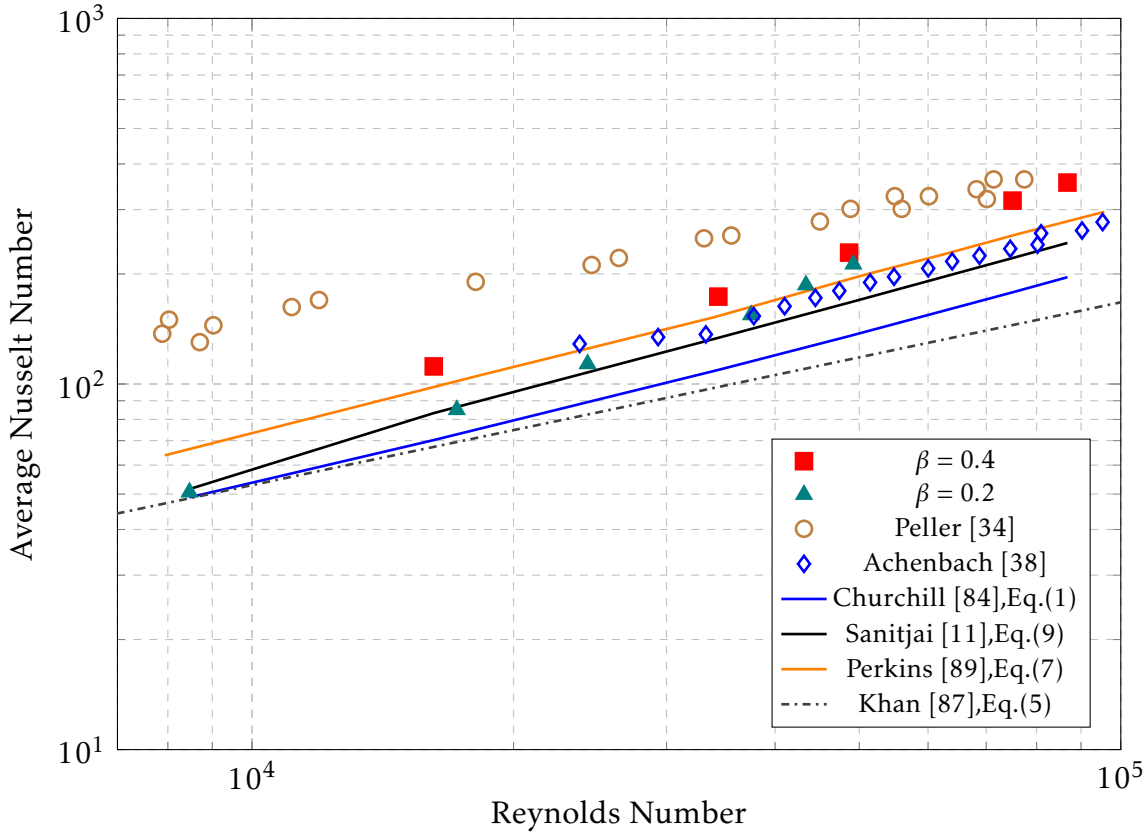

Figure 4.1: Comparison of the current results for the average Nusselt number with previous investigators.

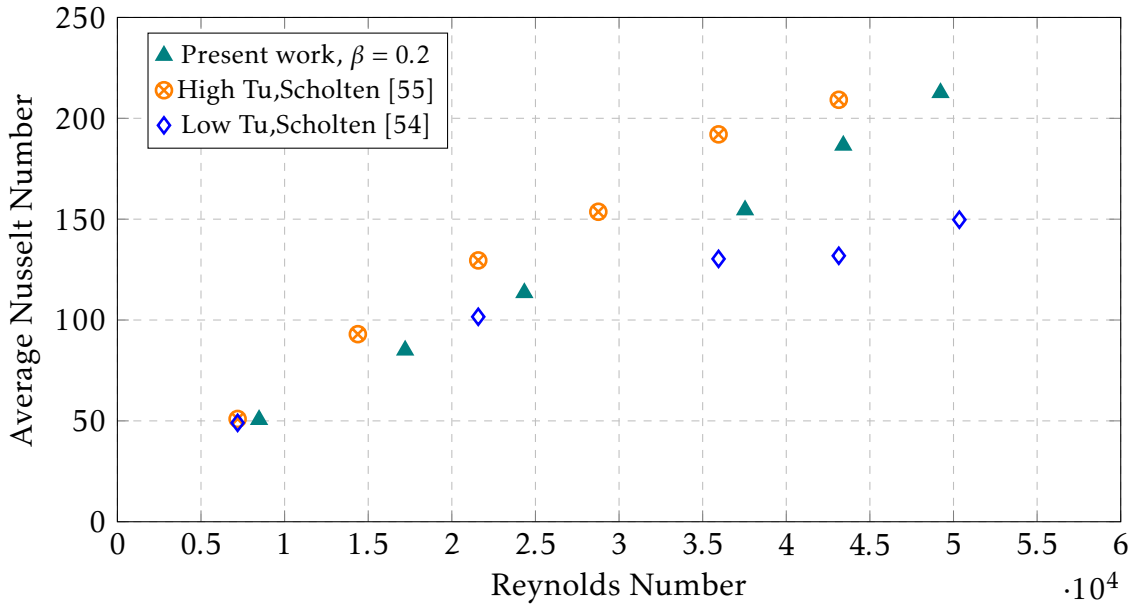

Figure 4.2: Effect of turbulence levels on average heat transfer.

Table 4.1: The factors of blockage ratio and turbulence levels for various investigators.

Auther	β (%)	Tu (%)
Perkins , Leppert, [89],Eq.(7)	**(20.8 , 31.2 , 41,2)**	**2.9**
Peller et al. [34]	**30**	**(4 - 12)**
Buyruk, [12]	**(13.1 - 84.3)**	**(1 - 2)**
Scholton A, [54]	**19.7**	**0.5**
Scholton B, [55]	**19.7**	**(6.7 - 8.5)**
Churchill , Bernstein, [84],Eq.(1)	~ 0	~ 0
Khan et al, [87],Eq.(5)	~ 0	~ 0
Achenbach, [92]	**16.4**	**0.45**
Sanitjai , Goldstein, [11],Eq.(9)	**14**	**0.3**
Present work	**(20 , 40)**	**2.2**

Table 4.2: Comparison of average Nusselt numbers from measurements with values obtained from Churchill and Bernstein [84] , Sanitjai [11] and Perkins [89]

Present work (β = 20%)	Churchill and Bernstein	Deviation (%)	Sanitjai	Deviation (%)	Perkins	Deviation (%)
50.6	49	**3.2**	51.6	**-2**	68.4	**-35.1**
85	72.7	**14.4**	86.5	**-1.8**	98.4	**-15.8**
113.5	89	**21.6**	107.5	**5.3**	122	**-7.4**
154.5	115.2	**25.4**	141.4	**8.5**	162.5	**-5.2**
186	126	**32.5**	155.1	**16.8**	179.5	**3.8**
212.6	136	**36**	168	**21**	195.6	**8**
Mean Deviation	**22.2** %		**7.9** %		**-8.6** %	

4.1.2 Local heat transfer

The local Nu_θ at $\beta = 40\%$ and Tu= 2.2 are shown in Figure 4.3 plotted against versus angular position between the front stagnation point ($\theta_{Fsp} = 0$) and the rear stagnation point ($\theta_{Rsp} = 180^o$). Data is shown for a range of Reynolds numbers from 16200 to 87000.

The variation of heat transfer coefficient around the cylinder can be roughly split into three divisions, $0^o < h < 85^o$, $85^o < h < 135^o$ and $135^o < h < 180^o$. The maximum Nu_θ is achieved near the front stagnation point (Fsp) for all Reynolds numbers. The heat transfer coefficient decreases after the front stagnation point reaching a minimum value at about $\theta = 90^o$ (at the side of the cylinder). As discussed in Section 2.2, this decrease in Nu_θ is due to the increasing the thickness of the laminar boundary layer along the surface which increasing in the thermal resistance at the surface. In the second regime, $85^o < h < 135^o$ the value of Nu_θ starts to increase. The minimum Nu_θ changes with Re, it is at 90^o for the lowest values of Re and then moves forward to $\approx 85^o$ as the highest values of Re. Two types of behaviour can now be observed. At the lowest Reynolds numbers tested the Nu_θ remains constant or only slow increases as the angles increases to 130^o. At higher values of Re (greater than or equal to 34500) the Nu_θ increases rapidly reaches a maximum and then decreases (Sec. 2.2). In next final part of the surface $\approx 130^o$ to 180^o the value of Nu_θ increases for all values of Reynolds numbers.

Shown in Figures 4.5 and 4.4 are the angular variation in Nu at $\beta = 20\%$, where the local Nusselt number was compared with previous works at same blockage ratio with high and low turbulence levels, Figure 4.4. As shown in this Figure, the present results correspond with the prior studies [54, 55] and the aforementioned turbulence variations significantly affect the local Nusselt number.

Figure 4.6 shown both the front and rear part contribution of heat transfer. From 0^o to 90^o (front part) is where the higher heat transfer occurs. The slope of lines in Figure 4.6a indicated that the heat transfer of the front part is higher at low Re and starts to decrease with increasing Re. As a result of a high mass flow rate, the mixing and turbulence increase at the back of the cylinder and thus the contribution from the rear half of the cylinder was slightly higher compared to that from the front half. While at low Re number, the free shear layer may reattach. however, the periodic swirls do not become fully turbulent and the swirl forming zone is away from the rear cylinder surface. Hence, the impact of periodic swirls and the re-attached free shear layer on the Nusselt number are comparatively small. That effect is more obvious at the big blockage ratio because of reattaching region (85^o to 135^o). Similar observations were made the previous work of [8, 11, 13]

4.1.3 Effect of blockage ratio on heat transfer

The total Nusselt number was seen to increase with the blockage ratio. The effect of the blockage ratio (β =0.4 and 0.2) can be seen on local heat transfer by comparing Figure 4.3 and Figure 4.4, respectively, It is seen from these Figures that the location of the boundary layer separation depends on the blockage ratio, as higher blockage causes separation to be delayed. At $\beta = 0.4$, Figure 4.3, the minimum local Nusselt number is moved to the downstream side of the cylinder about by 10°. This is due to the increasing the velocity around the cylinder outside the boundary layer which leads to changes in the distributions of velocity and pressure inside the boundary layer.

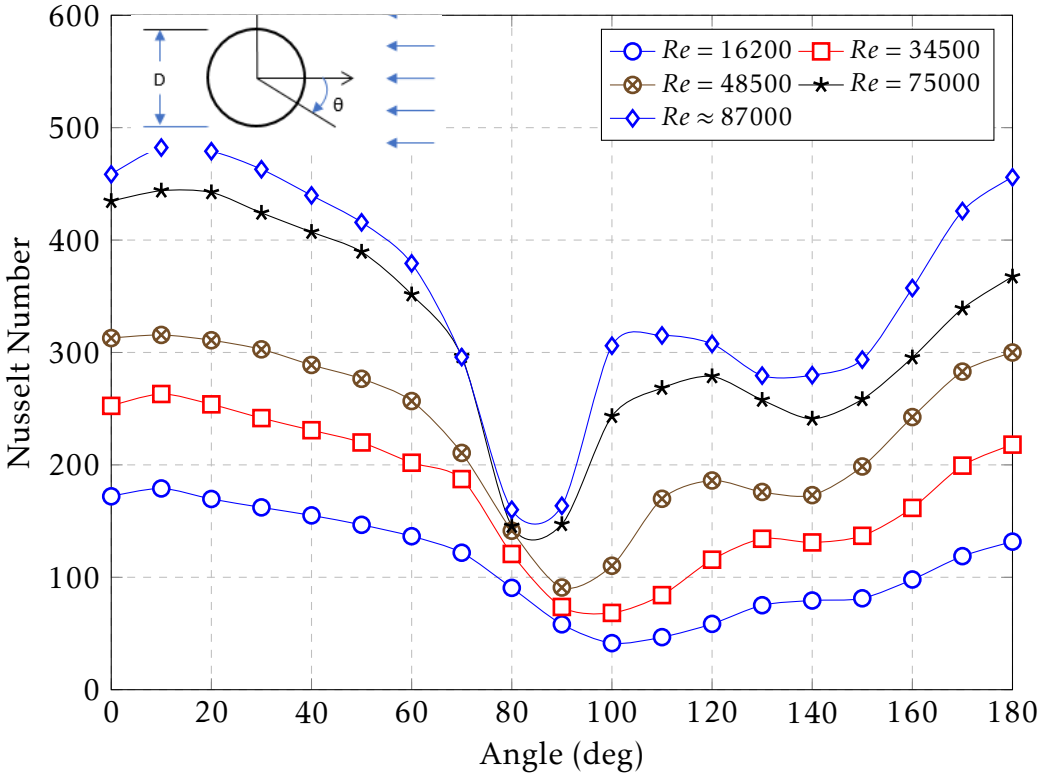

Figure 4.3: Variation of local Nusselt number on the smooth cylinder at $\beta = 0.4$.

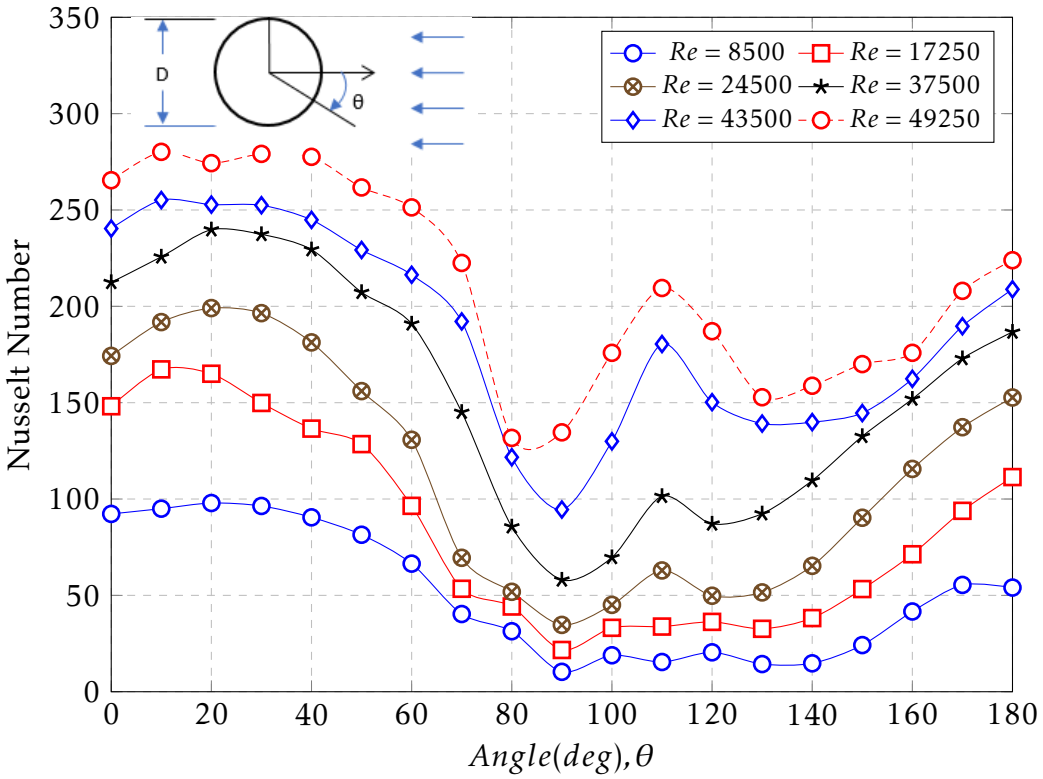

Figure 4.4: Variation of local Nusselt number on the smooth cylinder at $\beta = 0.2$.

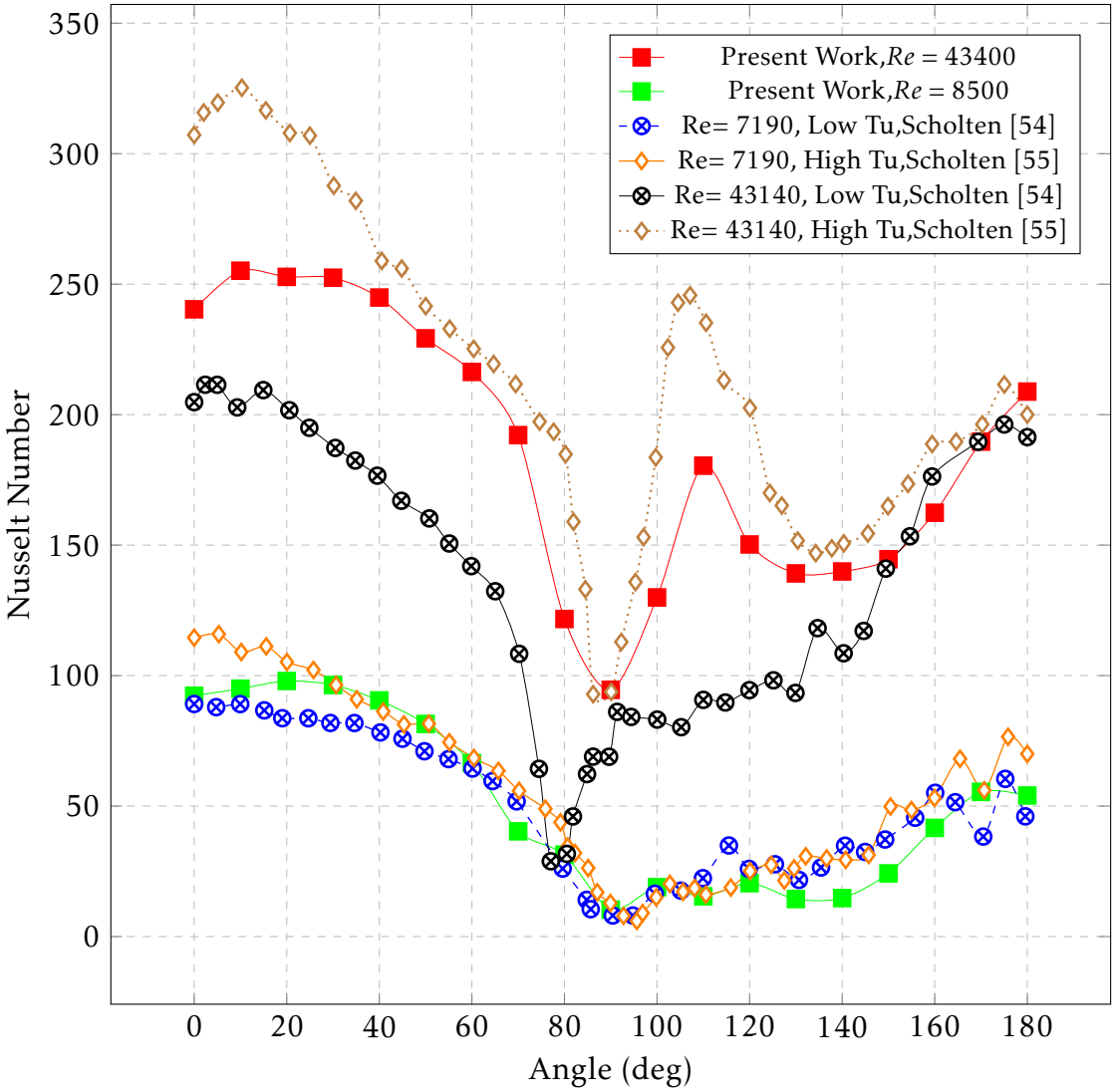

Figure 4.5: Effect of turbulence levels on local Nusselt number variation at $\beta = 0.2$.

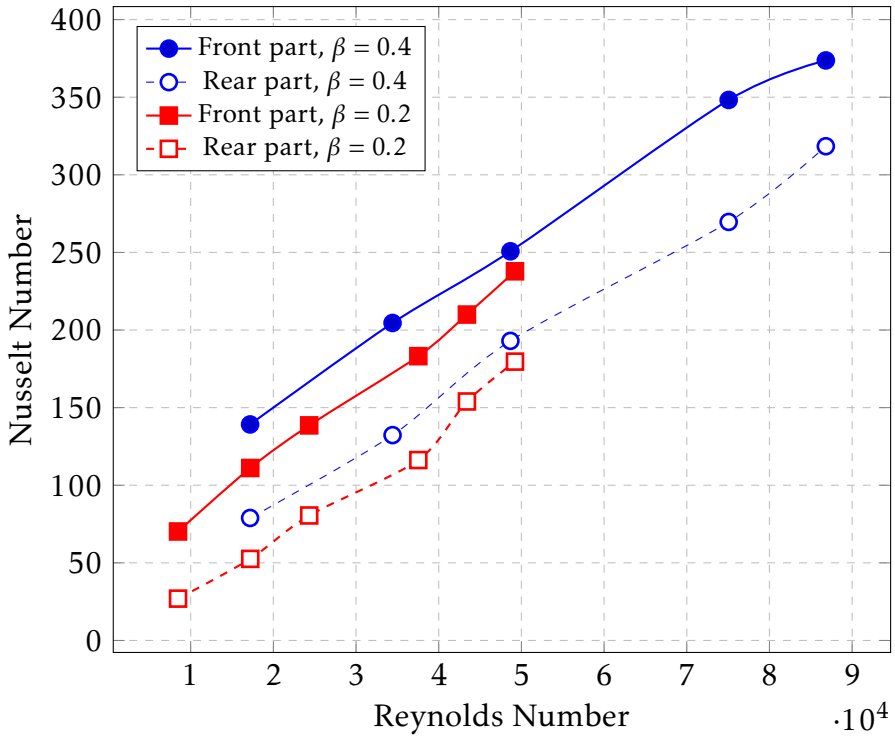

(a) Average heat transfer on the front and rear part.

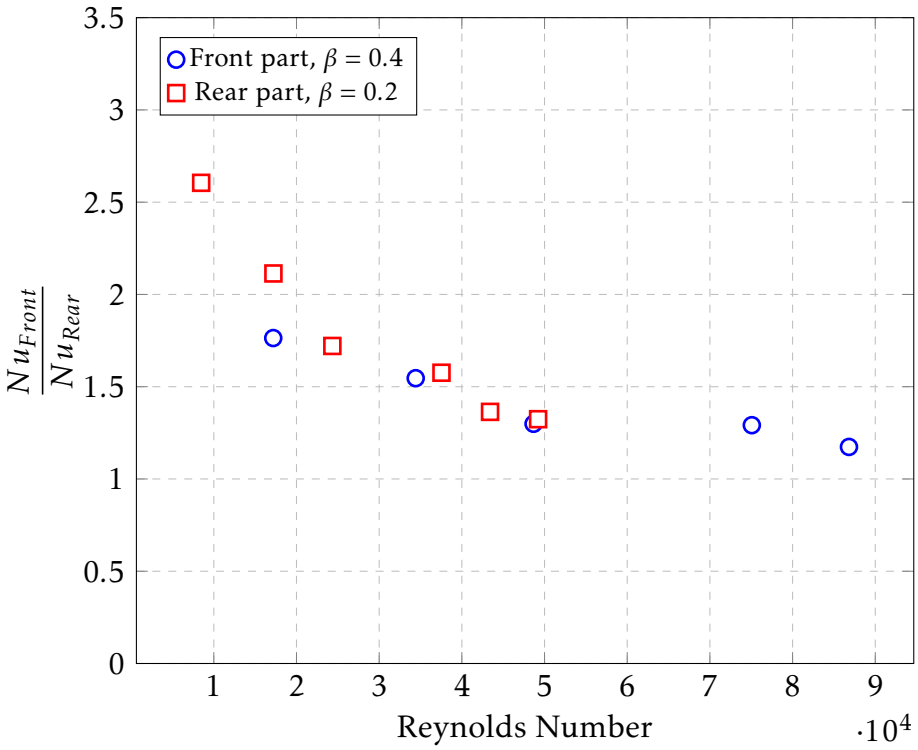

(b) A ratio of Nu in front part to the rear part.

Figure 4.6: Heat transfer rate in the front and rear part of a cylinder at blockage ratio (β=0.2 and 0.4).

4.2 FST Effect

4.2.1 Total heat transfer

Shown in Figure 4.7 are the overall Nusselt numbers for different values of Tu. As the Reynolds number increased so do the Nusselt number. The Nusselt numbers also increased with Tu. The measurements performed with the grid are noticeably bunched together in comparison to the dataset where a turbulence generating grid was not used. The relationship between heat transfer and turbulence intensity at a constant Reynolds number is shown in Figure 4.8. It can be concluded that increasing the turbulence intensity is associated with an increase in the mean heat transfer and the results indicate that the largest increases in Nusselt number occur at the highest value of turbulence intensity. This seems reasonable on the basis of conclusions of previous studies which indicate that increases in free turbulence intensity lead to increase heat transfer rate at Reynolds number larger than 10^4 [43, 58]. Also, the results in Figure 4.8 indicate that for a constant Reynolds number there seems to be almost a linear relationship between heat transfer and turbulence intensity level in the range, $2.2 < Tu < 9.7$ percent.

4.2.2 Local heat transfer

Effect of turbulent intensity on local Nusselt number around the smooth cylinder for different Reynolds numbers are shown in Figures (4.9 - 4.13).

Shown in Figure 4.9 are the circumferential Nu_θ number for a Reynolds number of $1.6x10^4$ for increasing Tu. Maximum values of Nu_θ number occur at $\theta_{Fsp} = 0^o$ (the front stagnation point) and at $\theta_{Rsp} = 180^o$ (rear stagnation point). From $\theta = 0^o$ the Nu_θ number decreases this is associated with the increase of the boundary layer thickness from 60^o to 90^o , the local Nu_θ number drops rapidly on account due to changes in the velocity profile of main-stream and its effect on the boundary layer. The minimum value of Nu_θ occurs at 100^o , it then increases in the rear part of the cylinder is because of the swirl impacts in the cylinder wake region as discussed in Sec.2.2. The grid makes little difference in local Nusselt number at this Reynolds number, therefore, increasing turbulence intensity from 2.2% to 9.7%, the total Nusselt number increases about 5.4%.

The results for the next Reynolds number tested Re ($3.5x10^4$) are shown in Figure 4.10. The increased turbulence in the flow makes a clear difference in two distinct area from 0^o to 60^o, and from 90^o to 140^o. The effect of the freestream turbulence leads to distortion of the boundary layer and of the velocity profile within it, due to this effect the heat transfer rate increase in the laminar flow region from 0^o to 60^o. At around 90^o the separation occurs. The heat transfer sharply increases after separation point and achieve a peak about $\theta = 120^o$ at low Tu (2.2) and $\theta = 110^o$ for other Tu, this effect is due to a flow re-attachment where new free

stream air is moved nearer to the cylinder. In the region after the reattachment, the boundary layer continues developing and becomes plainly turbulent then separates again about $\theta \approx 140^o$.

The Nu_θ number distribution at high Re $7.5x10^4$ and $8.7x10^4$ are shown in Figures 4.12 and 4.13 respectively. At Tu = 2.2 (no grid), the Nu number steadily decreases from the front stagnation point (Fsp) until it achieves a minimum at the separation point. From $\theta \approx 85^o$ *to* $\theta \approx 150^o$ a hump in the heat transfer data can be observed. This has been attributed to secondary vortices in the cylinder wake [54]. From $\theta \approx 150^o$, the Nu_θ number increases associated with the unsteady flow and the irregular vortex shedding in the wake. At Tu of 9.7%, there is a minimum value Nu_θ associated with the separation point moves toward downstream at $\theta \approx 90^o$. A 'hump' in the heat transfer results occur corresponding to the re-attachment of the flow stream. The flow becomes unsteady (turbulent) and lastly, turbulent boundary layer separates at around 150^o where the second least Nu_θ number occurs. After the second separation point, the heat transfer increase because of increasing the turbulent.

The data from this study shows good agreement with previous studies [57,120]. Similar magnitudes of heat transfer increase have been reporting (Re = $3x10^4$ for $Tu < 5\%$) and similar changes to the heat transfer across the cylinder have been observed (the appearance of a (hump) in the wake).

The results presented above can be summarized in Figure 4.14. Free stream turbulence results in increases in the heat transfer around the cylinder by deformation the boundary layer and making it turbulent. An increase of Tu from 2.2% to 9.7% is not just accompanied by an increment of the heat transfer rate on the front part of the cylinder where the flow is laminar, but the boundary layer becomes turbulent and rather than separating at $\theta = 90^o$, separates at about $\theta = 150^o$, this helps to increase total Nu number about 13 %, at Re = $7.5x10^4$.

4.2.3 Impact of turbulence length scale on heat transfer

The impact of turbulence length scale L_x on Nu_θ number at constant Re number and Tu is displayed in Figure 4.15. Increasing the turbulent length scale from 0.007m to 0.012m resulted in few changes to the heat transfer distribution. There is some impact before and then after separation. The impact on the total Nu number is slight. These results are in line with those in the literature where both an increase and decrease in the heat transfer due to changes of length scale have been reported.

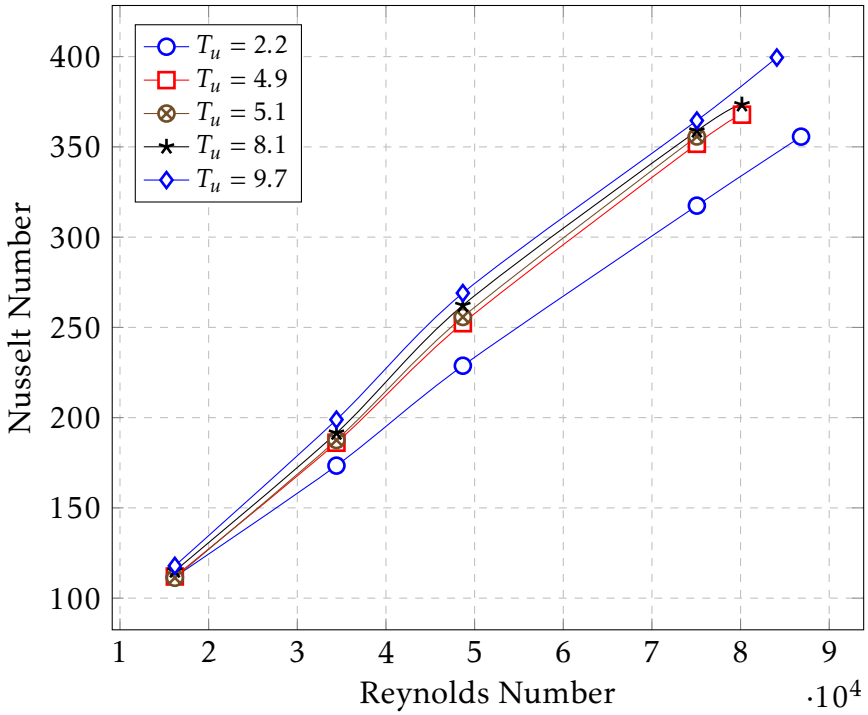

Figure 4.7: Relationship between Nu number and Re number with different turbulence level.

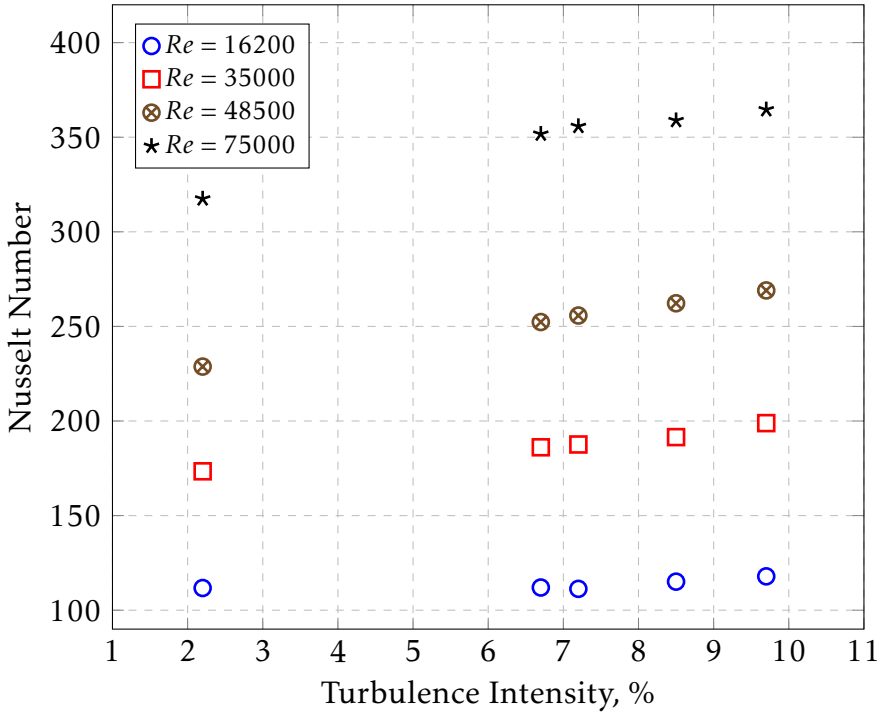

Figure 4.8: Effect of turbulence intensity on Nu number at different Re number.

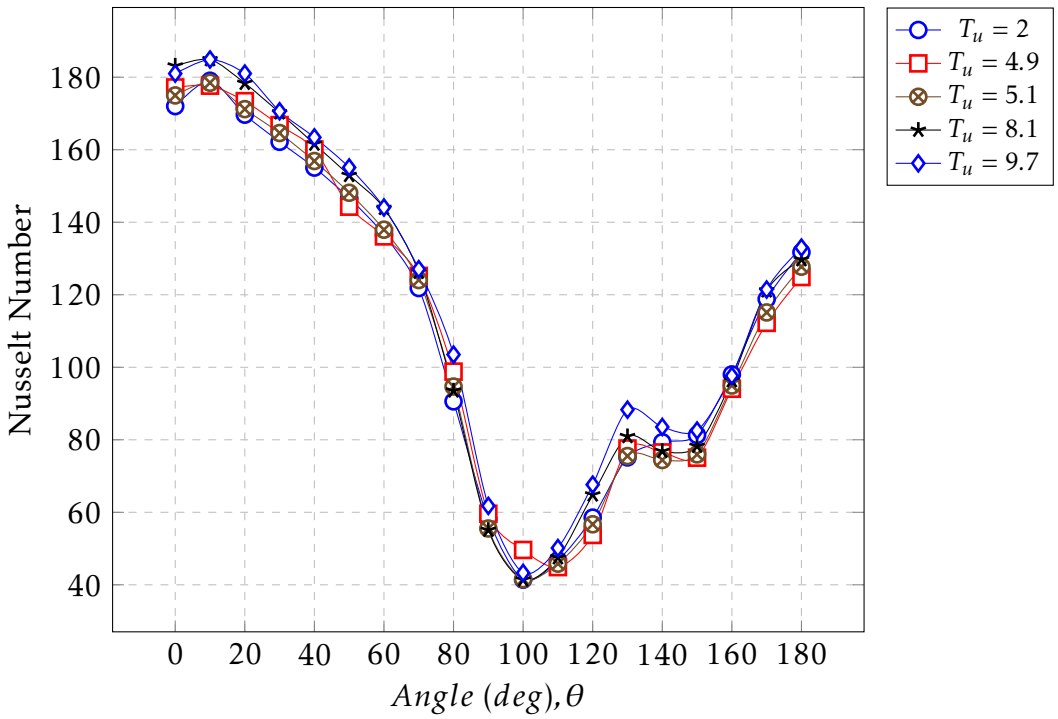

Figure 4.9: Variation of local Nusselt number on the smooth cylinder at $Re = 1.6x10^4$.

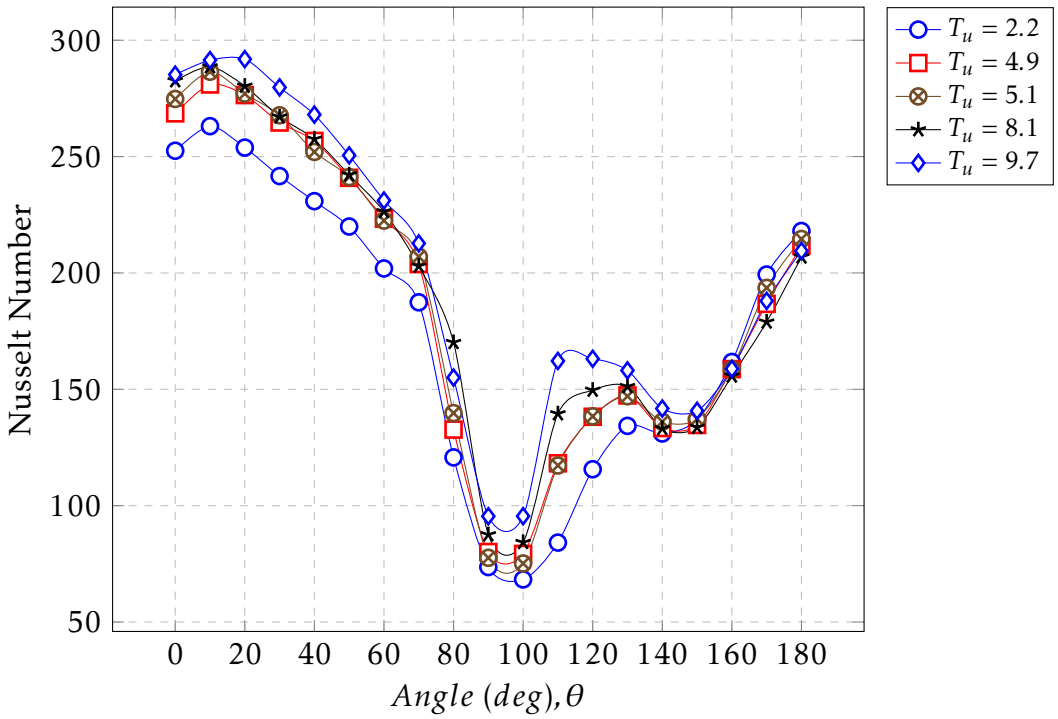

Figure 4.10: Variation of local Nusselt number on the smooth cylinder at $Re = 3.4x10^4$.

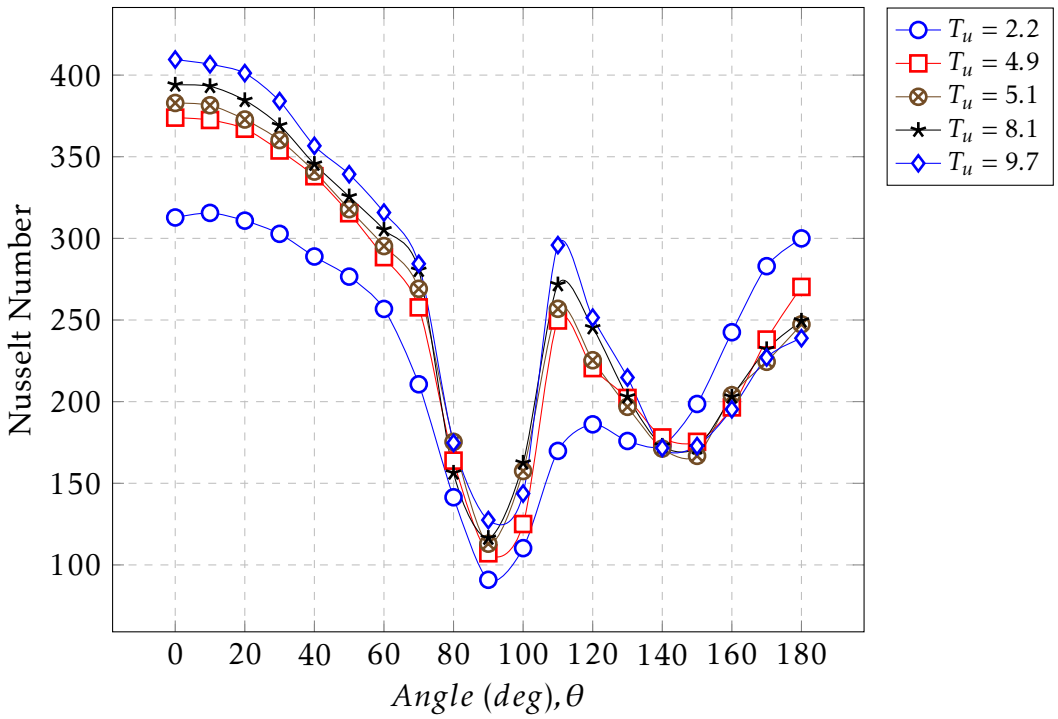

Figure 4.11: Variation of local Nusselt number on the smooth cylinder at $Re = 4.8x10^4$.

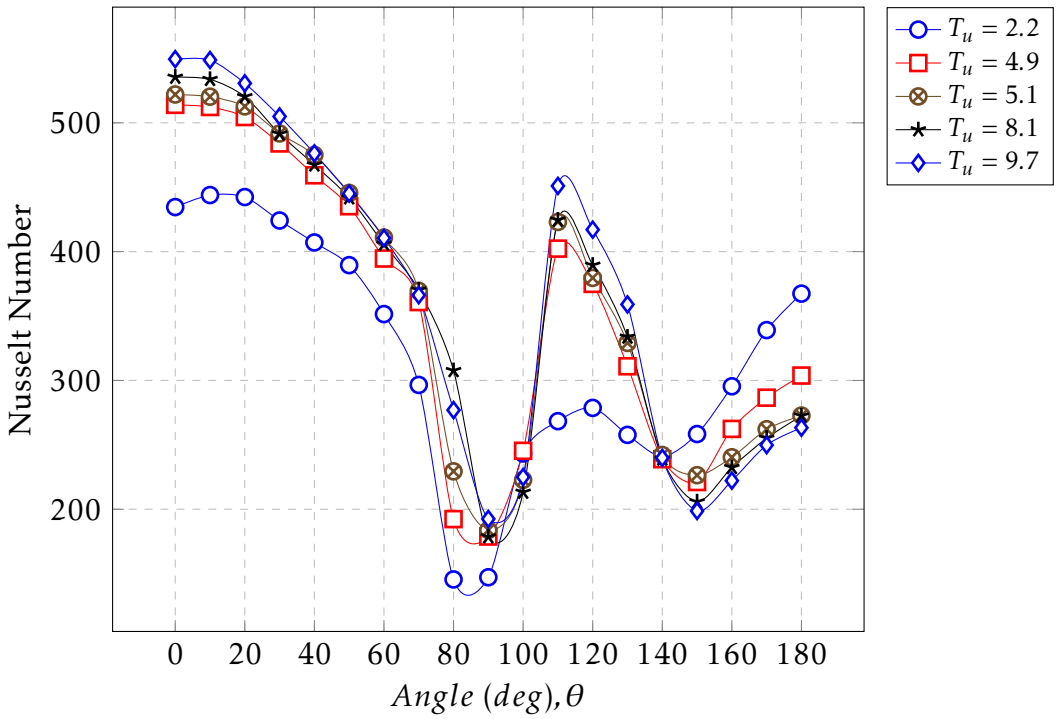

Figure 4.12: Variation of local Nusselt number on the smooth cylinder at $Re = 7.5x10^4$.

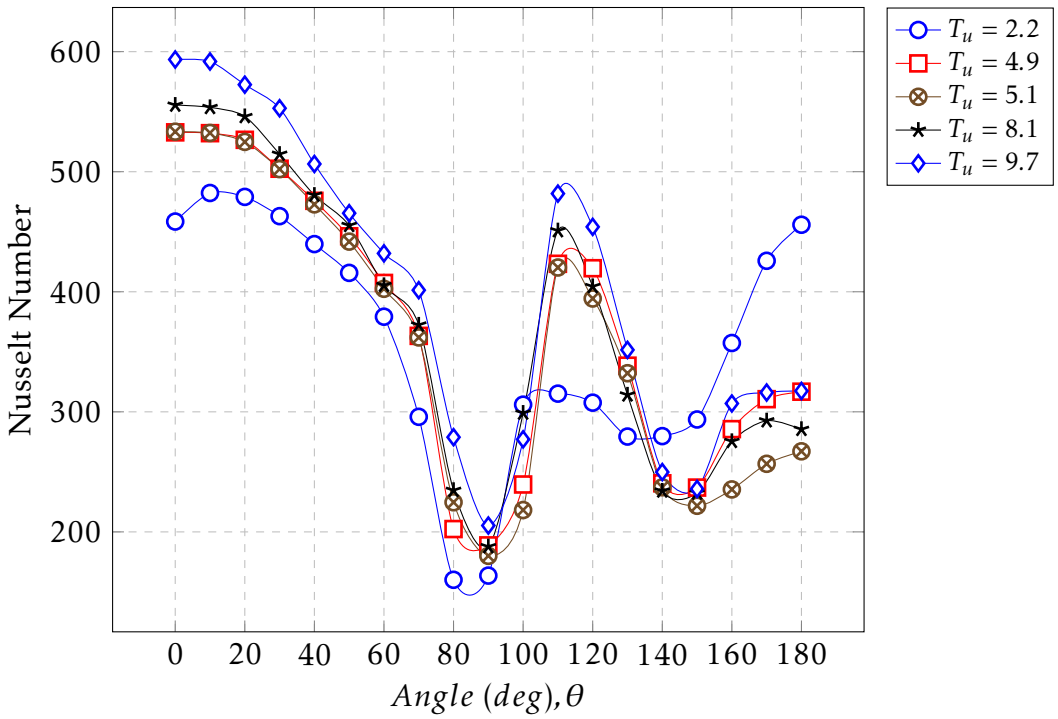

Figure 4.13: Variation of local Nusselt number on the smooth cylinder at $Re = 8.7x10^4$.

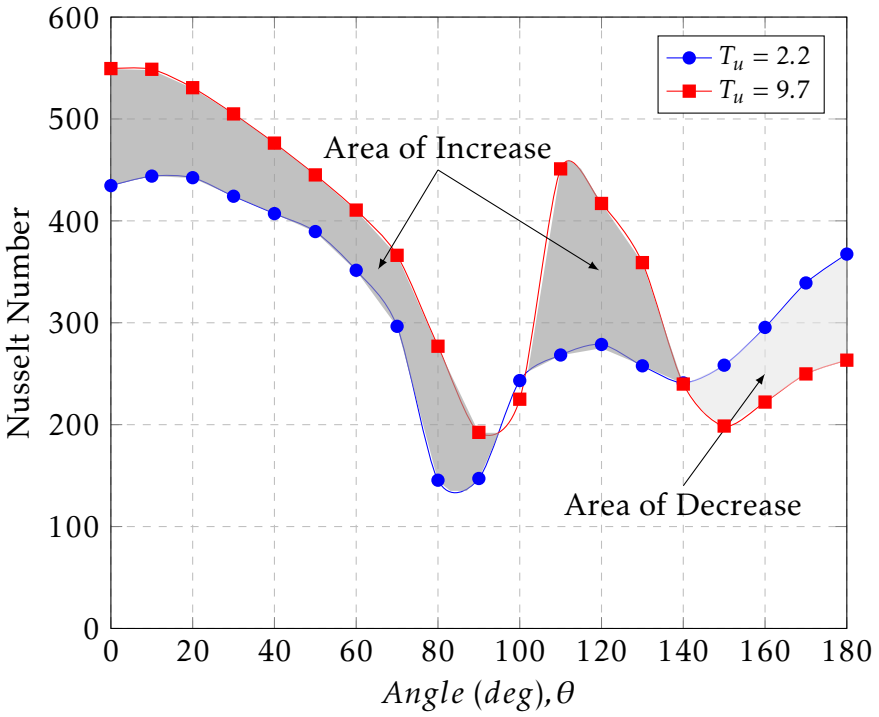

Figure 4.14: Comparison of the local variation of Nu number around a cylinder for turbulence intensity 2.2% and 9.7% at Re number $7.5x10^4$.

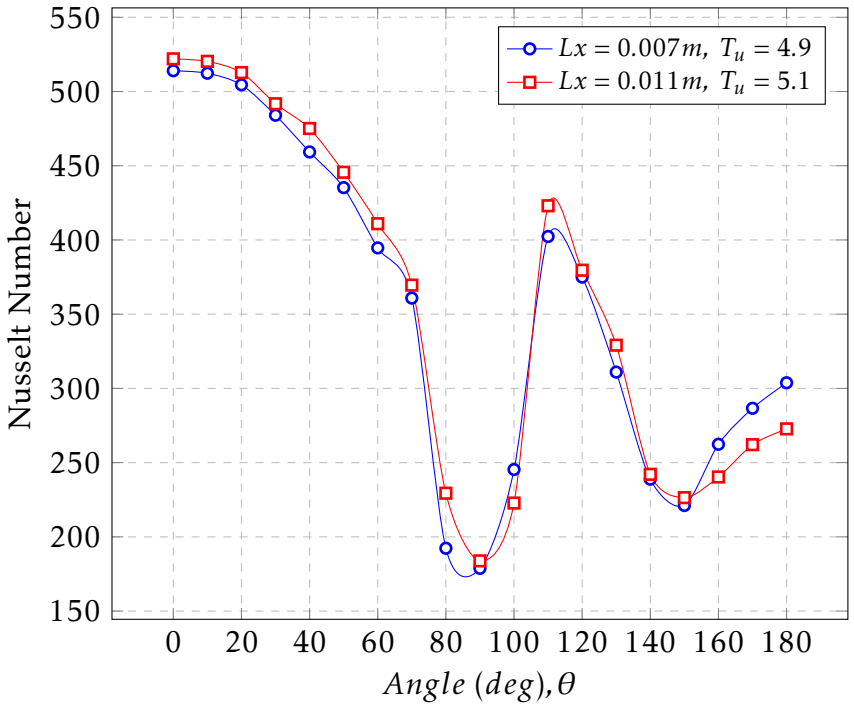

Figure 4.15: Distributions of the local Nu number along the perimeter of the circular cylinder for the two different turbulent scales at $Re = 7.5x10^4$.

4.3 Roughness Effect

4.3.1 Total heat transfer

The total heat transfer coefficient at different roughness heights are shown in Figure 4.16. As the roughness increased the overall Nusselt number increased. As the Reynolds number increased the impact of surface roughness also increased resulting in enhanced heat transfer. These results are in agreement with those of **Achenbach** [38, 121] and **Zukauskas** [73] who showed similar increases. They attributed the increase in heat transfer to changes in the boundary layer around cylinder these will become apparent in the local heat transfer measurements. Table 4.3, illustrates the increase of the total heat transfer because of the surface roughness compared with the smooth cylinder.

4.3.2 Local heat transfer

In Figures 4.17 - 4.19 the local Nusselt number around the cylinder is shown for different Re numbers for each of the three roughnesses tested.

The results of the smallest roughness ($\epsilon/D = 113xl0^{-5}$) for five flow rates shown in Figure 2.16. The results are similar to those observed for a smooth cylinder. At low Reynolds number, the max Nu_θ is seem at the forward separation point ($\theta = 0^o$), Nu_θ then decreased achieving a minimum at an angle of $\theta = 90^o$. As the angle increased so did Nu_θ. At higher values of Re, the existence of a recirculation becomes apparent from $\theta = 80^o$ to $\theta = 140^o$.

Shown in Figure 4.18 is the local heat Nusselt number for a roughness of $\epsilon/D = 325x10^{-5}$. At the lowest Reynolds numbers the local heat transfer is again as observed for smooth cylinders, a peak value of Nu_θ was observed at 0^o which then decreased reaching a minimum at an angle of 100^o after which the heat transfer increased. However at a Reynolds number of 48500 the heat transfer profiles changes. The Nu_θ at the forward separation point remains relatively constant and then there is a rapid rise in Nu_θ starting on the front face of the cylinder. The resulting peak in Nu_θ encompasses the range 60^o to 110^o (this range was larger for higher Re). Similar results were observed for the largest roughness tested ($\epsilon/D = 7.25 \times 10^{-3}$) as shown in Figure 4.19. the main difference was that peak in heat transfer from 60^o to 110^o was observed at lower values of Re. The largest values of Nu_θ were recorded, ≈ 800, for $\epsilon/D = 7.25 \times 10^{-3}$ at $Re \approx 87000$.

Figures 4.20 and 4.21, represent the local Nu_θ number at a consistent Reynolds number for different roughness levels. At $Re = 3.5xI0^4$, Figure 4.20, the sub-critical (laminar) flow is still covered the entire cylinders at smooth and two lower roughnesses. However, the highest roughness just induces critical flow conditions. At highest roughness leads to move separation point downstream at about $\theta = 140^o$. At $Re = 7.5x10^4$, Figure 4.21, the laminar-turbulent transition

occurs on the front part of the cylinder ($\theta < 90^o$) for each of the three roughened cylinders. The transition point takes place at about $\theta = 40^o$ and $\theta = 0^o$ for $\epsilon/D = 1.13 \times 10^{-3}$ and $\epsilon/D = 7.25 \times 10^{-3}$ respectively. The turbulent flow regime is found for the cylinder covered with the highest roughnesses where turbulent flow covers the entire cylinder. At smallest roughness, the separation bubble phenomenon (reattach) occur as well which help to substantial increase of the heat- transfer coefficient.

From these Figures (4.20 and 4.21) it can be seen that the critical Re number (Re_{cr}), declines with increasing roughness element. This is conceivable, with decreasing Re number causes the increasing thickness of boundary layer which results in submerge the roughness gradually in it.

At the Re number lower than critical Reynolds number (Re_{cr}), the laminar boundary layer develops from the Fsp ($\theta = 0^o$) then it separates at angle about ($\theta = 100^o$). But at the Re number higher than critical Reynolds number (Re_{cr}), the surface roughness help to aggravates disturbance near the cylinder surface and induces the transition to the turbulent boundary layer, and thus increase local heat transfer with θ. Due to boundary layer transition, a sudden difference in Nu_θ number happens at a specific angle from the Fsp ($\theta = 0^o$) which relies on a surface roughness and Re values. Table (4.4) appears the angular position of transition point (θ) as a function of roughness height and Reynolds number. It is quite clear that the transition point moves upstream, towards the front stagnation point (Fsp) with increasing Reynolds number. Additionally, at a fixed angular position on the front half of the cylinder, the boundary layer transits from laminar to turbulent flow at lower Reynolds numbers with increasing relative roughness (ϵ/D). In the other words, the angle of transition decrease with increase Reynolds numbers or relative roughness ($\theta_t \ \alpha \ \frac{1}{Re \ \epsilon/D}$).

Appropriate surface roughness provides considerable heat-transfer improvement. Figure 4.22 shows the comparison of local heat-transfer for highest roughness ($\epsilon/D = 7.25x10^{-3}$) and smooth cylinders. it is obvious that due to movement of the transition point toward upstream in high Re number, the heat transfer increases over the front part of the cylinder, and thus the contribution of the heat transferred from the front half of the cylinder is more than in the rear position of the rough cylinder. Generally, in average the total heat transfer increases about 11% in the fine surface roughness ($\epsilon/D = 1.13x10^{-3}$), and about 46% in the high surface roughness ($\epsilon/D = 7.25x10^{-3}$).

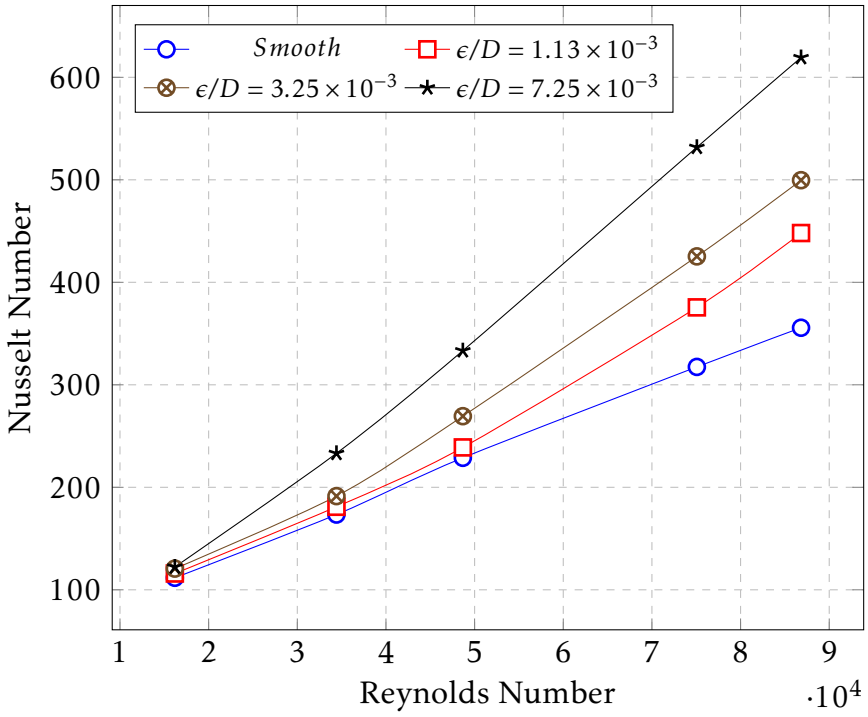

Figure 4.16: Effect of surface roughness on total heat-transfer coefficient.

Table 4.3: The increasing of the total heat transfer due to the roughness of the surface, compared with the smooth cylinder.

Present Work	Smooth	$\epsilon/D =$ (1.13×10^{-3})	Deviation (%)	$\epsilon/D =$ (3.25×10^{-3})	Deviation (%)	$\epsilon/D =$ (7.25×10^{-3})	Deviation (%)
$1.6x10^4$	111	116	**3.7**	120	**8**	122	**9.4**
$3.5x10^4$	173	181.6	**4.3**	191	**10.4**	233	**34.5**
$4.9x10^4$	229	239	**4.4**	269	**17.8**	333	**45.7**
$7.5x10^4$	317	376	**18.3**	425	**34**	531	**67.5**
$8.7x10^4$	356	448	**26**	499	**40.5**	619	**74.1**
Mean Deviation	/	**11.4 %**		**22.1 %**		**46.3 %**	

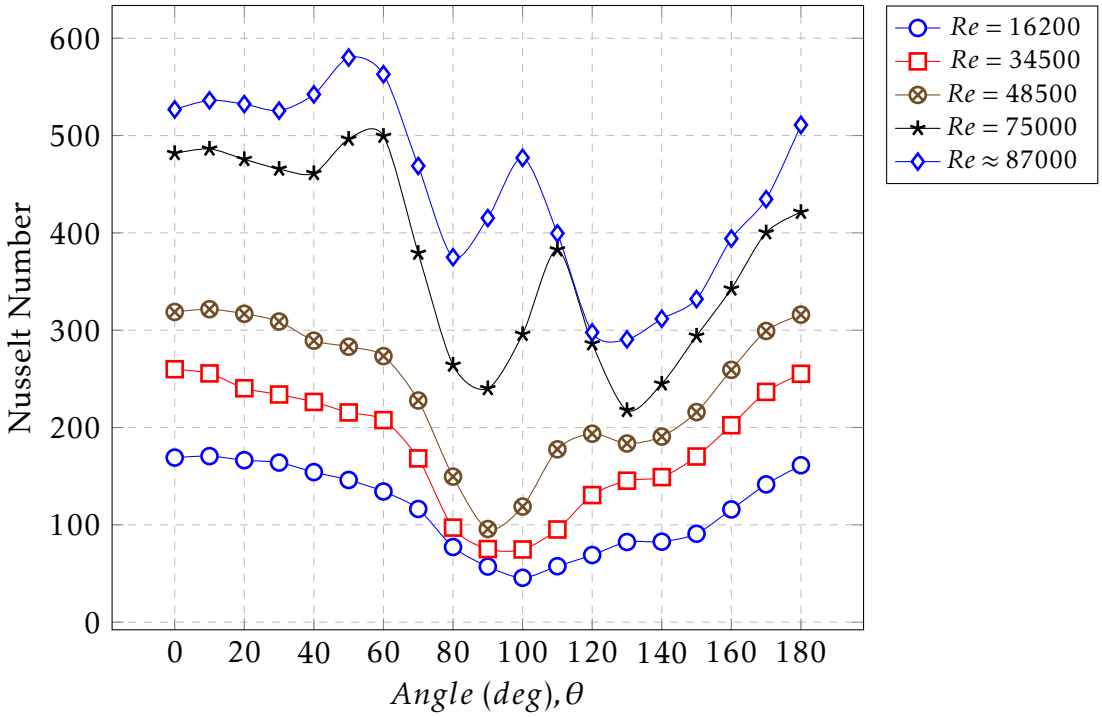

Figure 4.17: Variation of local Nusselt number at $\epsilon/D = 1.13 \times 10^{-3}$ and variable Re numbers.

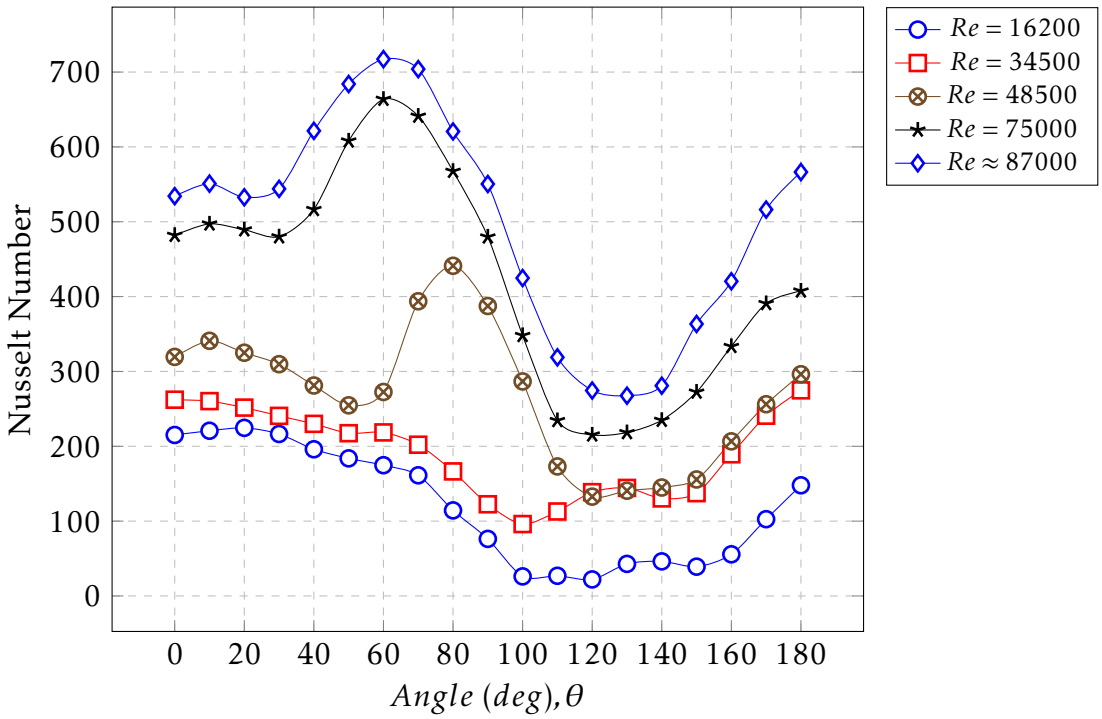

Figure 4.18: Variation of local Nusselt number at $\epsilon/D = 3.25 \times 10^{-3}$ and variable Re numbers.

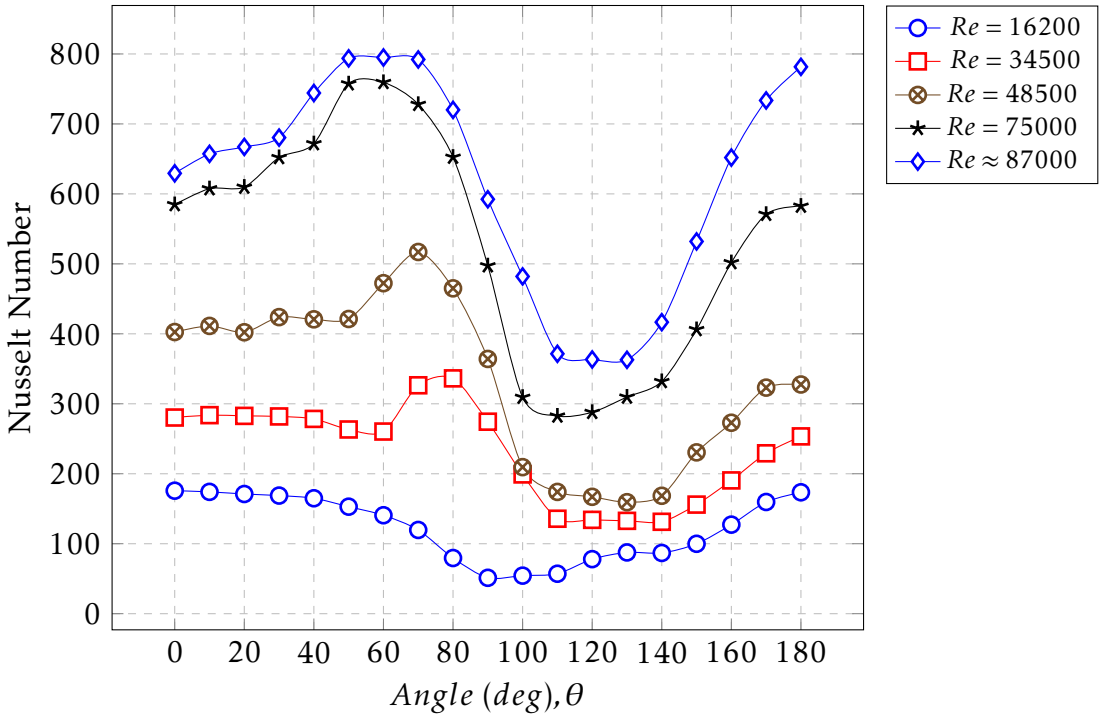

Figure 4.19: Variation of local Nusselt number at $\epsilon/D = 7.25 \times 10^{-3}$ and variable Re numbers.

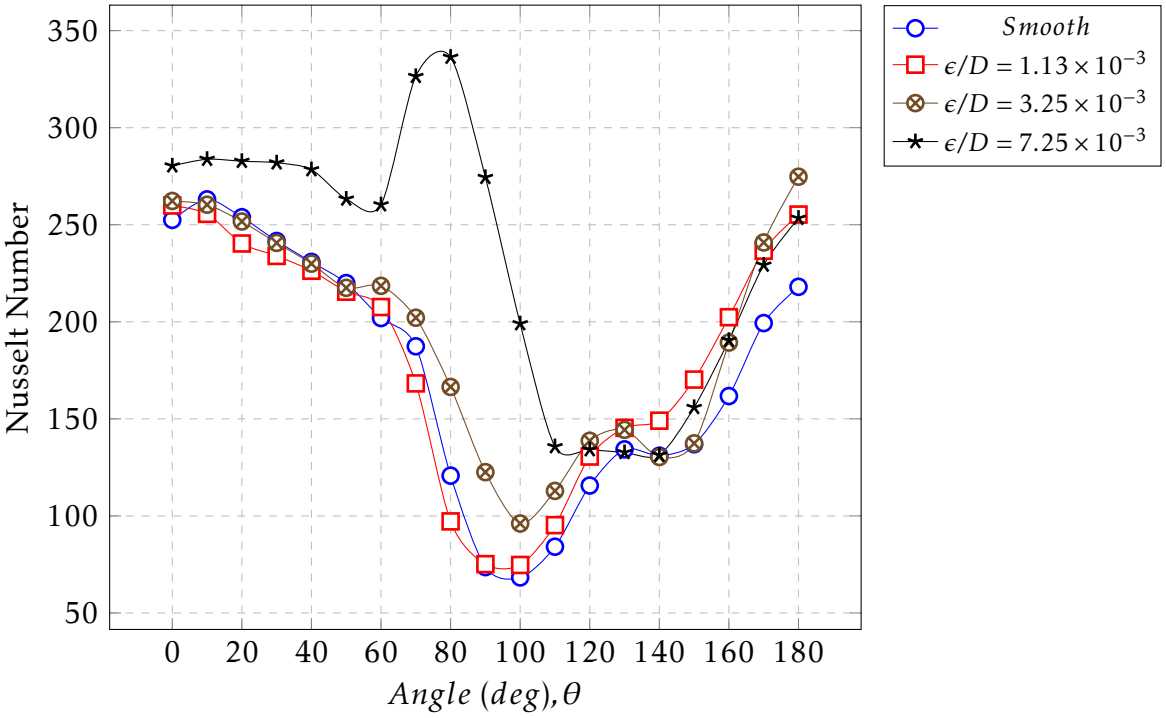

Figure 4.20: Local heat-transfer coefficient at $Re = 3.5x10^4$ and variable roughness levels.

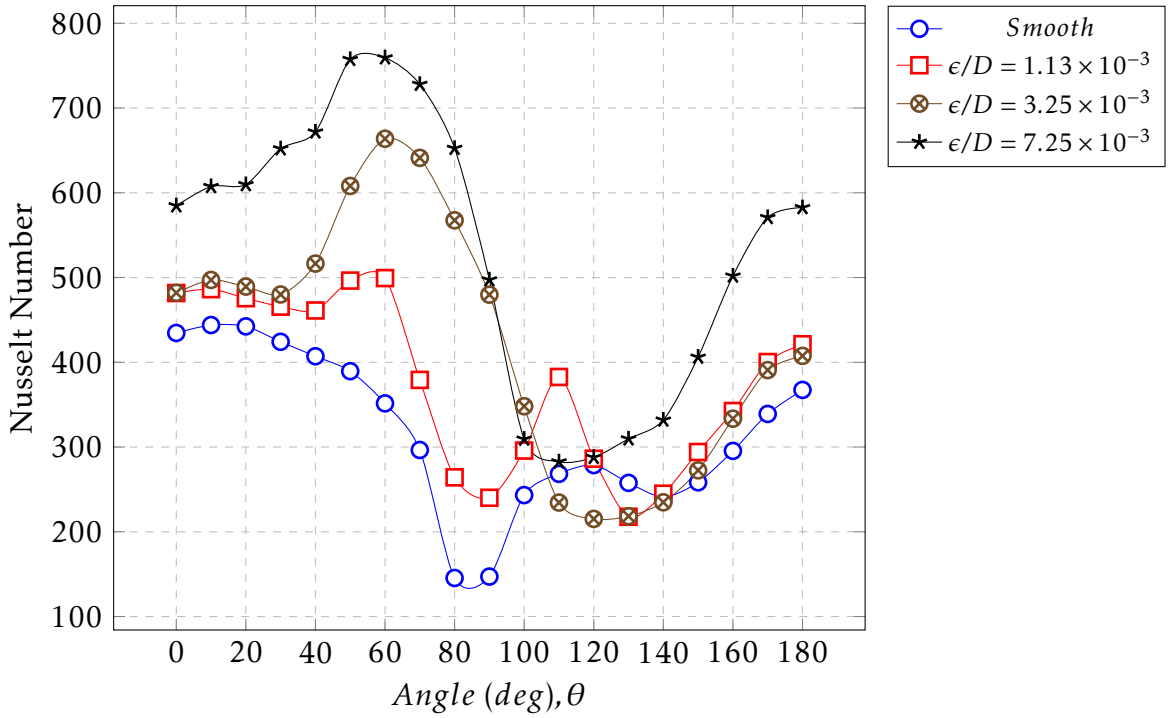

Figure 4.21: Local heat-transfer coefficient at $Re = 7.5x10^4$ and variable roughness levels.

Table 4.4: An angular position of transition point as a function of Re number and roughness parameter ϵ/D.

Re number	$\epsilon/D = 725x10^{-5}$	$\epsilon/D = 325x10^{-5}$	$\epsilon/D = 113x10^{-5}$
$1.6x10^4$	-	-	-
$3.5x10^4$	60^o	-	-
$4.9x10^4$	30^o	50^o	-
$7.5x10^4$	0^o	30^o	40^o
$8.7x10^4$	0^o	20^o	30^o

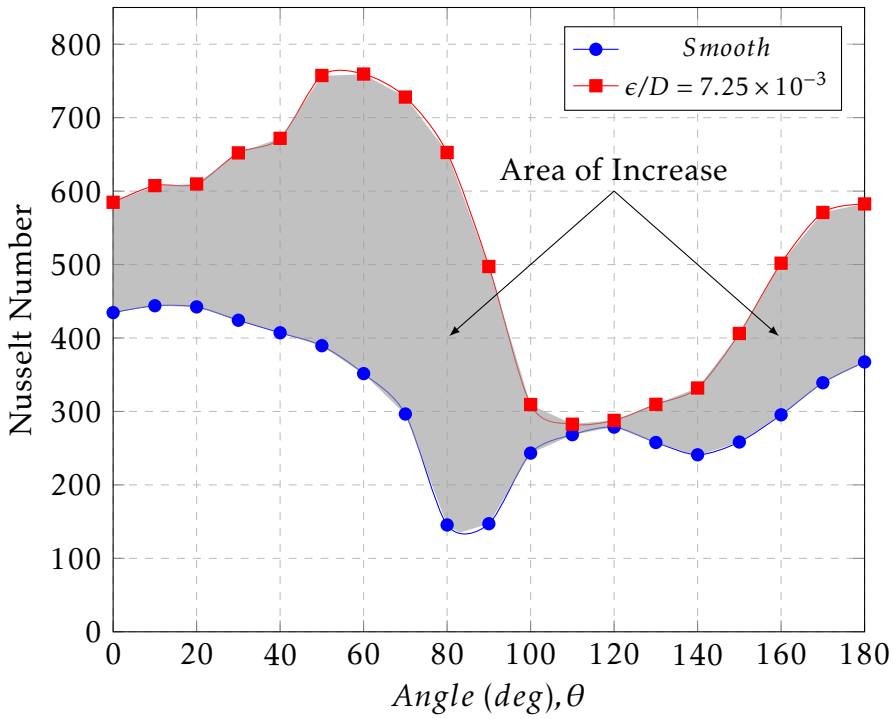

Figure 4.22: Comparison of the local variation of Nu number around a smooth and highest roughness cylinder ($\epsilon/D = 725x10^{-5}$) at Re number $7.5x10^4$.

4.4 Combined effects of FST and roughness

4.4.1 Total heat transfer

The Figure 4.23 has been separated to demonstrate the slope of the heat transfer curves for the four cylinders at the different levels of roughness and FST. It can be shown that the slope of a simple relationship between Re number and Nu number ($Nu = aRe^m$) is changing depending on the values of surface roughness and turbulence intensity. where the slope is affected by increasing FST and roughnesses, in other words, these effects combine. At relative roughness $\epsilon/D = 1.13x10^{-3}$, this changing occurs at Re number $4.9x10^4$, while it happens with low FST at higher Re number ($7.5x10^4$). At higher relative roughness $\epsilon/D = 7.25x10^{-3}$, due to combining effect of roughness and FST, the critical Reynolds number move to less value, i.e. the critical Reynolds number is reached faster, these will become clearer in measurements of local heat transfer.

The Nu_θ number gradually increases since a laminar to a turbulent boundary layer transition point moves upstream when reaching the critical Reynolds number (Re_{cr}). At this stage, the slope of relationship $Nu = aRe^m$ stepwise changes. This can be clarified by expanding of the laminar boundary layer in the Reynolds number before the critical Reynolds number. Hence an extensive part of the surface is wrapped by laminar boundary layers which represent a significant resistance to heat transfer. Beyond the critical Reynolds number, the local Nu_θ number rapidly increases because of the transition of boundary layer close to the cylinder surface to turbulent layer. Furthermore, the value of critical Reynolds number decrease according to surface roughness and FST values in contrast to the results for the smooth cylinder at low FST ($Re_c \approx 1x10^5$).

The Figure 4.23 also indicate that at Re number $4.9x10^4$ (sub-critical regime) with the small rough element ($\epsilon/D = 1.13x10^{-3}$), an increase of turbulence to 10% leads to a 20% increase of total Nu number. With further expansion of Reynolds number($7.5x10^4$) , the effect of turbulence on the total Nu number grows to 27%. In the highest surface roughness ($\epsilon/D = 7.25x10^{-3}$), an increase of turbulence intensity from 2.2 to 10% gives a 16% increase in the mean Nu number at Re= $4.9x10^4$ and a large increase in the total Nu number occurs about 12% with a further increase of Re to ($7.5x10^4$).

Combining effect of roughness and turbulence intensity together lead to multiplying the heat transfer compared with smooth one at ($T_u = 2.2$, without grid), an increase of turbulence intensity from 2.2 to 9.7% gives a 45% and 80% increase in the mean heat transfer at Re= $7.5x10^4$, In the surface roughness ($\epsilon/D = 1.13x10^{-3}$), and ($\epsilon/D = 7.25x10^{-3}$), respectively.

4.4.2 Local heat transfer

The combined influence of these two factors (FST and surface roughness) on local heat transfer are shown in Figures (4.24-4.26). As shown in these Figures, the surface roughness and FST exert a certain effect on the flow field around the cylinder, in the low Reynolds number, the turbulence in the main flow and surface roughness have no clear influence on the heat transfer coefficient, while in the high Reynolds number range, the variation of Nu_θ number depends on both of these two factors. In general, when the surface roughness and/or FST increase the Re number which the critical flow regime is formed declines. The existence these two factors augments the heat transfer in critical flow range. Additionally, these Figures indicate that the surface roughness has the higher impact than FST on heat transfer i.e. the most dominance influence.

Figure 4.25 shows the impact of the FST on local heat transfer behaviour with a moderate relative roughness ($\epsilon/D = 325x10^{-5}$) for different flow rate. These curves help to determine the predominant fraction of FST. It can be seen that the maximum influence of the turbulence of free-stream at Re Number $3.5x10^4$. In this range of Re number, the additive action of the FST and the surface roughness produced the velocity fluctuations in the boundary layer, with a further increment of Reynolds number and after the vanishing of reattaching region ($\theta = 100^o - 150^o$), the impact of a surface roughness and low thickness of the boundary layer produce greater increase of the heat transfer. Moreover, in the high flow rates, the heat transfer coefficient augmentation relative to the low turbulence intensity (no grid, $Tu = 2.2$) is significant in the laminar boundary layer ($\theta = 0^o - 60^o$), caused by the upgrade of velocity fluctuations resulting from increasing turbulence intensity. At the front stagnation point, The heat transfer demonstrates a general tendency to increment with turbulence intensity, this particular behaviour contingent upon the Re number, it is not clear in lower Re number. It is also clear that the impact of turbulence intensity is confined and is most grounded in the front half of the cylinder, its impacts becoming noticeably less at higher angular positions ($\theta = 70^o - 100^o$). No precise impact of turbulence can be seen in the rear half of the cylinder.

At a fine relative roughness ($\epsilon/D = 1.13 \times 10^{-3}$), Figure 4.24, the effect of a turbulence intensity on local heat transfer coefficient is similar to that corresponding to a moderate roughness ($\epsilon/D = 3.25x10^{-3}$), Figure 4.25, but the trend of the curves are slightly different. In particular, the maximum influence of the turbulence intensity occurs at higher Re number, $4.9x10^4$ compare with $3.5x10^4$ at a moderate relative roughness ($\epsilon/D = 3.25 \times 10^{-3}$). It can be seen that the increase of heat transfer is, in this circumstance, governed by the level of turbulence intensity only.

At a high relative roughness ($\epsilon/D = 7.25 \times 10^{-3}$), Figure 4.26, no clear augmentation of the heat transfer was observed with the increase of the turbulence intensity in reattaching region ($\theta = 100^o - 150^o$). By analogy, the effect of relative

roughness which is made the boundary layer thicker by adding the streams separating has made this region has the lowest value of heat transfer. In the other hand, still, the direct effect of turbulence intensity on the heat transfer coefficient augmentation in the front part of the cylinder ($\theta = 0^o - 60^o$) is considerable. Figure 4.27 below shows the combined effect of free stream turbulence and the roughness on the enhancement of heat transfer at Reynolds number $7.5x10^4$, resulting from increase FST to ($Tu = 9.7\%$), as indicated in Region I, while Region II represents the enhancement of heat transfer because of the roughness($\epsilon/D = 7.25x10^{-3}$).

In general, In the sub-critical flow regime, the augmentation of the relative roughness or of the FST (turbulence level) can give just a moderate increase of the heat transfer. Whilst, in the critical flow regime, a higher relative roughness helps to increase heat transfer coefficient and to an earlier laminar to turbulent transition in the boundary layer i.e a prior onset of the critical flow regime. A similar tendency was seen with increasing of the turbulence intensity.

It is pertinent to mention that the local Nu_θ number differs impressively around the circumference, many applications frequently require average heat transfer over different zones. The mean heat transfer for the front part (the transitional region) which is covered by the laminar boundary layer, and the rear part (the turbulent boundary layer) are shown in Figures (4.28 and 4.29), respectively.

As shown in these Figures and as expected, the heat transfer is high in the rear half of the rough cylinder compare with the smooth one, because of the air dynamic behaviour in this region still more complex and effect which incorporates the turbulent boundary layer and the separation point.

On the other hand, the increase of the turbulence intensity leads to the heat transfer increasing in the front part for both smooth and rough cylinders, with an increase of turbulence intensity up to 10% the heat transfer averaged increasing by about 19% and 13% for smooth and rough cylinders, respectively. While in the rear part the heat transfer is autonomous of the turbulence level, the vortex flow effect becomes more predominance.

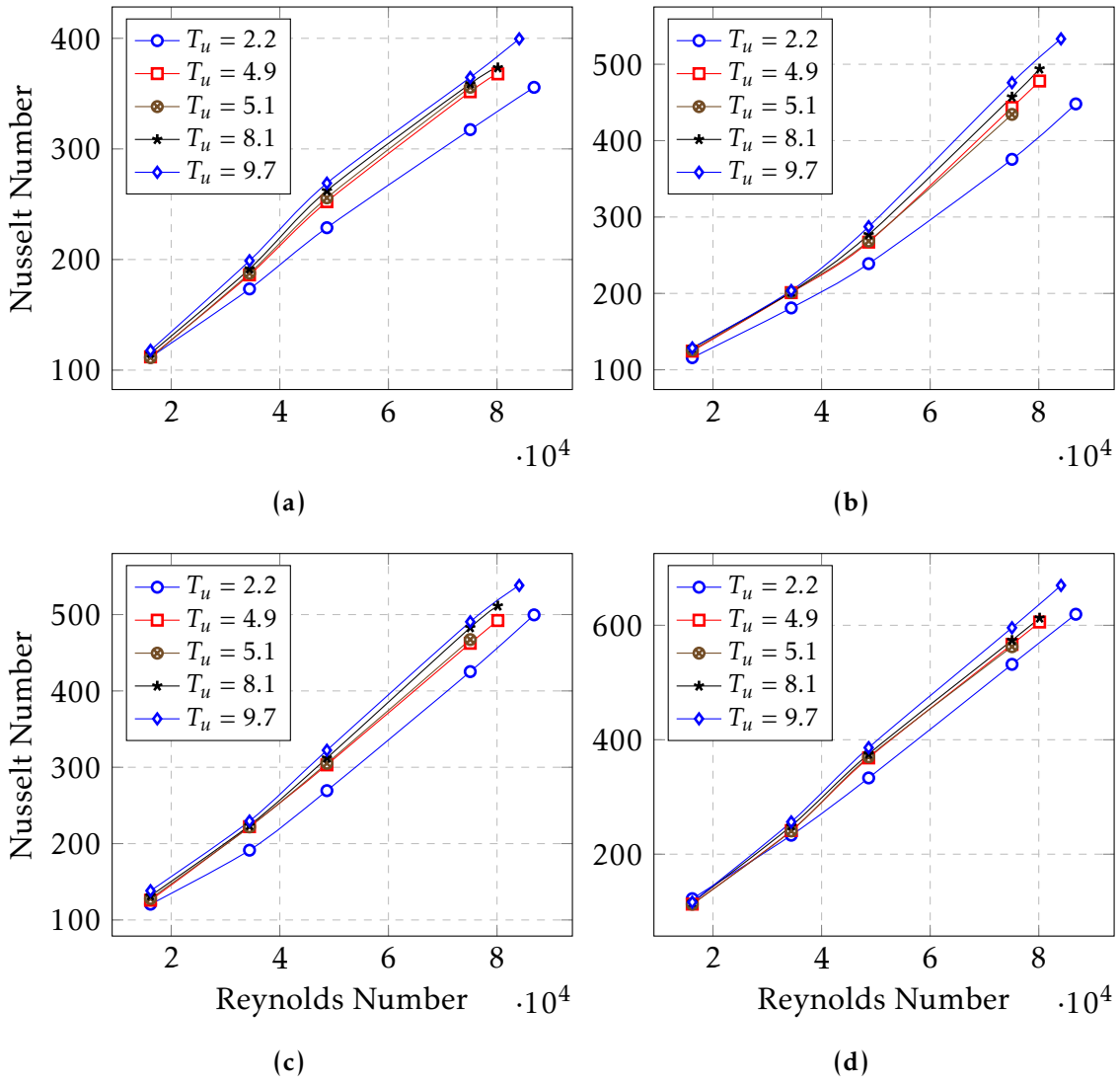

Figure 4.23: Effect of turbulence level on total heat-transfer coefficient for different surface roughness, (a) Smooth cylinder, (b) $\epsilon/D = 1.13 \times 10^{-3}$, (c) $\epsilon/D = 3.25 \times 10^{-3}$, (d) $\epsilon/D = 7.25 \times 10^{-3}$

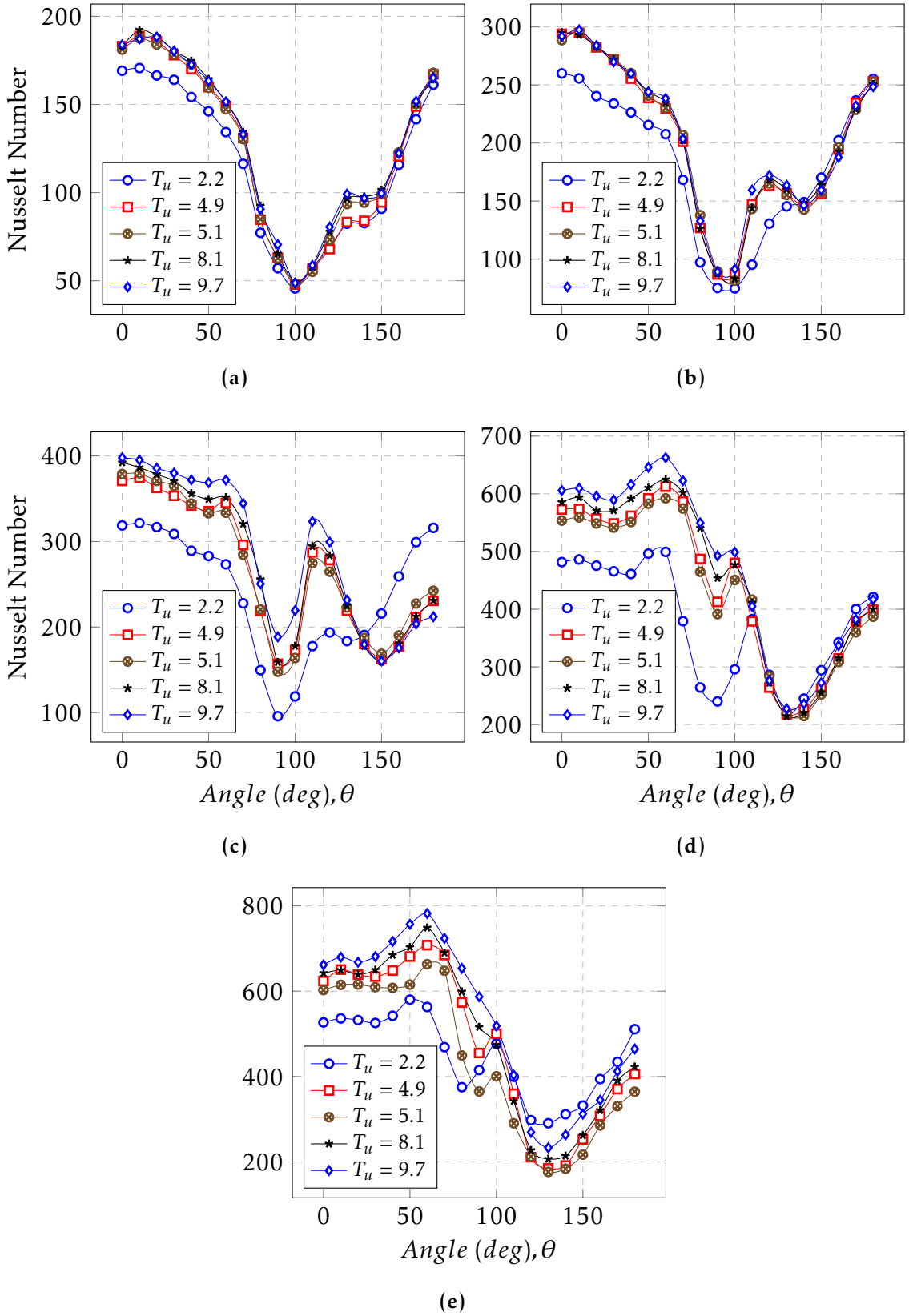

Figure 4.24: Effect of turbulence level on local heat-transfer coefficient at $\epsilon/D = 1.13 \times 10^{-3}$ for different flow rate, (a) $Re = 16200$, (b) $Re = 34500$, (c) $Re = 48500$, (d) $Re = 75000$, (e) $Re \approx 87000$

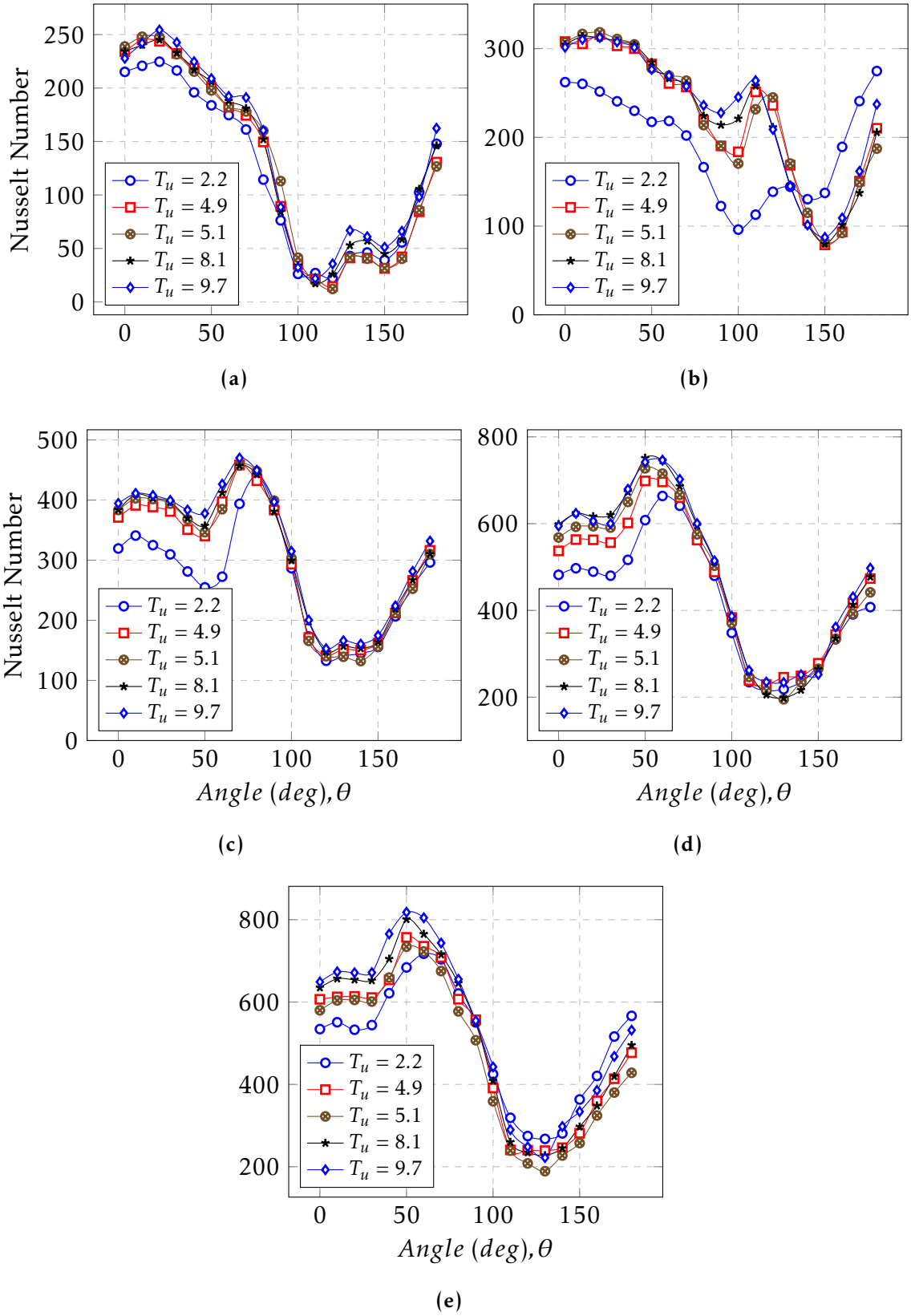

Figure 4.25: Effect of turbulence level on local heat-transfer coefficient at $\epsilon/D = 3.25 \times 10^{-3}$ for different flow rate, (a) $Re = 16200$, (b) $Re = 34500$, (c) $Re = 48500$, (d) $Re = 75000$, (e) $Re \approx 87000$

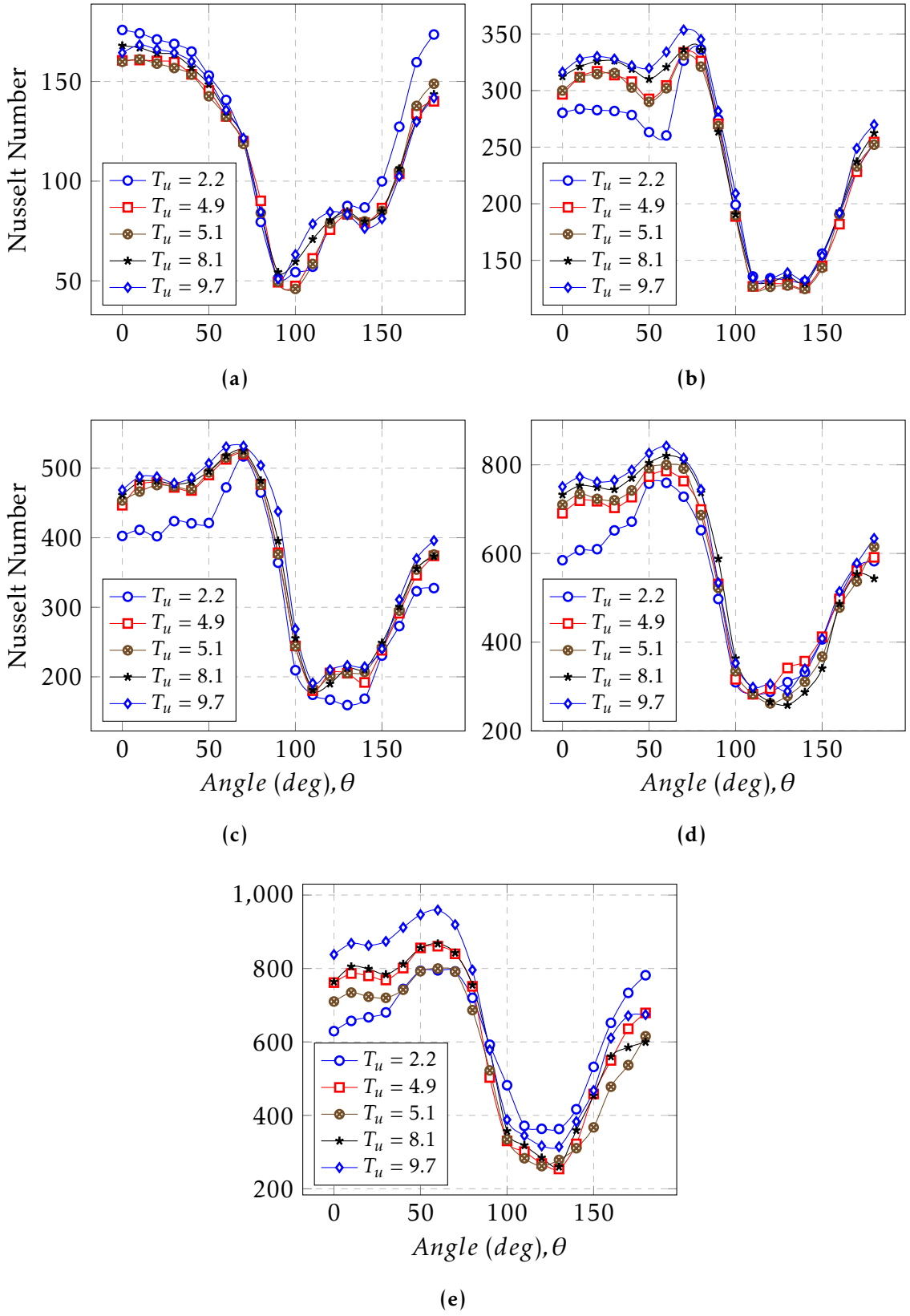

Figure 4.26: Effect of turbulence level on local heat-transfer coefficient at $\epsilon/D = 7.25 \times 10^{-3}$ for different flow rate, (a) $Re = 16200$, (b) $Re = 34500$, (c) $Re = 48500$, (d) $Re = 75000$, (e) $Re \approx 87000$

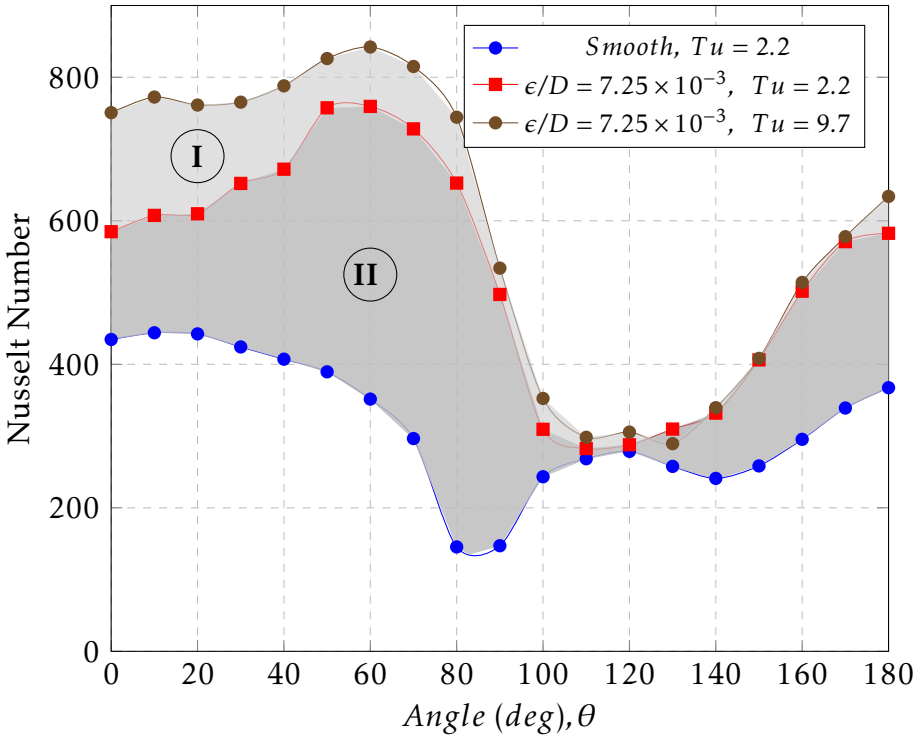

Figure 4.27: The combined effect of FST and roughness on the enhancement of heat transfer at Re number $7.5x10^4$. I- effect of FST ($Tu = 9.7\%$), II- effect of roughness ($\epsilon/D = 725x10^{-5}$)

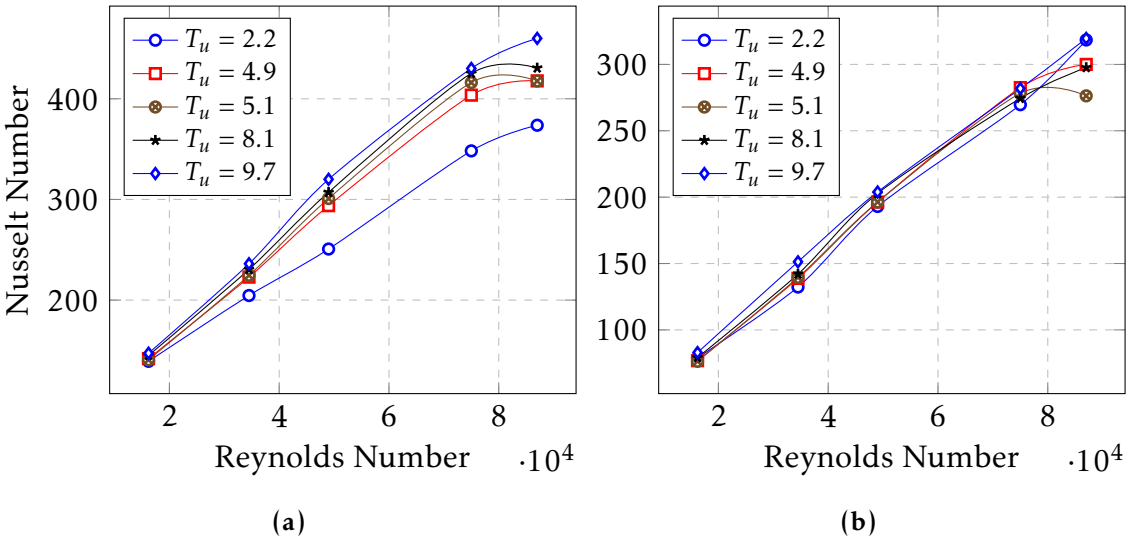

Figure 4.28: Average heat transfer at the front and rear parts of the smooth cylinder (a) front half , (b) rear half

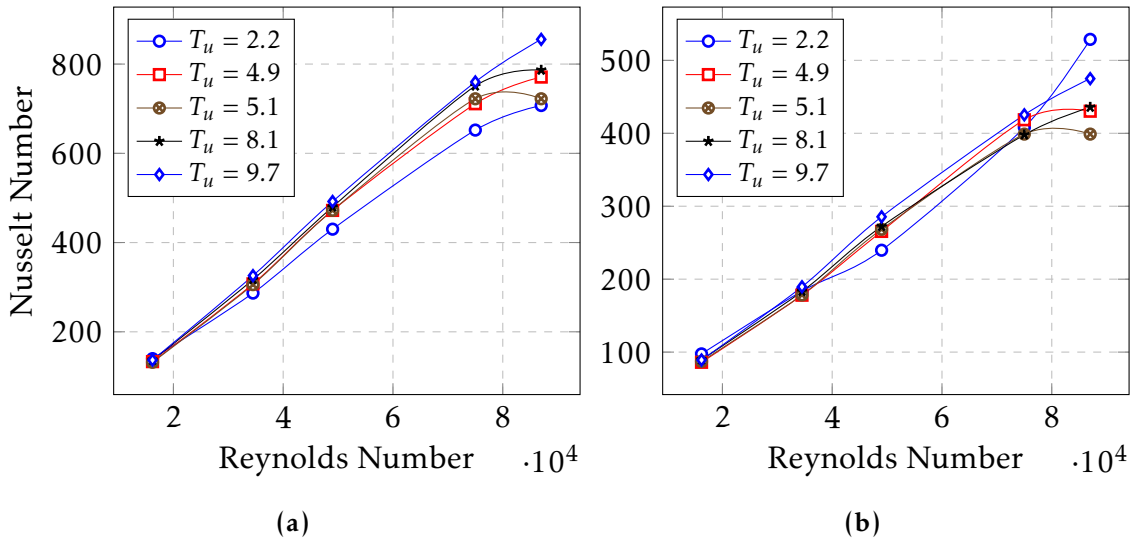

Figure 4.29: Average heat transfer at the front and rear parts of the rough cylinder (a) front half , (b) rear half

4.5 Flow field in the wake region

For a range of mass flow rates, the frequencies of vortex street (shedding) are demonstrated in Figures 4.30 and 4.31 for blockage ratios 20% and 40%, respectively. As shown, only one single peak frequency was recognised for each flow rate. These figures clearly indicated the increase in mass flow rate (Re. number) with increasing the frequency of vortex shedding. Moreover, the value of vortex shedding frequency decreases with blockage ratio.

Figure 4.32, shows the effect of the blockage ratio (β) on the Strauhal number which is helped to determine the dominating wake region frequency by defining the ratio of vortex shedding frequency and cylinder diameter to mainstream velocity ($St = f.D/U$). As shown the relationship between Strouhal numbers and Re numbers at blockage ratio $\beta = 20\%$ is linear and the St number shows a slight decrease with Re number increase (about 0.2 for all Re range). These results are good agreement with the previous investigations [17, 122]. It is also shown that at $\beta = 40\%$, the St number increases with Re number growing, also rises with increasing β (and vice versa), that occurs because the velocity at the separation point increases compared to unconfined flow conditions [17].

Figure 4.33 shows how the frequency of vortex shedding (St numbers) is affected by different Tu levels at constant Re number. The velocity fluctuations were collected at an averaged Re about $5x10^4$. The turbulence intensity levels are varied between $\approx 2.2\%$ and $\approx 9\%$.There are clear indications that, the increase in the FST level has comparable consequences for the St number as an increment in Re where the Strouhal number is increased with growing the free stream turbulence intensity. This augment agrees well with the observations by **Norberg** [123] and **Khabbouchi** [53], who found that the Strouhal number increases by 20% from a turbulence intensity of 0.3% to 6%.

Shown in Figure 4.34 are the RMS coefficients and turbulence intensity level of the fluctuating velocity in the near-wake region for blockage ratios 20% and 40%. It is quite clear that they are directly dependent on the Reynolds number, while the blockage ratio has no clear influence.

The effect of turbulence intensity and blockage ratio are not only on the separation boundary layer on the cylinder surface but also in its interaction with the separated shear layers and the wake region. Mostly, the zone beyond the cylinder consists firstly from separated boundary layers then vortices which in turn rotate in the same positioning or are orderly shed from the surface and therefore configure vortex street phenomenon [2]. The free stream turbulence intensity has two important roles: firstly, it augments the level of turbulence inside the separating shear layer and therefore it helps to accelerate the formation and the breakdown of the vortices. Secondly, the FST decreases the forming length which leads to prevent the separating layer from developing near the wake region.

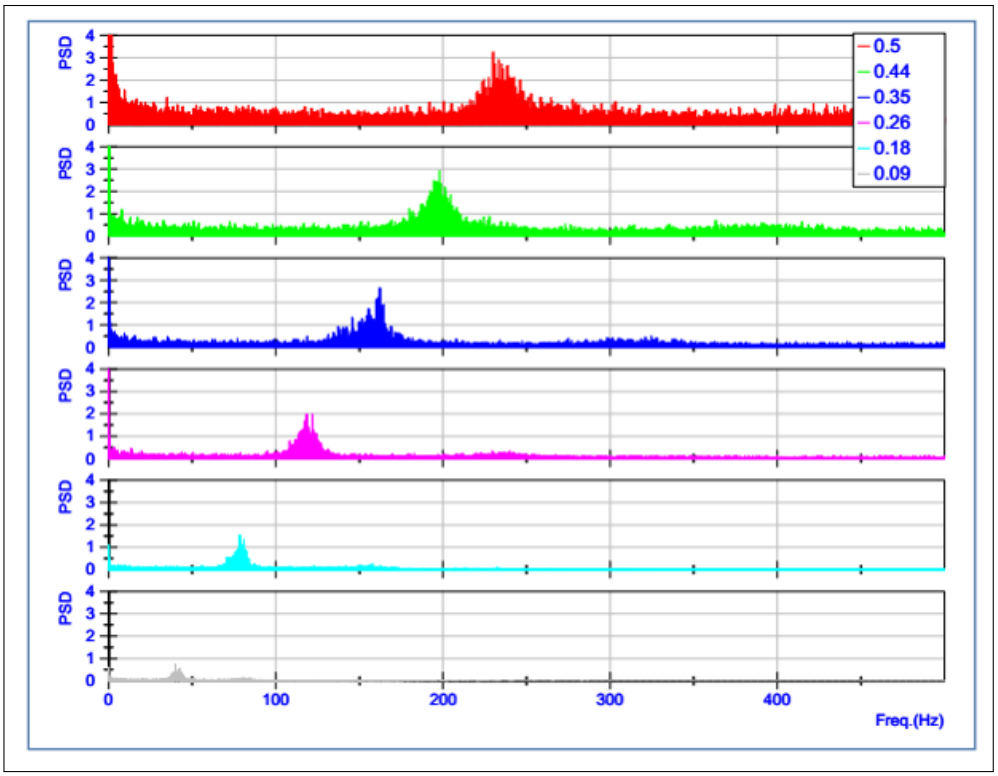

Figure 4.30: Power Spectral Densities of velocity fluctuations in wake region at the different mass flow rate (kg/s) with blockage ratio $\beta = 20\%$

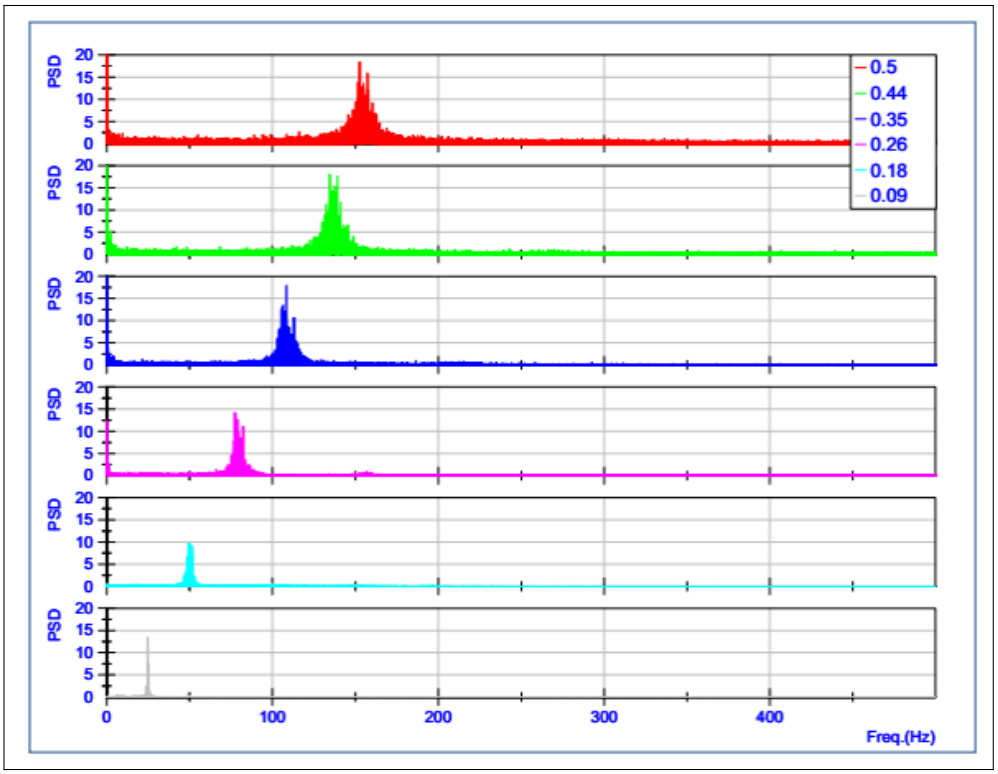

Figure 4.31: Power Spectral Densities of velocity fluctuations in wake region at the different mass flow rate (kg/s) with blockage ratio $\beta = 40\%$

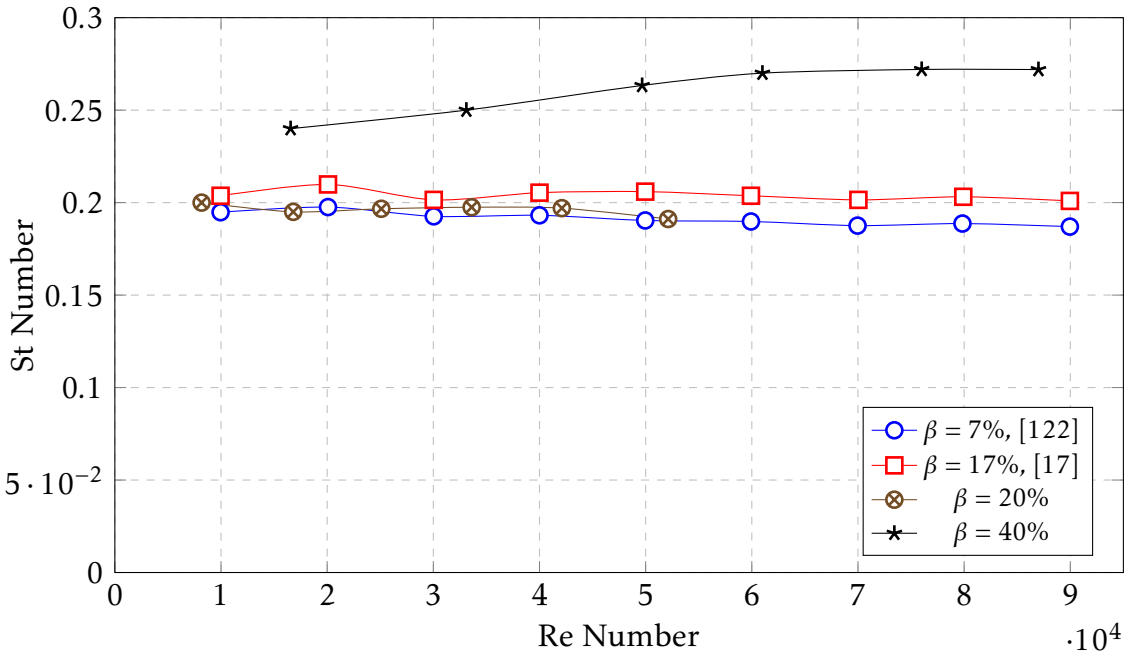

Figure 4.32: The relationship between the Strouhal number and the Reynolds number for different blockage ratio

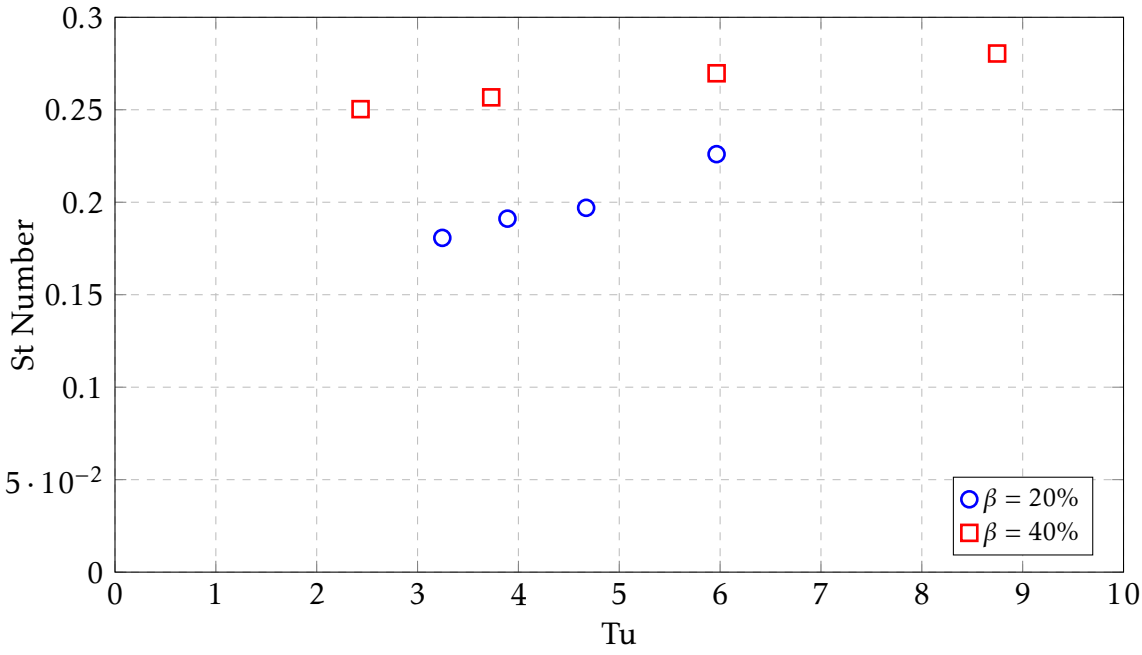

Figure 4.33: The effect of Tu level on the Strouhal number for different blockage ratio.

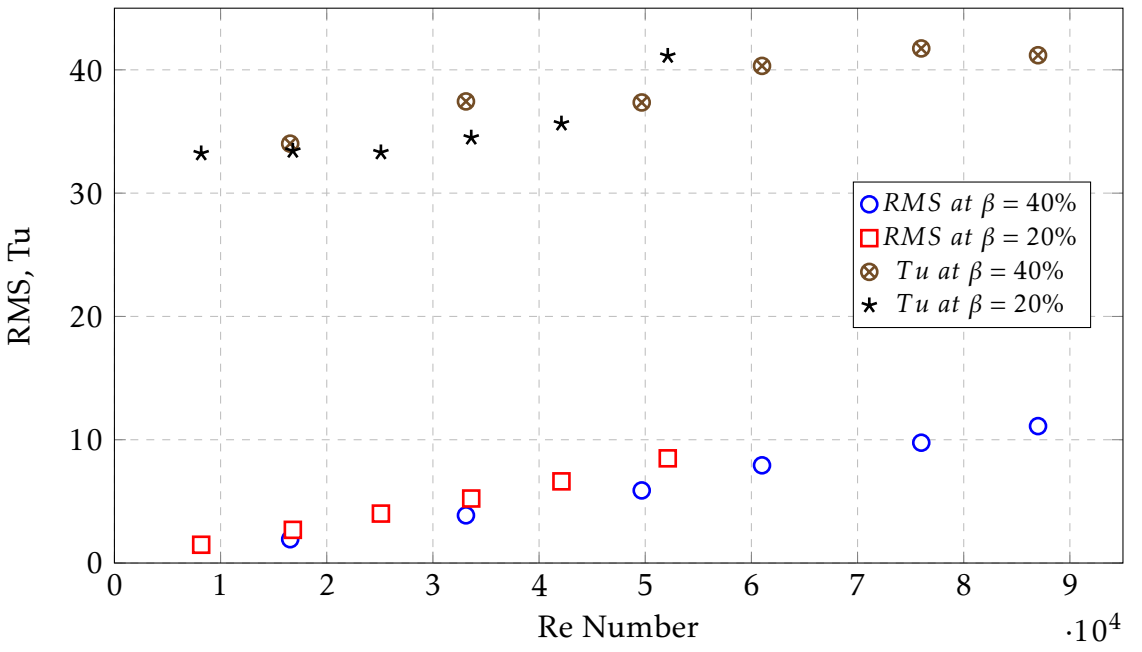

Figure 4.34: Variation of RMS and Tu of velocity in wake region with Reynolds number

CHAPTER 5

Infrared Thermography

5.1 Introduction

With developing in technology and science, the measurement tools and their quality are excessively increasing, principally in some fields, like scientific research, surveillance systems, medical domains, aerospace and so on. One of the best ways for obtaining the temperature distribution map of the surfaces is to use infrared thermo-vision techniques which consist of a source of heating, infrared camera, and PC. The thermography method is a non-intrusive technology which does not request direct contact with tested surface [124].

Among all the non-destructive methods, the IR technique plays an interesting role. In general, thermal Infrared imagery participates several optical techniques like ultraviolet (UV) and visible (VIS) techniques and they are widely used in the study many of the engineering applications especially in manufacturing processes. Furthermore, using the IR imaging to study temperature distribution of cylinders in cross-flow is not commonly adopted [125]. Therefore, IR images used with the IR transparent materials could help to better understand the heat transfer process from the rough cylindrical surface. This technique is very helpful to get detailed data from the rough cylinders in cross flow.

5.1.1 Background

The advantages of IR cameras are that they are a non-contact technique with fast response [124]. Recently, thermal cameras operating in the far-infrared range have evolved to powerful tools to investigate heat flux as well as to measure the surface temperature field over complex forms [126, 127]. Thermal IR technology depends on measuring the emitted thermal radiation from a surface and then converting these measurements to visual images by means the post-processed with a numerical model [128, 129]. The radiant temperature of a material is related to the surface emissivity [126]. On the other hand, it is hard to determine the relation between surfaces temperature and its roughness. Therefore, it is very interesting to study the effect of surface roughness on the temperature maps of a material surface.

5.1.1.1 Theory

All bodies, with a temperature more than absolute zero, emit thermal energy as an electromagnetic radiation over a broad range of wavelengths from the ultraviolet band (UV) up to the infrared band(IR) [130]. The electro- magnetic spectrum is divided into a number of wavelength bands as seen in Figure 5.1 ; The infrared region, the wavelength between 750 nm to 1000 μm [131] is in turn sub-divided into four arbitrarily chosen zones [127] :

1. near infrared ($0.75 - 3\mu m$).

2. middle infrared ($3-6\mu m$).
3. far infrared ($6-15\mu m$).
4. extreme infrared ($15-1000\mu m$).

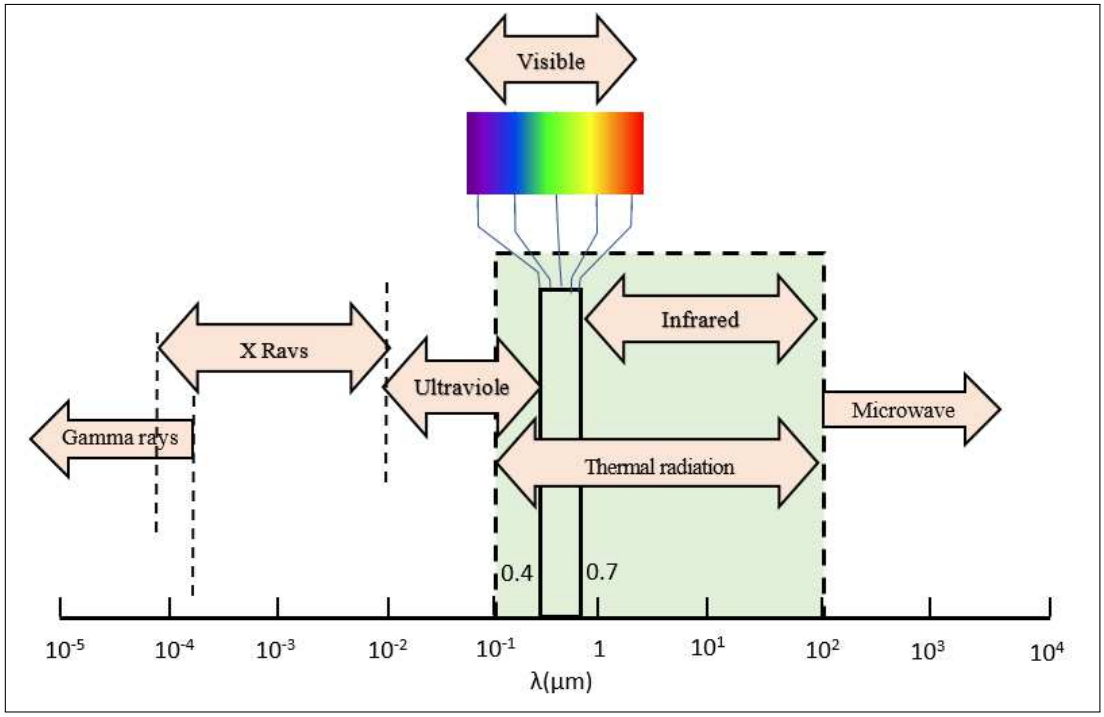

Figure 5.1: Spectrum of electromagnetic radiation [35]

Emissivity: All surfaces have a different emissivity which impacts the thermal radiation emitted from a surface. It is a surface unit-less property and defined as the relationship between the radiant temperature and the surface temperature. The emissivity has the value between 0 (completely not-emitting) and 1 (completely emitting and called a blackbody) [130]. Practically, the emissivity is affected by many factors, such as temperature, surface roughness, viewing angle, moisture content, etc. However, the most influential factors are the surface temperature and surface roughness [132, 133].

Radiation: Thermal emission is based around the assumption of a perfect emitter in a thermal equilibrium state (at a constant temperature). The spectral intensity that represents the radiation energy level at each wavelength described with the Planck's relation:

$$E_{b\lambda}(\lambda,T)=\frac{C_1}{\lambda^5[exp(C_2/\lambda T)-1]} \qquad (W/m^2.\mu m) \tag{5.1}$$

Where,

$$C_1 = 3.743 \times 10^8 \qquad (W.\mu m^4/m^2)$$
$$C_2 = 1.438 \times 10^4 \qquad (\mu m.K)$$

The spectral distribution of blackbody has maximum values at a specific wavelength and this wavelength has longer values with lower temperatures, in the sense that the maximum wavelength value (peak) is inversely proportional to the corresponding temperature, this relationship was produced by Wien's displacement law as shown in equation (5.2). These concepts with more detail are shown in Figure 5.2 , the Figure reinforces the conception of the maximum value of wavelength is going down as the temperature increases.

$$\lambda_{max} T = 2897.8 \qquad (\mu m.K) \tag{5.2}$$

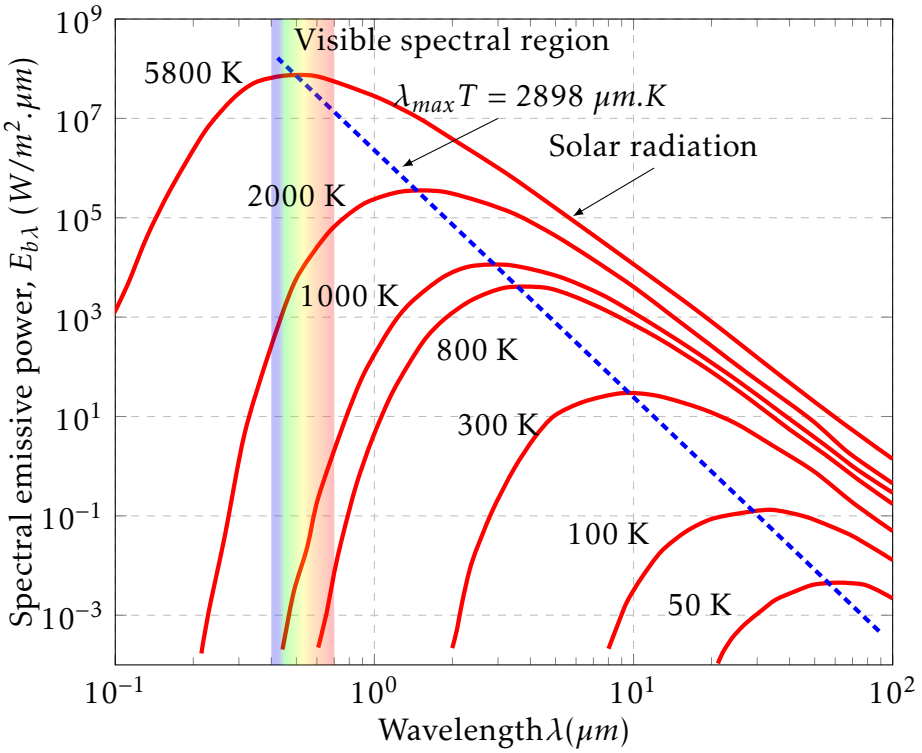

Figure 5.2: Spectral blackbody emissive power [35].

By integrating the intensity of spectral radiation of a blackbody, equation (5.1) over all wavelengths, the emitted radiation of the full body is calculated and it may be expressed as:

$$E_b(T) = \int_0^\infty E_{b\lambda}(\lambda, T) d\lambda = \sigma T^4 \qquad (W/m^2) \tag{5.3}$$

where the Stefan-Boltzmann constant, which depends on C1 and C2, has the numerical value.

$$\sigma = 5.670 \times 10^{-8} \qquad (W/m^2.K^4)$$

As shown in equation (5.3), the amount of radiation emitted of the blackbody proportionally to the fourth power of its absolute temperature.

On the other side, the blackbody described as an ideal surface compared with a real surface, the blackbody is an ideal emitter, in other words, at the same temperature, no surface can emit more radiation than a blackbody Figure 5.3. The radiation intensity emitted from a real surface could be studied as the emissivity multiplied by the radiation intensity emitted from a blackbody at the same temperature, in accordance with:

$$E(\lambda, T) = \mathcal{E}(\lambda, T).E_b(\lambda, T) \qquad (W/m^2) \tag{5.4}$$

Substituting Eqs. (5.3) into (5.4) gives;

$$E(\lambda) = \mathcal{E}(\lambda).\sigma T^4 \qquad (W/m^2) \tag{5.5}$$

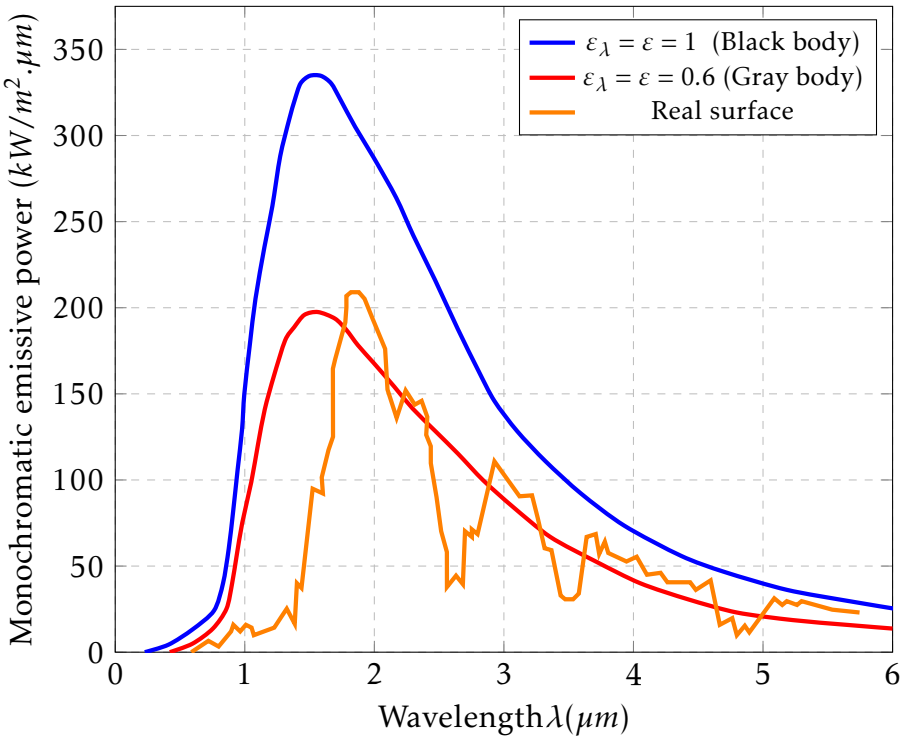

Figure 5.3: Comparison of blackbody and real surface emission [134].

5.1.2 Literature survey

In the last many years, infrared (IR) thermography has turned into an effective optical technique for examining flow field crosswise over complicated geometries, for considering heat exchange or essentially as an analysis device for various applications [127, 135].

Several specialists have utilized the capacities of the infrared thermography in many applications, for example, thermal assessment of electrical hardware [136, 137], perception of plastic deformation [138] , assessment of stress damages in materials [139–141], heat losses in buildings [142–144], observing of deformation [145, 146], examination of heavy machineries [147] and evaluation of machining processes (welding, orthogonal cutting, drilling and milling) [148–151].

The primary IR cameras were created in the 1960s as branches of military projects, be that without exactness features, not suitable to existing needs. Also, It was essentially utilized as a part of space missions, where the insurance of space vehicle in reentry stage was of prime significance [152].

The first practical introductions to gauge heat transfer coefficients were in the mid-1960s when Thomman and Frisk [153] utilized the AGA Thermovision 680SWB operating in a short-wave band 2:5 −5:6 μm to measure the distribution of the temperature on the surface of an elastomeric paraboloid in a hypersonic regime. In this study, the thin-film heat flux sensor was used to measure heat transfer coefficients and compare the results with data of IR system. The study showed good agreement with data obtained with different systems and it was encouraging to measure heat flux by means IR techniques.

During the last three decades,, IR systems have developed into capable investigative tools for thermo-fluid flow examination. Particularly for assessment of different impacts on heat transfer such as surface roughness [154], boundary layer monitoring [135, 152, 155, 156], examining the surface flow field conduct over a range of complicated geometries [127, 135, 152], and existence the surface film cooling [154, 157, 158].

A number of studies have been published to examine the relationship between surface roughness and the emissivity which proved that surface roughness has a deep impact on spectral emissivity [132, 133, 159–161]. Generally, All these studies show that the emissivity increase with surface roughness. This increasing depends on topographical parameters like roughness (rough surface area) and slope (groove angle). In addition, the results of Wen [132, 133, 159, 160] indicate increasing emissivity with increasing temperature and the emissivity is increasing with heating time because of oxidizing the surface

5.2 Experimental set-up

Several improvements carried out on the rig, especially the test section to be more suitable with IR thermal experiences. During the experiments, the test cylinder is heated by increasing the power supply to required limit, until the cylinder reaches the steady state. At that moment, the IR camera recorded all the available data. Then these data are collected and saved as files on the computer. Initially, these data are read through software which accompanies the camera, it is called (Infrared Report Express).

The position and orientation of the thermal camera during the measurements was similar to the one during the calibrations. The camera was set up on the upper side of test section at a distance of 10 cm in other words as close as possible from the heated cylinder to reduce the effect of ambient radiation. Many experiments have been conducted with different factors such as four levels of roughness and three levels of flow rates to assess the impact of these factors individually on the surface temperature distribution.

A set of preliminary tests has been performed to determine the right position for the camera and to determine the time needed for each test for reaching a steady state. Figure 5.4 shows surface temperature of the smooth cylinder with the various flow rate. As can be seen from the figure, the maximum time required to reach a steady state is about 45 minutes in the low flow rate (0.09 kg/s, $Re = 1.6x10^4$). While it take shorter to reach steady state at the highest flow rate (0.5 kg/s, $Re = 8.7x10^4$), because of increasing heat transfer coefficient.

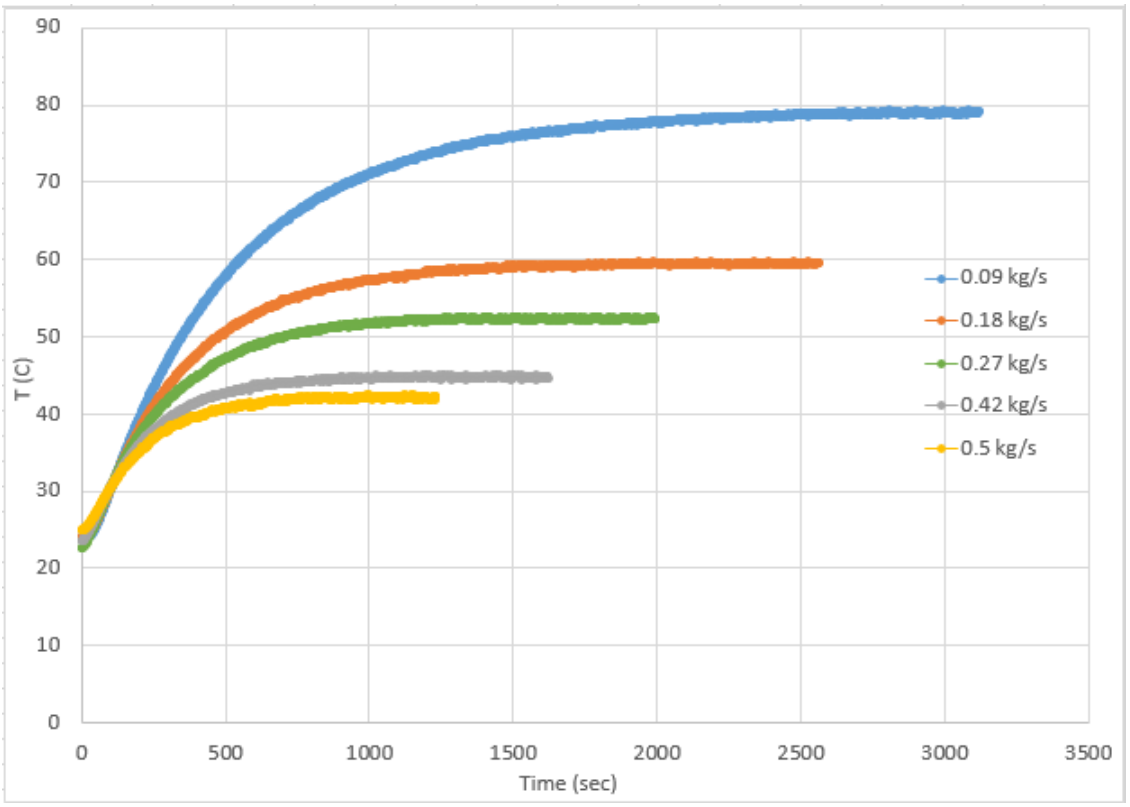

Figure 5.4: Surface temperature variation with time for the smooth cylinder at the different flow rate.

5.2.1 Materials

An IR thermal system is used in this study to compute the surface temperature of heated cylinders by measuring the radiation which emitted from it through an IR transparent sheet. Before the experimental test, the IR imaging camera should be calibrated by providing the camera parameters like the ambient temperature and humidity, distance, and emissivity (where the emissivity of the roughed cylinder surface is 0.1-0.3 [160], and the polished cylinder surface is 0.03 [36]. while plastic has an emissivity about 0.9 [35]). Then the Images that are captured are saved to the memory card then can be relocated to a computer via the USB port or it is also possible to collect data while the camera still connected to a computer.

5.2.1.1 Infrared Camera

The IR optical measurement apparatus that used in this research is (Infrared Thermometer PCE-TC 31) with manual focus and a field of view ($18°x13°$).The field of view (FOV) depends on the viewing distance and on the optics focal length. the camera is operating in the spectral range of $8-14\mu m$, and a ($160x120$) -pixel image resolution format. According to the manufacturer, a measurement

accuracy of ∓2 °C or ∓2% within a temperature range of −20 °C to +350 °C, and with the thermal sensitivity of only 0.1 °C (at 30 °C). The electromagnetic radiation emitted by the heated cylinder first will convert into an electrical signal then will process into an analog representation of the corresponding temperature distribution. To assign temperature bands, the image pixels are represented by the gray tones.

5.2.1.2 IR window System

To allow the infrared camera to scan the temperature distribution on the surface of the cylinder inside test section, an opening of 10x10 cm, Figure 5.5 was cut on the top side of the test section, and IR translucent sheet (Appendix C.1) was used. Some of the thermal radiation emitted by the heated cylinders will reflect and absorb on the translucent sheet, therefore, with each test of IR temperature measurement it is necessary to calibrate the IR camera with the temperature of the thermocouple.

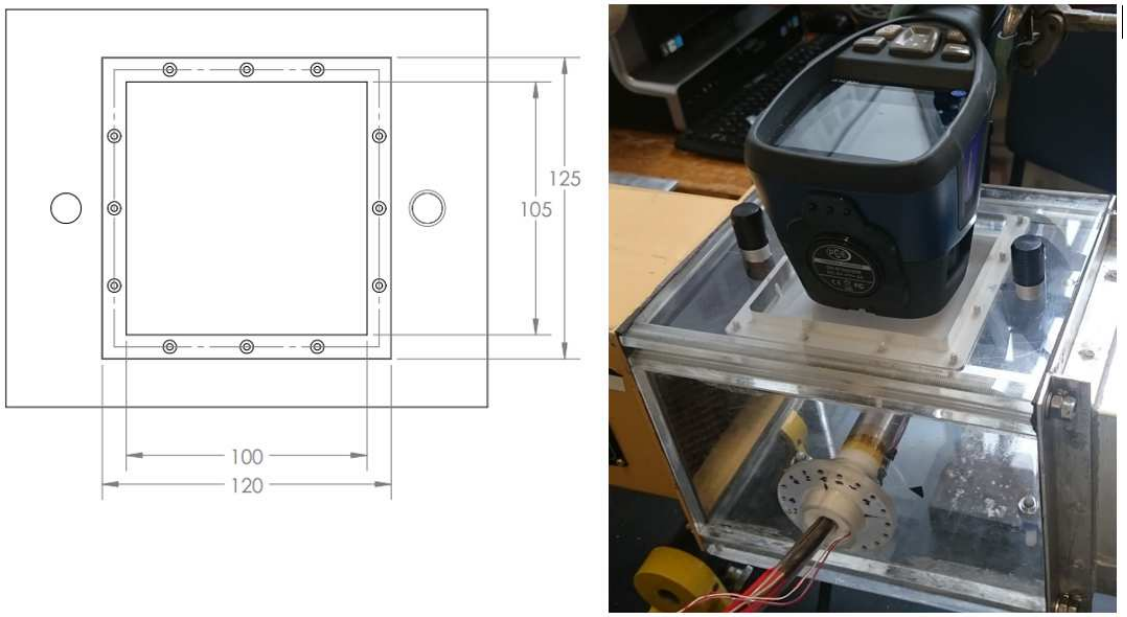

Figure 5.5: Schematic diagram of IR window on the top side of the test section with the Thermographic system.

5.2.2 IR image processing

All images captured by IR technique is consisting of a many of pixels which have several colors. Thus, the image can be regarded as a two- dimensional matrix of pixels according to the size (width and length) of the image. Each element in this matrix has its own gray level in accordance with the color value of the

corresponding pixel in the image. For instance, the gray level 255 equal to the white color, in other sense, the largest value in the IR image, and the gray level 0 equal to the black color which represents the smallest value in the IR image, while, the gray levels between them represents different color values depending on the corresponding gray values. This image processing technique was used to convert the color image to a gray image with 256 gray levels. After conversion, a three-dimensional view can be showed to examine the surface temperature map. In this study, the ImageJ software was used to convert the color images to gray images and it and (Infrared Report Express) software were used to extract and process the data.

5.2.3 Calibration of the temperature measured by IR camera Temperatures

Before the infrared temperature measurements, it is necessary to measure the temperature of the heating cylinder with a thermocouple and black body tape (emissivity= 0.95) which have adhered to the centre of the heating cylinder, as showen in Figure 5.6.

IR and thermocouple measurements are taken at same time. The number of pixel counts in a selected region (covered by the thermocouple, Figure 5.6) is registered by the IR camera and its accompanying software, while the thermocouple measures the surface temperature in degrees Celsius. From the series of measurements, the calibration is performed, the relationship is roughly linear, for the tested temperature ranges, as shown in Figure 5.7. Once this calibration is obtained, the surface thermocouple position is changed (by rotating the cylinder about 180^{o}), to allow IR camera of the entire heating cylinder. To ensure accurate data reduction, this calibration step is performed with each test run. From Figure 5.7, it can be seen that there are some bumps in the calibration line with IR translucent sheet also the slope of the calibration curve is changing compared with sheet absence line, these occur as result of the properties of IR sheet (transmission) which it is not stable along IR band (8-14 μm) (IR sheet properties in Appendix C.1).

On the other hand, the size of the images is calibrated using about $(5x5)\ mm^2$ black-coloured Teflon (high emissivity). In the IR images Figure 5.6, the colour contrast is used for that purpose, and the hot spot denotes the area marked by the square black tape.

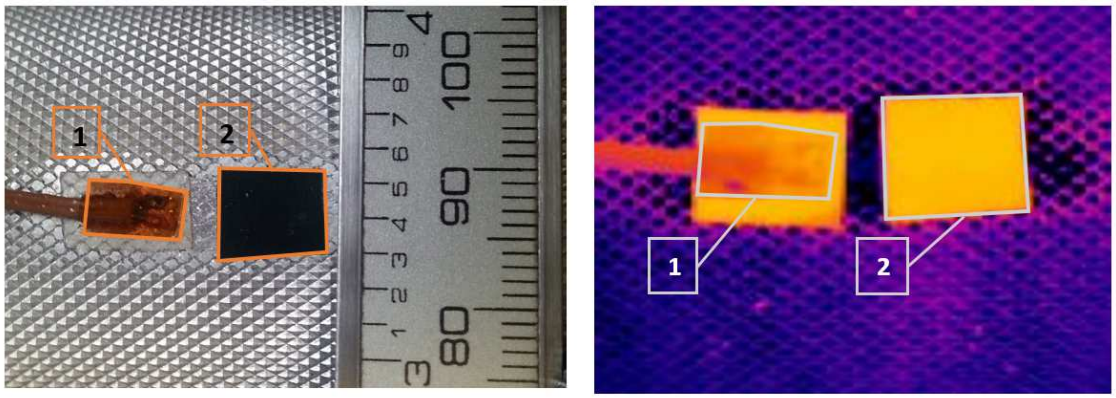

Figure 5.6: Calibration of the IR image

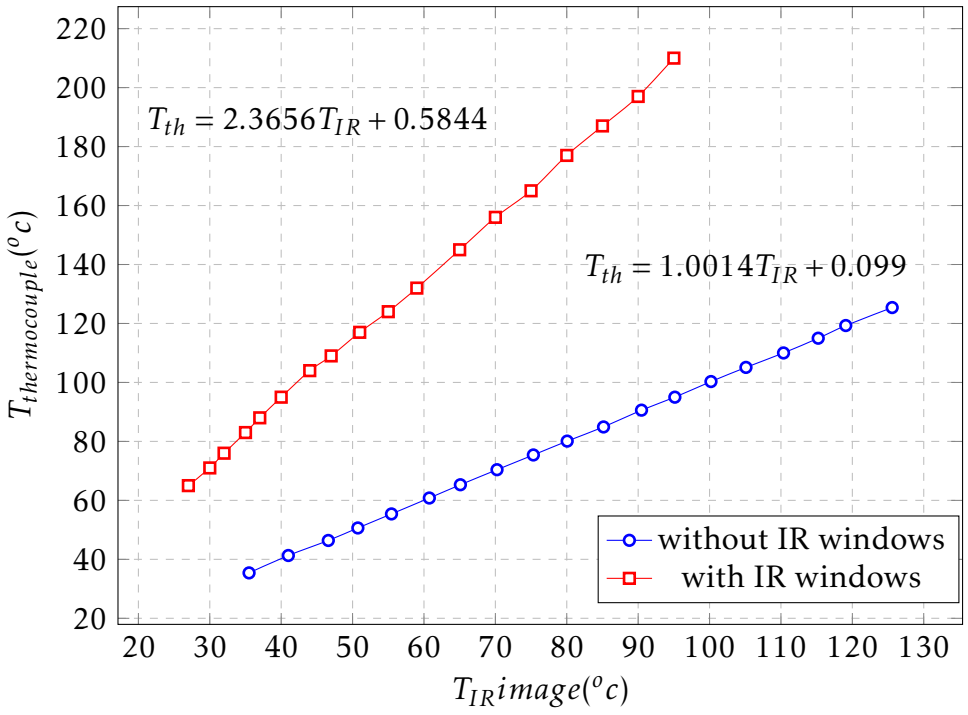

Figure 5.7: Calibration curve of the IR image as measured through the translucent sheet.

5.3 Results and Discussion

The surface temperature distribution for the entire cylinder with high roughness at Re = $1.6x10^4$, shown in Figure 5.8, It can be observed that in the direction of flow, the value of the temperature drops to the front and rear recesses which can be

attributed to the increase of the heat transfer coefficient at these points (as shown in sec.4.1.2) and to the difference in the observation angle (emissivity decrease). In addition, Figure 5.8 demonstrates the good symmetry of temperature distribution at the cylinder surface from centre-line and the highest surface temperature occurs at the middle of the cylinder about 90^o from stagnation line, in other words, at the lowest Nusselt numbers (sec.4.1.2). The temperature of thermal insulation at the ends of cylinder seem larger than cylinder because of emissivity difference.

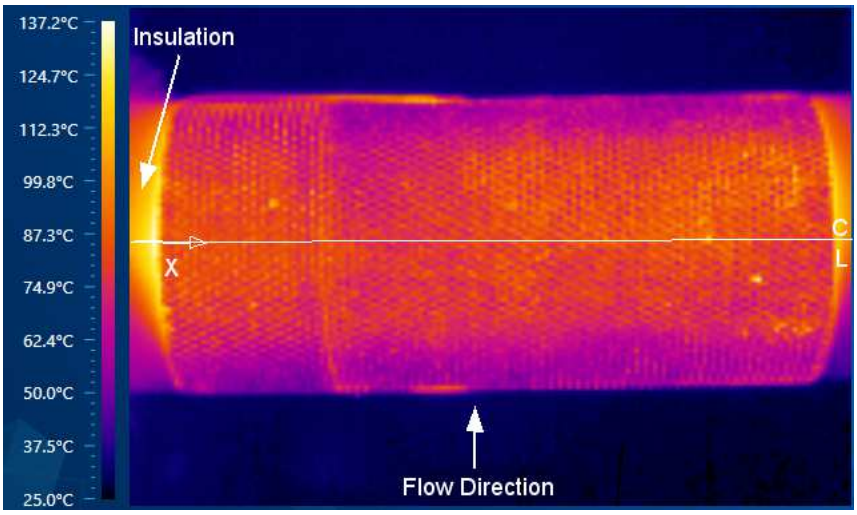

Figure 5.8: Distributions of the temperature for the high roughness cylinder ($\epsilon/D = 725 * 10^{-5}$) at low flow rate (Re = $1.6x10^4$).

The results of the infrared thermo-vision for steady state temperature distribution on the surface cylinder for different flow rate are presented in Figures (5.9 - 5.14) which include three levels of surface roughness. Figure 5.15 shows temperature profile within the thermal boundary layer of three rough cylinders along centre-line (90^o from the stagnation line) for different Re numbers.

These Figures show hot and cold spots at locations corresponding to valleys and peaks respectively on the rough surface. In addition, they show at the same power supply (65 Watts), the temperature differences between peaks and valleys increases with the decrease of Re. For instance, on the high roughness surface ($\epsilon/D = 725x10^{-5}$) are about 9 °C and 24 °C at Reynolds numbers 87000 and 16000 respectively, Figures 5.10 and 5.9.

By the assumption that the semi-regular roughness is extended surfaces. There are two important issues. Firstly, the thermal conductivity of cylinders material has a strong impact on the distribution of temperature along the extended surface (rough surface), Which at high Re number (i.e. low boundary layer thickness), helps to reduce a maximum to a minimum temperature difference, Figure 5.15. Secondly, the extended surfaces (roughness) have large effect under conditions which the heat transfer coefficient (h) is small and/or at low Reynolds Numbers (i.e. a high boundary layer thickness). Hence, the roughness peaks exhibit a

faster temperature response because of elevated convective heat transfer for the flow close from the peaks (where the effect of the main stream). While higher air temperatures close from the surface inside the thermal boundary layer (at roughness base).

A mean value and a standard deviation (RMS) for the temperature distributions are shown in Figure 5.16 and 5.17, respectively. As shown in Figure 5.16 and by comparing thermal images in Figures (5.9 - 5.14). It can see that the temperatures gradient stayed at the same tendency for all the flow rates and the maximum temperature occurs at low flow rates. Furthermore, as a result of the roughness of the surface, the temperature distribution is dramatically lower for the high roughness ($\epsilon/D = 7.25 \times 10^{-3}$) than it for the low roughness ($\epsilon/D = 113x10^{-5}$). This decline in temperature distribution results from increasing the heat transfer in the high roughness compared with other cases. Moreover, as can be seen from Figure 5.17 that the standard deviation (RMS) of the temperature fluctuations in the transverse direction decreases as Re numbers Increase, and it's always in maximum value for each flow rates at the high roughness ($\epsilon/D = 7.25 \times 10^{-3}$).

In summary, Infrared thermography technique appeared as a very powerful tool which can use to investigate the thermal boundary layer behavior and its effect on surface temperature. Where it showed clearly that due to the interaction between boundary layer and roughness, the temperature of the rough element (fin) have large value at the base where higher air temperatures close from the wall, inside the thermal boundary layer, and gradually decrease towards the roughness peak due to high heat transfer coefficient close from the peaks. So, the maximum to minimum temperature difference depends heavily on element heigh (roughness) and thickness of boundary layers (Re numbers).

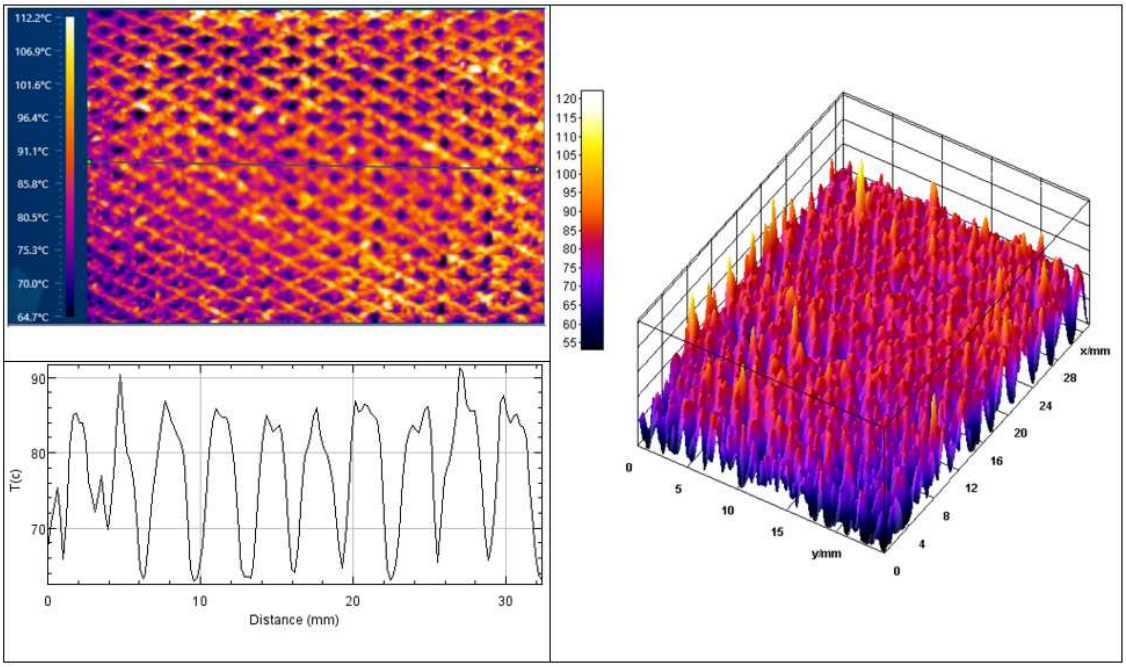

Figure 5.9: Temperature map and temperature profile along the centerline of thermal image for rough cylinder ($\epsilon/D = 7.25 \times 10^{-3}$) at Re = $1.6x10^4$.

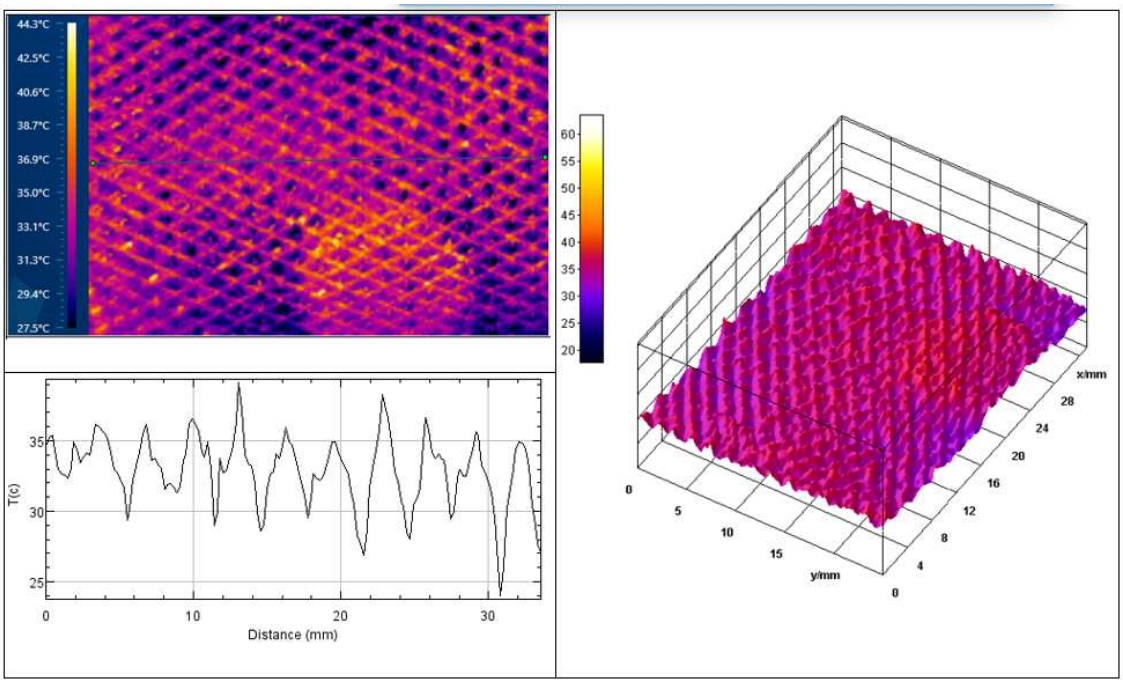

Figure 5.10: Temperature map and temperature profile along the centerline of thermal image for rough cylinder ($\epsilon/D = 7.25 \times 10^{-3}$) at Re =$8.7x10^4$.

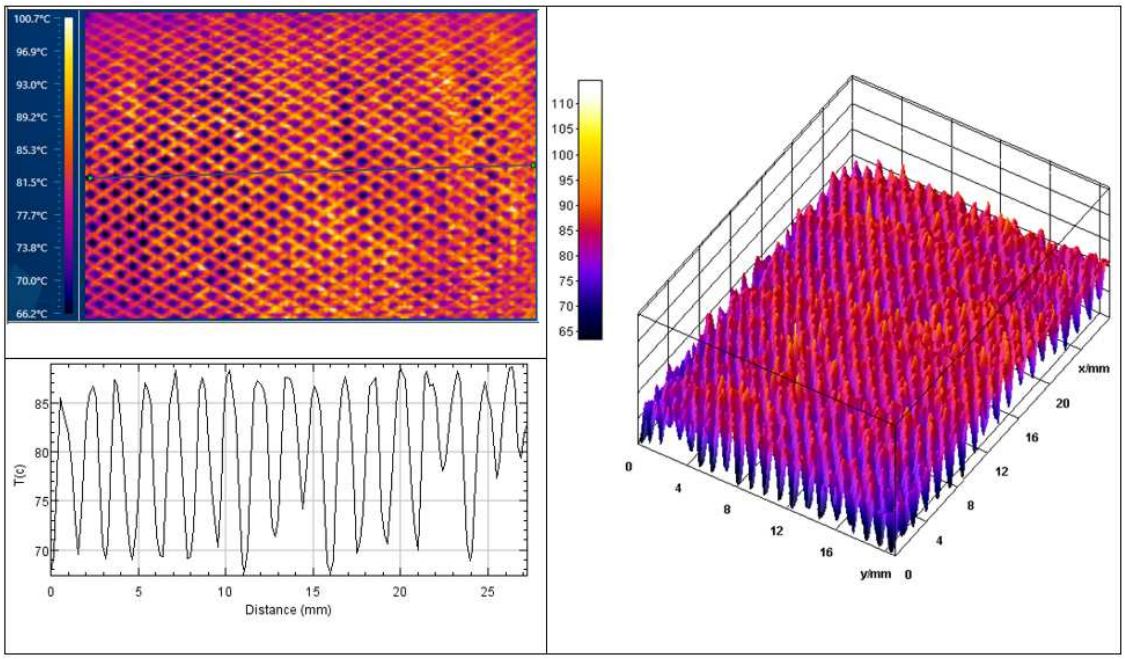

Figure 5.11: Temperature map and temperature profile along the centerline of thermal image for rough cylinder ($\epsilon/D = 3.25 \times 10^{-3}$) at Re = $1.6x10^4$.

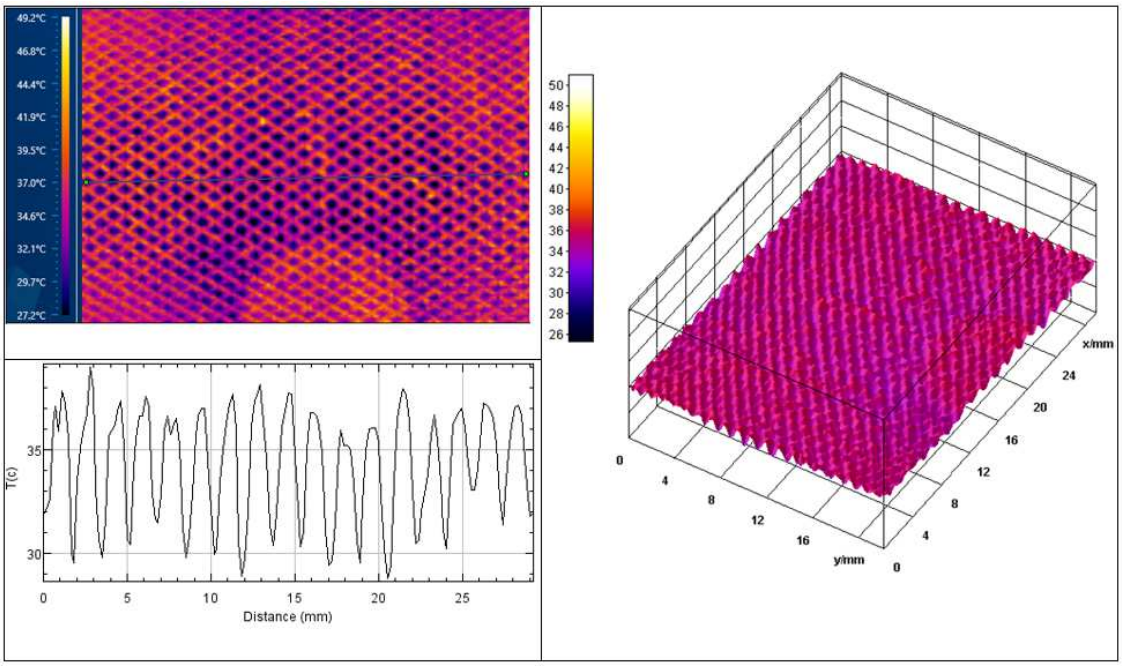

Figure 5.12: Temperature map and temperature profile along the centerline of thermal image for rough cylinder ($\epsilon/D = 3.25 \times 10^{-3}$) at Re = $8.7x10^4$.

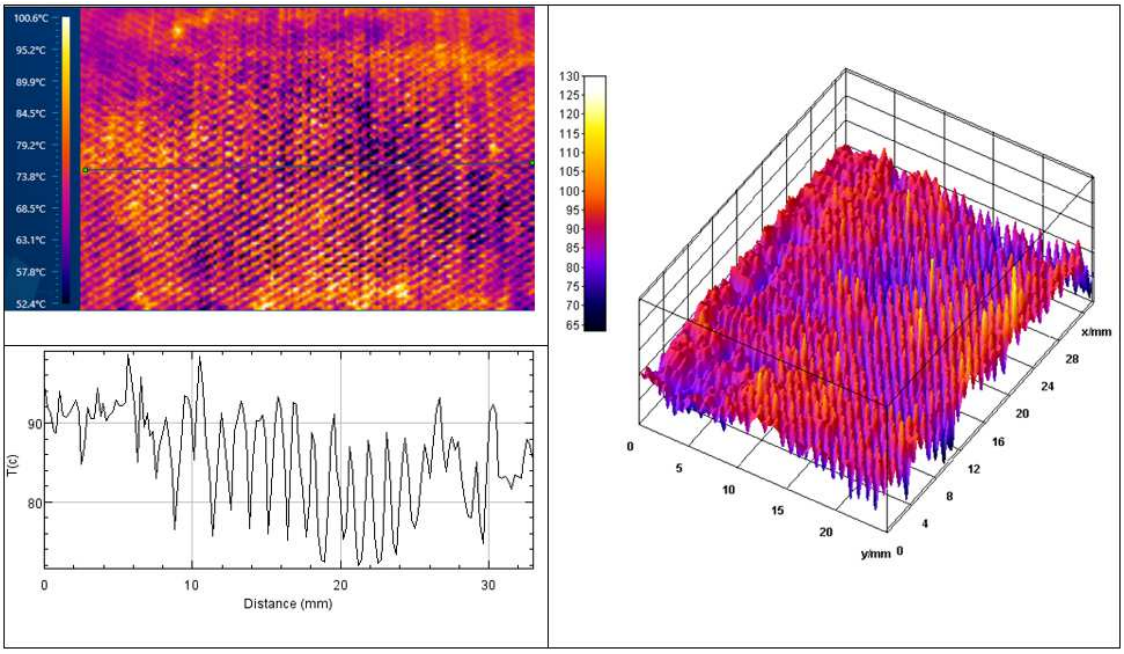

Figure 5.13: Temperature map and temperature profile along the centerline of thermal image for rough cylinder ($\epsilon/D = 1.13 \times 10^{-3}$) at Re = $1.6x10^4$.

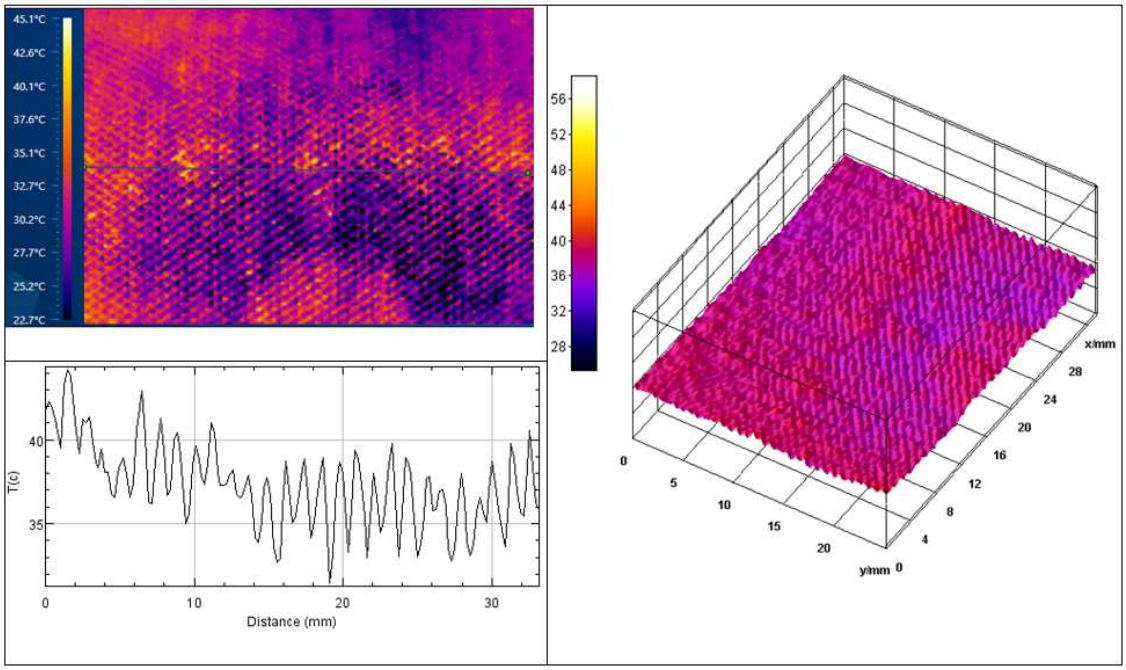

Figure 5.14: Temperature map and temperature profile along the centerline of thermal image for rough cylinder ($\epsilon/D = 1.13 \times 10^{-3}$) at Re = $8.7x10^4$.

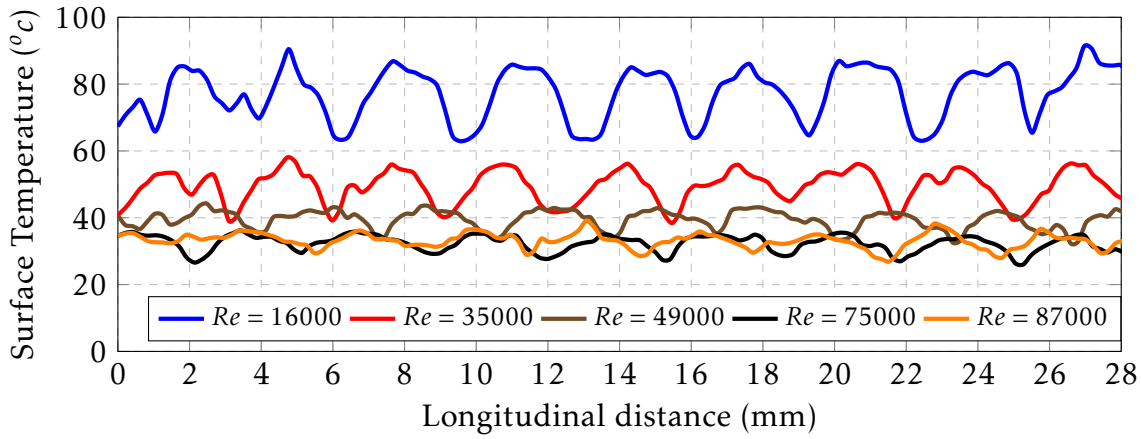

(a) $\epsilon/D = 7.25 \times 10^{-3}$

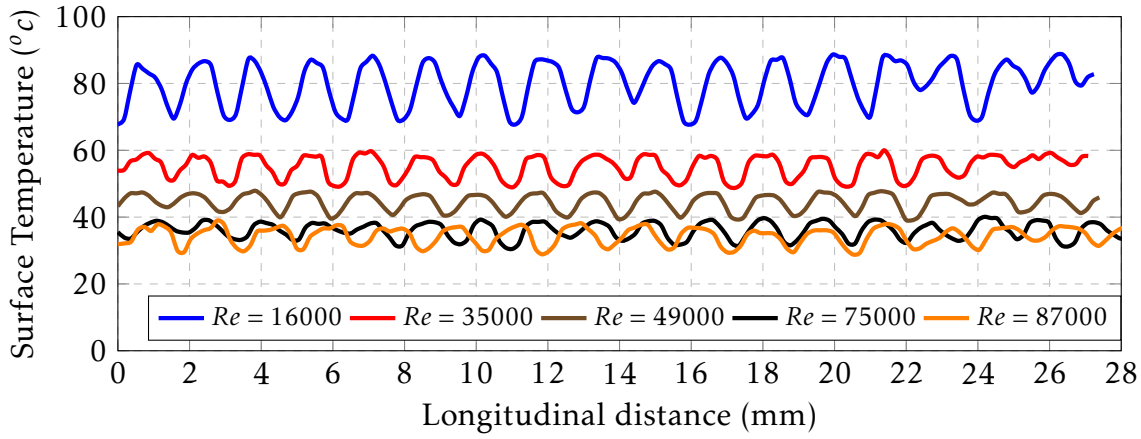

(b) $\epsilon/D = 3.25 \times 10^{-3}$

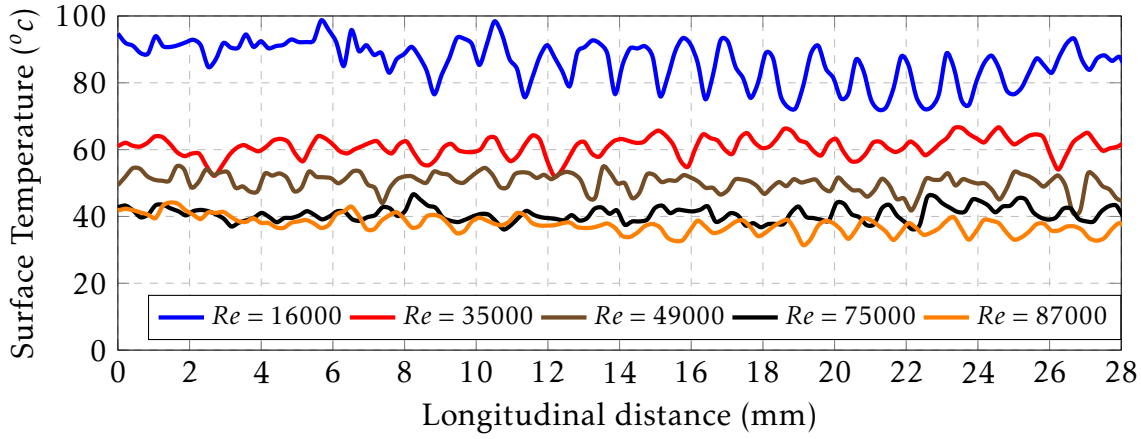

(c) $\epsilon/D = 1.13 \times 10^{-3}$

Figure 5.15: Temperature distributions within the thermal boundary layer of the rough cylinders at centreline 90^o from the stagnation line for different Re numbers and surface roughness's.

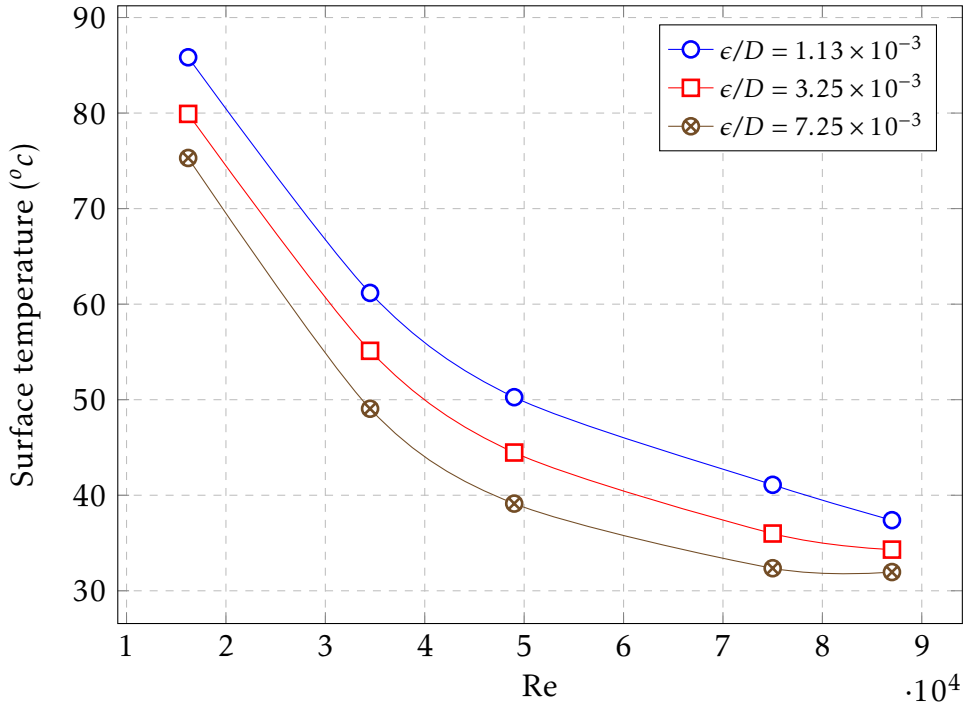

Figure 5.16: A mean value for the surface temperature as a function of Reynolds Numbers for different surface roughnesses.

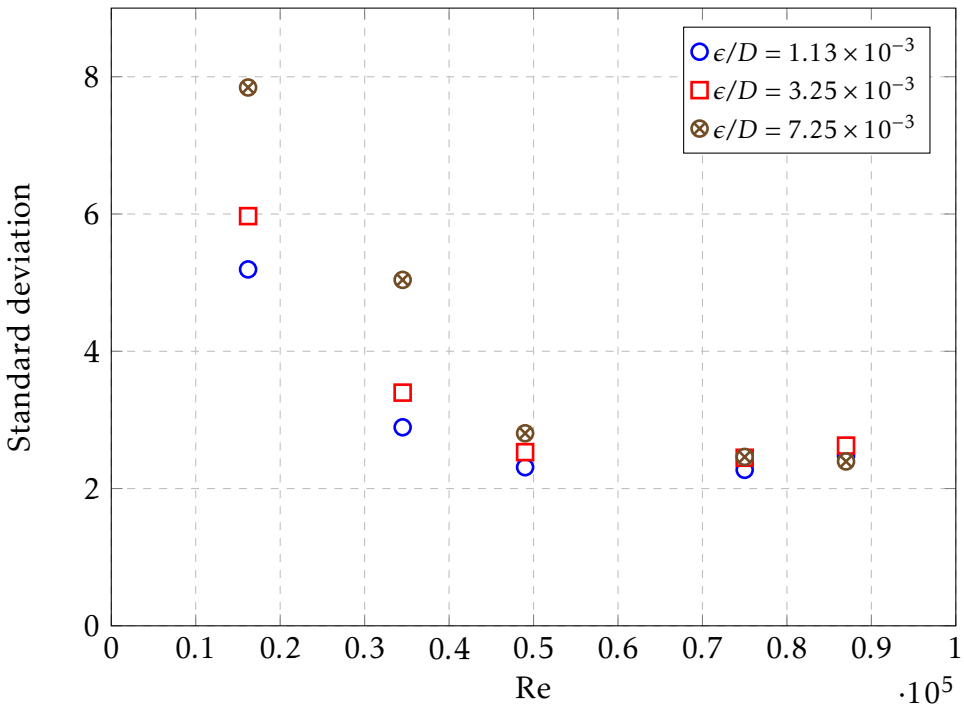

Figure 5.17: A standard deviation for the surface temperature as a function of Reynolds Numbers for different surface roughnesses.

CHAPTER 6

Conclusions and Future work

6.1 Conclusions

The effect of free-stream turbulence and surface-roughness on heat transfer from cylinders in cross flow was experimentally investigated for a range of Reynolds numbers ($16000 \leqslant Re \leqslant 87000$) and a blockage ratio $\beta = 40\%$. Four levels of surface roughness ($0 < \epsilon/D < 7.25 \times 10^{-3}$) were manufactured. Experiments were carried out in an open-circuit wind tunnel. Heat flux sensors were used to calculate heat transfer coefficient, while hot-wire anemometry was employed to measure mean velocities and the flow turbulence characteristics. Turbulence intensity levels were varied independently to Reynolds number using perforated plates, values of up to 10% were achieved. An IR thermal camera was used to obtain temperature maps of the cylinder surfaces. Both the free-stream turbulence and surface roughness were found to modify the boundary layer around the cylinder enhancing the heat transfer.

The main conclusions are:

- The heat transfer was found to increase with the turbulence intensity. The turbulence intensity had little impact at low flow rates. Increasing turbulence levels (from 2.2% to 9.7%) resulted in an increase in the heat transfer at the front of the smooth cylinder as the separation point was displaced downstream, this helped to increase heat transfer rate from the entire cylinder by about 13 %. Changes in turbulence length scale were found to have little effect.

- The blockage ratio used in these tests was generally higher than that other workers (40% compared to typical values of 20%). This was necessary to achieve the desired Reynolds numbers. This resulted in higher heat transfer due to increased velocities around the cylinder. The Strouhal number was also increased compared to workers who used a smaller blockage ratio.

- Cylinder roughness accelerated the occurrence of the turbulent boundary layer resulting in improved heat transfer. The angular position of the boundary layer transition moved upstream, towards the front stagnation point as the roughness was increased. Compared to the smooth cylinders the heat transfer rate increased by 11% for the fine surface roughness ($\epsilon/D = 113x10^{-5}$), and 46% in the high surface roughness ($\epsilon/D = 7.25 \times 10^{-3}$), at $7.5x10^{4}$.

- The combined impact of roughness and turbulence intensity significantly increased heat transfer. The critical Reynolds number decreased as both surface roughness and free stream turbulence increased. However, the surface roughness had a dominant influence. Increasing of turbulence intensity from 2.2% to 9.7% gave a 45% increase in heat transfer for ($\epsilon/D = 113x10^{-5}$), however for a higher roughness of ($\epsilon/D = 7.25 \times 10^{-3}$) the mean heat transfer

increased by 80%. Whilst changing turbulent intensity mainly impacted heat transfer on the front part of the cylinder surface roughness increased heat transfer across the whole surface.

- The thermal camera images showed that the temperature of the base was higher than the extended rough elements. From this it was concluded that the thermal boundary layer was of a similar order to the roughness. At low flow rates a larger base to tip temperature difference was observed due to the thicker boundary layer. As the Reynolds number increased the tip to base temperature difference decreased due to the shrinking boundary layer resulting in a steeper temperature gradient across the extended elements hence enhancing heat transfer.

6.2 Recommendations for future work

In view of the previous conclusions and the present comprehension of the impact surface roughness and FST on flow behaviour and boundary layer around the circular cylinder, the following list of recommendations are relevant for future work:

- A more comprehensive assessment of the roughness and FST effect requires further investigation by using various types of roughness and different types of Turbulence-Generating Grid for a wider range of Reynolds number to affirm the present conclusions.

- Experimental work may cover the velocity components and flow behaviour around the cylinder using PIV system since this will present an additional explanation of the effects of surface roughness on the flow dynamics.

- It would be interesting to see the effect of surface roughness and FST on flow characteristics, by using a porous layer around the cylinder to increase surface roughness and enhance of heat transfer and using polymers (hydrophobic material) to reduce surface roughness and drag coefficient.

- This study demonstrates that extensive research is yet required for complete comprehension of the impact of roughness and FST on liquid flow (various Pr number) around cylinders.

- Combining IR camera and CFD results might be more developed to better assess for heat transfer rates and make it more useful.

References

[1] MM Zdravkovich. The effects of interference between circular cylinders in cross flow. *Journal of fluids and structures*, 1(2):239–261, 1987.

[2] A Zukauskas and J Ziugzda. Heat transfer of a cylinder in crossflow. *Washington, DC, Hemisphere Publishing Corp., 1985, 219 p. Translation.*, 1, 1985.

[3] WH Giedt. Investigation of variation of point unit heat-transfer coefficient around a cylinder normal to an air stream. *Trans. ASME*, 71(375-381):147, 1949.

[4] RM Fand and KK Keswani. A continuous correlation equation for heat transfer from cylinders to air in crossflow for Reynolds numbers from 10^{-2} to 2×10^5. *International Journal of Heat and Mass Transfer*, 15(3):559–562, 1972.

[5] Hajime Nakamura and Tamotsu Igarashi. Variation of nusselt number with flow regimes behind a circular cylinder for Reynolds numbers from 70 to 30000. *International journal of heat and mass transfer*, 47(23):5169–5173, 2004.

[6] BG Van Der Hegge Zijnen. Modified correlation formulae for the heat transfers by natural and by forced convection from horizontal cylinders. *Applied Scientific Research, Section A*, 6(2-3):129–140, 1956.

[7] A Zukauskas. Heat transfer from tubes in cross-flow. *advances in heat transfer*, 18:87, 1987.

[8] AA McKillop. Heat transfer from a single cylinder, cylinders in tandem, and cylinders in the entrance region of a tube bank with a uniform heat flux. 1986.

[9] JS Kraabel, AA McKillop, and JW Baughn. Heat transfer to air from a yawed cylinder. *International Journal of Heat and Mass Transfer*, 25(3):409–418, 1982.

[10] Maher I Boulos and David CT Pei. Dynamics of heat transfer from cylinders in a turbulent air stream. *International Journal of Heat and Mass Transfer*, 17(7):767–783, 1974.

[11] S Sanitjai and RJ Goldstein. Forced convection heat transfer from a circular cylinder in crossflow to air and liquids. *International journal of heat and mass transfer*, 47(22):4795–4805, 2004.

[12] Ertan Buyruk. Heat transfer and flow structures around circular cylinders in cross-flow. *Turkish Journal of Engineering and Environmental Sciences*, 23(5):299–316, 1999.

[13] Christoffer Norberg. Effects of Reynolds number and a low-intensity freestream turbulence on the flow around a circular cylinder. *Chalmers University, Goteborg, Sweden, Technological Publications*, 87(2), 1987.

[14] JP Batham. Pressure distributions on circular cylinders at critical Reynolds numbers. *Journal of Fluid Mechanics*, 57(02):209–228, 1973.

[15] Oktay Güven, Cesar Farell, and VC Patel. Surface-roughness effects on the mean flow past circular cylinders. *Journal of Fluid Mechanics*, 98(04):673–701, 1980.

[16] Guido Buresti. The effect of surface roughness on the flow regime around circular cylinders. *Journal of Wind Engineering and Industrial Aerodynamics*, 8(1):105–114, 1981.

[17] E Achenbach and E Heinecke. On vortex shedding from smooth and rough cylinders in the range of Reynolds numbers 6×10^3 to 5×10^6. *Journal of fluid mechanics*, 109:239–251, 1981.

[18] MM Zdravkovich. Conceptual overview of laminar and turbulent flows past smooth and rough circular cylinders. *Journal of wind engineering and industrial aerodynamics*, 33(1):53–62, 1990.

[19] WCL Shih, C Wang, D Coles, and A Roshko. Experiments on flow past rough circular cylinders at large Reynolds numbers. *Journal of Wind Engineering and Industrial Aerodynamics*, 49(1-3):351–368, 1993.

[20] SJ Zan. Experiments on circular cylinders in crossflow at Reynolds numbers up to 7 million. *Journal of Wind Engineering and Industrial Aerodynamics*, 96(6):880–886, 2008.

[21] Christoffer Norberg. Fluctuating lift on a circular cylinder: review and new measurements. *Journal of Fluids and Structures*, 17(1):57–96, 2003.

[22] Che-Chun Jim Chang, R Ajith Kumar, and Michael M Bernitsas. VIV and galloping of single circular cylinder with surface roughness at $3\times10^4 \leqslant Re \leqslant 1.2\times10^5$. *Ocean Engineering*, 38(16):1713–1732, 2011.

[23] Hongrae Park, R Ajith Kumar, and Michael M Bernitsas. Enhancement of flow-induced motion of rigid circular cylinder on springs by localized surface roughness at $3\times10^4 \leqslant Re \leqslant 1.2\times10^5$. *Ocean Engineering*, 72:403–415, 2013.

[24] Nils Paul van Hinsberg. The Reynolds number dependency of the steady and unsteady loading on a slightly rough circular cylinder: From subcritical up to high transcritical flow state. *Journal of Fluids and Structures*, 55:526–539, 2015.

[25] Anatol Roshko. Experiments on the flow past a circular cylinder at very high Reynolds number. *Journal of Fluid Mechanics*, 10(3):345–356, 1961.

[26] E Achenbach. Distribution of local pressure and skin friction around a circular cylinder in cross-flow up to Re= 5×10^6. *Journal of Fluid Mechanics*, 34(4):625–639, 1968.

[27] Elmar Achenbach. Influence of surface roughness on the cross-flow around a circular cylinder. *Journal of Fluid Mechanics*, 46(02):321–335, 1971.

[28] George W Jones and Robert W Walker. *Aerodynamic forces on a stationary and oscillating circular cylinder at high Reynolds numbers*, volume 300. National Aeronautics and Space Administration, 1969.

[29] W Paris. A study of viscous cross-flow effects on circular cylinders at high Reynolds numbers. 1979.

[30] Günter Schewe. On the force fluctuations acting on a circular cylinder in crossflow from subcritical up to transcritical Reynolds numbers. *Journal of fluid mechanics*, 133:265–285, 1983.

[31] Günter Schewe. Sensitivity of transition phenomena to small perturbations in flow round a circular cylinder. *Journal of fluid mechanics*, 172:33–46, 1986.

[32] SJ Zan and K Matsuda. Steady and unsteady loading on a roughened circular cylinder at Reynolds numbers up to 900,000. *Journal of Wind Engineering and Industrial Aerodynamics*, 90(4):567–581, 2002.

[33] GS West and CJ Apelt. The effects of tunnel blockage and aspect ratio on the mean flow past a circular cylinder with Reynolds numbers between 10^4 and 10^5. *Journal of Fluid Mechanics*, 114:361–377, 1982.

[34] H Peller, V Lippig, D Straub, and R Waibel. Thermofluiddynamic experiments with a heated and rotating circular cylinder in crossflow. *Experiments in fluids*, 2(3):113–120, 1984.

[35] Theodore L Bergman, Frank P Incropera, David P DeWitt, and Adrienne S Lavine. *Fundamentals of heat and mass transfer*. John Wiley & Sons, 2011.

[36] A Cengel Yunus et al. *Heat transfer: a practical approach*. MacGraw-Hill,, 2003.

[37] Anatol Roshko and W Fiszdon. *On the persistence of transition in the near-wake*. Society for Industrial and Applied Mathematics, 1969.

[38] Elmar Achenbach. The effect of surface roughness on the heat transfer from a circular cylinder to the cross flow of air. *International Journal of Heat and Mass Transfer*, 20(4):359–369, 1977.

[39] PW Bearman and T Morel. Effect of free stream turbulence on the flow around bluff bodies. *Progress in aerospace sciences*, 20(2-3):97–123, 1983.

[40] A Zukauskas, P Vaitiekunas, and J Ziugzda. Analysis of influence of free stream turbulence intensity and integral length scale on skin friction and heat transfer of a circular cylinder. In *Experimental Heat Transfer, Fluid Mechanics, and Thermodynamics 1993*, page 591, 1993.

[41] Algirdas Zukauskas, Petras Vaitiekunas, and Juozas Vytautas Ziugzda. Heat transfer from cylinders in transverse flows of highly variable turbulence. *Heat Transfer Research*, 33(3&4), 2002.

[42] Shuichi Torii and Wen-Jei Yang. Effects of the length scale of free-stream turbulence and cylinder size on local heat transfer in laminar separated flows. *EXPERIMENTAL HEAT TRANSFER An International Journal*, 6(2):175–187, 1993.

[43] C Sak, R Liu, DS-K Ting, and GW Rankin. The role of turbulence length scale and turbulence intensity on forced convection from a heated horizontal circular cylinder. *Experimental thermal and fluid science*, 31(4):279–289, 2007.

[44] KJA Westin, AV Boiko, BGB Klingmann, VV Kozlov, and PH Alfredsson. Experiments in a boundary layer subjected to free stream turbulence. Part 1. boundary layer structure and receptivity. *Journal of Fluid Mechanics*, 281:193–218, 1994.

[45] KJA Westin, AA Bakchinov, VV Kozlov, and PH Alfredsson. Experiments on localized disturbances in a flat plate boundary layer. Part 1. the receptivity and evolution of a localized free stream disturbance. *European Journal of Mechanics-B/Fluids*, 17(6):823–846, 1998.

[46] AV Boiko, KJA Westin, BGB Klingmann, VV Kozlov, and PH Alfredsson. Experiments in a boundary layer subjected to free stream turbulence. Part 2. the role of TS-waves in the transition process. *Journal of Fluid Mechanics*, 281:219–245, 1994.

[47] Pavel Jonáš, Oton Mazur, and Václav Uruba. On the receptivity of the by-pass transition to the length scale of the outer stream turbulence. *European Journal of Mechanics-B/Fluids*, 19(5):707–722, 2000.

[48] PH Alfredsson and Masaharu Matsubara. Free-stream turbulence, streaky structures and transition in boundary layer flows. *AIAA paper*, 2534, 2000.

[49] M Matsubara and P Henrik Alfredsson. Disturbance growth in boundary layers subjected to free-stream turbulence. *Journal of Fluid Mechanics*, 430:149–168, 2001.

[50] Luca Brandt, Philipp Schlatter, and Dan S Henningson. Transition in boundary layers subject to free-stream turbulence. *Journal of Fluid Mechanics*, 517:167–198, 2004.

[51] Lars-Uve Schrader, Subir Amin, and Luca Brandt. Transition to turbulence in the boundary layer over a smooth and rough swept plate exposed to free-stream turbulence. *Journal of Fluid Mechanics*, 646:297–325, 2010.

[52] M Gundappa and TE Diller. The effects of free-stream turbulence and flow pulsation on heat transfer from a cylinder in crossflow. *Journal of heat transfer*, 113(3):766–769, 1991.

[53] Imed Khabbouchi, Hachimi Fellouah, Mohsen Ferchichi, and Mohamed Sadok Guellouz. Effects of free-stream turbulence and Reynolds number on the separated shear layer from a circular cylinder. *Journal of Wind Engineering and Industrial Aerodynamics*, 135:46–56, 2014.

[54] JW Scholten and DB Murray. Unsteady heat transfer and velocity of a cylinder in cross flow *i*. low freestream turbulence. *International journal of heat and mass transfer*, 41(10):1139–1148, 1998.

[55] JW Scholten and DB Murray. Unsteady heat transfer and velocity of a cylinder in cross flow *ii*. high freestream turbulence. *International journal of heat and mass transfer*, 41(10):1149–1156, 1998.

[56] GJ VanFossen and RJ Simoneau. A study of the relationship between free-stream turbulence and stagnation region heat transfer. *Journal of heat transfer*, 109(1):10–15, 1987.

[57] S Sanitjai and RJ Goldstein. Effect of free stream turbulence on local mass transfer from a circular cylinder. *International journal of heat and mass transfer*, 44(15):2863–2875, 2001.

[58] Frédéric Peyrin and Alain Kondjoyan. Effect of turbulent integral length scale on heat transfer around a circular cylinder placed cross to an air flow. *Experimental thermal and fluid science*, 26(5):455–460, 2002.

[59] HM Blackburn and WH Melbourne. The effect of free-stream turbulence on sectional lift forces on a circular cylinder. *Journal of Fluid Mechanics*, 306:267–292, 1996.

[60] Marianna Braza, Rodolphe Perrin, and Yannick Hoarau. Turbulence properties in the cylinder wake at high Reynolds numbers. *Journal of fluids and Structures*, 22(6):757–771, 2006.

[61] Robert D Blevins. Applied fluid dynamics handbook. *New York, Van Nostrand Reinhold Co., 1984, 568 p.*, 1, 1984.

[62] Michael P Schultz and Karen A Flack. Turbulent boundary layers over surfaces smoothed by sanding. *Journal of fluid engineering*, 125(5):863–870, 2003.

[63] Johann Nikuradse. *Laws of flow in rough pipes*. National Advisory Committee for Aeronautics Washington, 1950.

[64] DJ Bergstrom, MF Tachie, and R Balachandar. Application of power laws to low Reynolds number boundary layers on smooth and rough surfaces. *Physics of Fluids (1994-present)*, 13(11):3277–3284, 2001.

[65] Vl Gomelauri. Influence of two-dimensional artificial roughness on convective heat transfer. *International Journal of Heat and Mass Transfer*, 7(6):653–663, 1964.

[66] P-Å Krogstadt and RA Antonia. Surface roughness effects in turbulent boundary layers. *Experiments in Fluids*, 27(5):450–460, 1999.

[67] V Kolář. Heat transfer in turbulent flow of fluids through smooth and rough tubes. *International Journal of Heat and Mass Transfer*, 8(4):639–653, 1965.

[68] Fujii Tetsu, Fujii Motoo, and Takeuchi Masanori. Influence of various surface roughness on the natural convection. *International Journal of Heat and Mass Transfer*, 16(3):629–636, 1973.

[69] Tetuya Kawamura, Hideo Takami, and Kunio Kuwahara. Computation of high Reynolds number flow around a circular cylinder with surface roughness. *Fluid Dynamics Research*, 1(2):145, 1986.

[70] D Lakehal. Computation of turbulent shear flows over rough-walled circular cylinders. *Journal of Wind Engineering and Industrial Aerodynamics*, 80(1):47–68, 1999.

[71] F Dierich and PA Nikrityuk. A numerical study of the impact of surface roughness on heat and fluid flow past a cylindrical particle. *International Journal of Thermal Sciences*, 65:92–103, 2013.

[72] James B Taylor, Andres L Carrano, and Satish G Kandlikar. Characterization of the effect of surface roughness and texture on fluid flow - past, present, and future. *International journal of thermal sciences*, 45(10):962–968, 2006.

[73] A Žukauskas. Enhancement of forced convection heat transfer in viscous fluid flows. *International journal of heat and mass transfer*, 37:207–212, 1994.

[74] CF Lange, F Durst, and Momentum Breuer. Momentum and heat transfer from cylinders in laminar crossflow at $10^{-4} \leqslant \mathrm{Re} \leqslant 200$. *International Journal of Heat and Mass Transfer*, 41(22):3409–3430, 1998.

[75] Gh Juncu. Unsteady conjugate heat/mass transfer from a circular cylinder in laminar crossflow at low Reynolds numbers. *International journal of heat and mass transfer*, 47(10):2469–2480, 2004.

[76] J-M Shi, D Gerlach, M Breuer, G Biswas, and F Durst. Heating effect on steady and unsteady horizontal laminar flow of air past a circular cylinder. *Physics of Fluids (1994-present)*, 16(12):4331–4345, 2004.

[77] Yan Ji, Kun Yuan, and JN Chung. Numerical simulation of wall roughness on gaseous flow and heat transfer in a microchannel. *International Journal of Heat and Mass Transfer*, 49(7):1329–1339, 2006.

[78] Gabriel Gamrat, Michel Favre-Marinet, and S Le Person. Modelling of roughness effects on heat transfer in thermally fully-developed laminar flows through microchannels. *International Journal of Thermal Sciences*, 48(12):2203–2214, 2009.

[79] Yongping Chen, Panpan Fu, Chengbin Zhang, and Mingheng Shi. Numerical simulation of laminar heat transfer in microchannels with rough surfaces characterized by fractal cantor structures. *International Journal of Heat and Fluid Flow*, 31(4):622–629, 2010.

[80] Chengbin Zhang, Yongping Chen, and Mingheng Shi. Effects of roughness elements on laminar flow and heat transfer in microchannels. *Chemical Engineering and Processing: Process Intensification*, 49(11):1188–1192, 2010.

[81] Bassam A/K Abu-Hijleh. Numerical simulation of forced convection heat transfer from a cylinder with high conductivity radial fins in cross-flow. *International journal of thermal sciences*, 42(8):741–748, 2003.

[82] J Koo and C Kleinstreuer. Analysis of surface roughness effects on heat transfer in micro-conduits. *International Journal of Heat and Mass Transfer*, 48(13):2625–2634, 2005.

[83] S Bhattacharyya and AK Singh. Augmentation of heat transfer from a solid cylinder wrapped with a porous layer. *International Journal of Heat and Mass Transfer*, 52(7):1991–2001, 2009.

[84] SW Churchill and M Bernstein. A correlating equation for forced convection from gases and liquids to a circular cylinder in crossflow. *Journal of Heat Transfer*, 99(2):300–306, 1977.

[85] Vincent T Morgan. The overall convective heat transfer from smooth circular cylinders. *Advances in heat transfer*, 11:199–264, 1975.

[86] Ephraim M Sparrow, John P Abraham, and Jimmy CK Tong. Archival correlations for average heat transfer coefficients for non-circular and circular

cylinders and for spheres in cross-flow. *International Journal of Heat and Mass Transfer*, 47(24):5285–5296, 2004.

[87] Waqar Khan. Modeling of fluid flow and heat transfer for optimization of pin-fin heat sinks. 2004.

[88] Stephen Whitaker. Forced convection heat transfer correlations for flow in pipes, past flat plates, single cylinders, single spheres, and for flow in packed beds and tube bundles. *AIChE Journal*, 18(2):361–371, 1972.

[89] HC Perkins and G Leppert. Local heat-transfer coefficients on a uniformly heated cylinder. *International journal of heat and mass transfer*, 7(2):143–158, 1964.

[90] TS Sarma and SP Sukhatme. Local heat transfer from a horizontal cylinder to air in cross flow: influence of free convection and free stream turbulence. *International Journal of Heat and Mass Transfer*, 20(1):51–56, 1977.

[91] Nils Frossling. Evaporation, heat transfer, and velocity distribution in two-dimensional and rotationally symmetrical laminar boundary-layer flow. Technical report, DTIC Document, 1956.

[92] Elmar Achenbach. Total and local heat transfer from a smooth circular cylinder in cross-flow at high Reynolds number. *International Journal of Heat and Mass Transfer*, 18(12):1387–1396, 1975.

[93] Stavros Tavoularis. *Measurement in fluid mechanics*. Cambridge University Press, 2005.

[94] Invotec extera, Innovative Products For The Injection Moulder. `http://www.invotecextra.co.uk/temperature-control/invotec-cartridge-heaters/10mm-metric-cartridge-heaters.html`. Accessed: 2017-12-20.

[95] RdF, HFS-A Heat Flux Sensorsc. `http://www.rdfcorp.com/products/hflux/ hflux.shtml`. Accessed: 2017-12-20.

[96] DJ Ortolano and FF Hines. Simplified approach to heat flow measurement. *Proceedings of the ISA International Conference, Houston.*, 38(2):1449–1456, 1983.

[97] John G Webster. *Mechanical Variables Measurement-Solid, Fluid, and Thermal*. CRC Press, 1999.

[98] Clayton A Pullins. *High temperature heat flux measurement: sensor design, calibration, and applications*. PhD thesis, Virginia Polytechnic Institute and State University, 2011.

[99] DC Shallcross and DG Wood. The accurate measurement of heat flux using thin film heat flux sensors with application to petroleum engineering. Technical report, Stanford Univ., CA (USA). Petroleum Research Inst., 1990.

[100] A Kondjoyan and JD Daudin. Effects of free stream turbulence intensity on heat and mass transfers at the surface of a circular cylinder and an elliptical cylinder, axis ratio 4. *International Journal of Heat and Mass Transfer*, 38(10):1735–1749, 1995.

[101] Rui Liu, David SK Ting, and Gary W Rankin. On the generation of turbulence with a perforated plate. *Experimental thermal and fluid science*, 28(4):307–316, 2004.

[102] IPD De Silva and HJS Fernando. Oscillating grids as a source of nearly isotropic turbulence. *Physics of Fluids (1994-present)*, 6(7):2455–2464, 1994.

[103] L Ljungkrona, CH Norberg, and B Sunden. Free-stream turbulence and tube spacing effects on surface pressure fluctuations for two tubes in an in-line arrangement. *Journal of Fluids and Structures*, 5(6):701–727, 1991.

[104] Sudhir D Savkar. Buffeting force on rigid circular cylinders in cross flows. *Journal of Fluid Mechanics*, 105:397–425, 1981.

[105] Genevieve Comte-Bellot. Hot-wire anemometry. *Annual review of fluid mechanics*, 8(1):209–231, 1976.

[106] MK Swaminathan, R Bacic, GW Rankin, and K Sridhar. Improved calibration of hot-wire anemometers. *Journal of Physics E: Scientific Instruments*, 16(4):335, 1983.

[107] HH Bruun and C Tropea. The calibration of inclined hot-wire probes. *Journal of Physics E: Scientific Instruments*, 18(5):405, 1985.

[108] Louis Vessot King. On the convection of heat from small cylinders in a stream of fluid: determination of the convection constants of small platinum wires with applications to hot-wire anemometry. *Philosophical Transactions of the Royal Society of London. Series A, Containing Papers of a Mathematical or Physical Character*, 214:373–432, 1914.

[109] Hans H Bruun. *Hot-wire anemometry-principles and signal analysis*. Oxford science publications, 1995.

[110] William K George, Paul D Beuther, and Aamir Shabbir. Polynomial calibrations for hot wires in thermally varying flows. *Experimental Thermal and Fluid Science*, 2(2):230–235, 1989.

[111] H Deyhle and H Bippes. Disturbance growth in an unstable three-dimensional boundary layer and its dependence on environmental conditions. *Journal of Fluid Mechanics*, 316:73–113, 1996.

[112] Olajide Ganiyu Akinlade. *Effects of surface roughness on the flow characteristics in a turbulent boundary layer*. PhD thesis, University of Saskatchewan, 2005.

[113] Ashwin Vinod, Amshumaan Kashyap, Arindam Banerjee, and Jonathan Kimball. Augmenting energy extraction from vortex induced vibration using strips of roughness/thickness combinations. In *Int. J. Marine Energy technology Symposium*, 2013.

[114] EE Essel. *Experimental Study of Roughness Effect on Turbulent Shear Flow Downstream of a Backward Facing Step*. PhD thesis, The University of Manitoba, 2014.

[115] Luiz Alberto Franco and Amilton Sinatora. 3D surface parameters (ISO 25178-2): Actual meaning of S pk and its relationship to V mp. *Precision Engineering*, 40:106–111, 2015.

[116] Karen A Flack and Michael P Schultz. Review of hydraulic roughness scales in the fully rough regime. *Journal of Fluids Engineering*, 132(4):041203, 2010.

[117] R Deltombe, KJ Kubiak, and M Bigerelle. How to select the most relevant 3D roughness parameters of a surface. *Scanning*, 36(1):150–160, 2014.

[118] Geometrical product specifications (GPS) - surface texture: Areal, Part 1: Terms, definitions and surface texture parameters, apr 2012.

[119] BK Rao. Heat transfer to non-Newtonian flows over a cylinder in cross flow. *International journal of heat and fluid flow*, 21(6):693–700, 2000.

[120] Joon Sik Lee, Dong Kee Sohn, and Tae Hwan Lee. Simultaneous effects of free-stream trubulence intensity and integral length scale on mass transfer about cylinder. *Experimental thermal and fluid science*, 9(2):225–232, 1994.

[121] E Achenbach. Heat-transfer from a staggered tube bundle in cross-flow at high Reynolds-numbers. *Int. J. Heat Mass Transfer*, 32(2):271–280, 1989.

[122] C Norberg. An experimental investigation of the flow around a circular cylinder: influence of aspect ratio. *Journal of Fluid Mechanics*, 258:287–316, 1994.

[123] C Norberg. Interaction between freestream turbulence and vortex shedding for a single tube in cross-flow. *Journal of wind engineering and industrial aerodynamics*, 23:501–514, 1986.

[124] T Nagaraju, Satish C Sharma, and SC Jain. Influence of surface roughness on non-newtonian thermohydrostatic performance of a hole-entry hybrid journal bearing. *Journal of Tribology*, 129(3):595–602, 2007.

[125] Ezio Mancaruso, Luigi Sequino, and Bianca Maria Vaglieco. IR imaging of premixed combustion in a transparent Euro5 diesel engine. Technical report, SAE Technical Paper, 2011.

[126] Eliodoro Chiavazzo, Luigi Ventola, Flaviana Calignano, Diego Manfredi, and Pietro Asinari. A sensor for direct measurement of small convective heat fluxes: Validation and application to micro-structured surfaces. *Experimental Thermal and Fluid Science*, 55:42–53, 2014.

[127] T Astarita, G Cardone, GM Carlomagno, and C Meola. A survey on infrared thermography for convective heat transfer measurements. *Optics & Laser Technology*, 32(7):593–610, 2000.

[128] Mitja Mori, Lovrenc Novak, and Mihael Sekavčnik. Measurements on rotating blades using IR thermography. *Experimental Thermal and Fluid Science*, 32(2):387–396, 2007.

[129] Herchang Ay, JiinYuh Jang, and Jer-Nan Yeh. Local heat transfer measurements of plate finned-tube heat exchangers by infrared thermography. *International Journal of Heat and Mass Transfer*, 45(20):4069–4078, 2002.

[130] Sergio Marinetti and Pier Giorgio Cesaratto. Emissivity estimation for accurate quantitative thermography. *NDT & E International*, 51:127–134, 2012.

[131] ISO. Optics and Photonics - Spectral Bands. Standard ISO 20473:2007(E), International Organization for Standardization, 2007.

[132] Chang-Da Wen and Issam Mudawar. Emissivity characteristics of polished aluminum alloy surfaces and assessment of multispectral radiation thermometry (MRT) emissivity models. *International journal of heat and mass transfer*, 48(7):1316–1329, 2005.

[133] Chang-Da Wen and Issam Mudawar. Emissivity characteristics of roughened aluminum alloy surfaces and assessment of multispectral radiation thermometry (MRT) emissivity models. *International Journal of Heat and Mass Transfer*, 47(17):3591–3605, 2004.

[134] J.P. Holman. *Heat Transfer (10th ed)*. Mcgraw-Hill Companies, 2010.

[135] T Astarita, G Cardone, and GM Carlomagno. Infrared thermography: An optical method in heat transfer and fluid flow visualisation. *Optics and lasers in engineering*, 44(3):261–281, 2006.

[136] Mohd Shawal Jadin and Soib Taib. Recent progress in diagnosing the reliability of electrical equipment by using infrared thermography. *Infrared Physics & Technology*, 55(4):236–245, 2012.

[137] Yang Cao, Xiaoming Gu, and Qi Jin. Infrared technology in the fault diagnosis of substation equipment. In *Electricity Distribution, 2008. CICED 2008. China International Conference on*, pages 1–6. IEEE, 2008.

[138] C Badulescu, M Grédiac, H Haddadi, J-D Mathias, X Balandraud, and H-S Tran. Applying the grid method and infrared thermography to investigate plastic deformation in aluminium multicrystal. *Mechanics of Materials*, 43(1):36–53, 2011.

[139] Minh Phong Luong. Fatigue limit evaluation of metals using an infrared thermographic technique. *Mechanics of materials*, 28(1):155–163, 1998.

[140] ML Pastor, X Balandraud, M Grédiac, and JL Robert. Applying infrared thermography to study the heating of 2024-T3 aluminium specimens under fatigue loading. *Infrared Physics & Technology*, 51(6):505–515, 2008.

[141] L Jiang, H Wang, PK Liaw, CR Brooks, and DL Klarstrom. Characterization of the temperature evolution during high-cycle fatigue of the ULTIMET superalloy: experiment and theoretical modeling. *Metallurgical and Materials Transactions A*, 32(9):2279–2296, 2001.

[142] MR Clark, DM McCann, and MC Forde. Application of infrared thermography to the non-destructive testing of concrete and masonry bridges. *Ndt & E International*, 36(4):265–275, 2003.

[143] E Grinzato, C Bressan, S Marinetti, PG Bison, and C Bonacina. Monitoring of the Scrovegni Chapel by IR thermography: Giotto at infrared. *Infrared Physics & Technology*, 43(3):165–169, 2002.

[144] Carosena Meola. Infrared thermography of masonry structures. *Infrared physics & technology*, 49(3):228–233, 2007.

[145] Jalaj Kumar, Sony Baby, and Vikas Kumar. Thermographic studies on IMI-834 titanium alloy during tensile loading. *Materials Science and Engineering: A*, 496(1):303–307, 2008.

[146] Hakim Ait-Amokhtar, Claude Fressengeas, and S Boudrahem. The dynamics of Portevin–Le Chatelier bands in an Al–Mg alloy from infrared thermography. *Materials Science and Engineering: A*, 488(1):540–546, 2008.

[147] S Bagavathiappan, BB Lahiri, T Saravanan, John Philip, and T Jayakumar. Infrared thermography for condition monitoring–a review. *Infrared Physics & Technology*, 60:35–55, 2013.

[148] Patrik Broberg. Surface crack detection in welds using thermography. *NDT & E International*, 57:69–73, 2013.

[149] Julien Artozoul, Christophe Lescalier, Olivier Bomont, and Daniel Dudzinski. Extended infrared thermography applied to orthogonal cutting: Mechanical and thermal aspects. *Applied Thermal Engineering*, 64(1):441–452, 2014.

[150] M Armendia, A Garay, A Villar, MA Davies, and PJ Arrazola. High bandwidth temperature measurement in interrupted cutting of difficult to machine materials. *CIRP Annals-Manufacturing Technology*, 59(1):97–100, 2010.

[151] J Pujana, A Rivero, A Celaya, and LN Lopez de Lacalle. Analysis of ultrasonic-assisted drilling of Ti6Al4V. *International Journal of Machine Tools and Manufacture*, 49(6):500–508, 2009.

[152] Umberto Desideri, Gianluca Rossi, Alessandro Giovannozzi, and Paolo Maggiorana. High resolution infrared thermography for airfoils boundary layer inspection in passive mode. In *ASME Turbo Expo 2004: Power for Land, Sea, and Air*, pages 579–583. American Society of Mechanical Engineers, 2004.

[153] Giovanni Maria Carlomagno and Gennaro Cardone. Infrared thermography for convective heat transfer measurements. *Experiments in fluids*, 49(6):1187–1218, 2010.

[154] A Schulz. Infrared thermography as applied to film cooling of gas turbine components. *Measurement Science and Technology*, 11(7):948, 2000.

[155] Ld Luca, GM Carlomagno, and G Buresti. Boundary layer diagnostics by means of an infrared scanning radiometer. *Experiments in fluids*, 9(3):121–128, 1990.

[156] Simone Zuccher and William S Saric. Infrared thermography investigations in transitional supersonic boundary layers. *Experiments in Fluids*, 44(1):145–157, 2008.

[157] Michael Gritsch, Achmed Schulz, and Sigmar Wittig. Film-cooling holes with expanded exits: near-hole heat transfer coefficients. *International Journal of Heat and Fluid Flow*, 21(2):146–155, 2000.

[158] Srinath V Ekkad, Shichuan Ou, and Richard B Rivir. A transient infrared thermography method for simultaneous film cooling effectiveness and heat transfer coefficient measurements from a single test. In *ASME Turbo Expo 2004: Power for Land, Sea, and Air*, pages 999–1005. American Society of Mechanical Engineers, 2004.

[159] Chang-Da Wen and Issam Mudawar. Experimental investigation of emissivity of aluminum alloys and temperature determination using multispectral

radiation thermometry (MRT) algorithms. *Journal of materials engineering and performance*, 11(5):551–562, 2002.

[160] Chang-Da Wen and Issam Mudawar. Modeling the effects of surface roughness on the emissivity of aluminum alloys. *International Journal of Heat and Mass Transfer*, 49(23):4279–4289, 2006.

[161] Michal Wieczorowski and Leszek Rozanski. Roughness aspects in thermal analysis of machine tools. In *XVIII IMEKO World Congress, Metrology for a Sustainable Development, Rio de Janeiro, Brazil, Proc*, pages 17–22, 2006.

[162] WA Khan, JR Culham, and MM Yovanovich. Fluid flow around and heat transfer from an infinite circular cylinder. *Journal of Heat transfer*, 127(7):785–790, 2005.

[163] Karl Pohlhausen. Zur näherungsweisen integration der differentialgleichung der iaminaren grenzschicht. *ZAMM-Journal of Applied Mathematics and Mechanics/Zeitschrift für Angewandte Mathematik und Mechanik*, 1(4):252–290, 1921.

[164] Herrmann Schlichting and Klaus Gersten. *Boundary-Layer Theory*. Springer Science & Business Media, 2003.

[165] PE Roach. The generation of nearly isotropic turbulence by means of grids. *International Journal of Heat and Fluid Flow*, 8(2):82–92, 1987.

[166] Lamyaa A El-Gabry, Douglas R Thurman, and Philip E Poinsatte. Procedure for determining turbulence length scales using hotwire anemometry. 2014.

[167] *Infrared (*IR*) Material Windows*. 101 East Gloucester Pike, Barrington, NJ 08007-1380 USA. Accessed: 2017-12-20.

APPENDIX A

A two-dimensional boundary layer analysis

Using the curvilinear system of coordinates, as shown in Figure A.1, for laminar and incompressible flow field, the equations (2.5),(2.6), and (2.7), leads to the following system of equations [162]:

Continuity:

$$\frac{\partial u}{\partial s} + \frac{\partial v}{\partial \eta} = 0 \tag{A.1}$$

Momentum:

s-direction:

$$u\frac{\partial u}{\partial s} + v\frac{\partial u}{\partial \eta} = -\frac{1}{\rho}\frac{dP}{ds} + v\frac{\partial^2 u}{\partial \eta^2} \tag{A.2}$$

η-direction:

$$\frac{dP}{\partial \eta} = 0 \tag{A.3}$$

Bernoulli equation:

$$-\frac{1}{\rho}\frac{dP}{ds} = U(o)\frac{dU(o)}{ds} \tag{A.4}$$

Energy:

$$\frac{1}{\alpha}\Big(u\frac{\partial T}{\partial s} + v\frac{\partial T}{\partial \eta}\Big) = \frac{\partial^2 T}{\partial \eta^2} \tag{A.5}$$

As shown in Figure A.1, for a uniform flow field, (T_∞) denoted to the ambient temperature and the approaching velocity of the flow is assumed to be U_∞ . In the isothermal condition, the surface temperature of the wall (T_w) is higher than the ambient temperature (T_∞) while in the iso-flux boundary case, the heat flux is q. The velocity distribution of fluid outside the boundary layer, across a cylinder is represented by $U(o)$, Equation.(2.2).

Boundary Conditions:

Hydrodynamic:

At the surface of cylinder, where $\eta = 0$

$$u = 0 \quad and \quad \frac{\partial^2 u}{\partial \eta^2} = \frac{1}{\mu}\frac{\partial P}{\partial s} \tag{A.6}$$

At the boundary layer edge , where $\eta = \delta(o)$

$$u = U(o) \quad and \quad \frac{\partial u}{\partial \eta} = 0 \quad and \quad \frac{\partial^2 u}{\partial \eta^2} = 0 \tag{A.7}$$

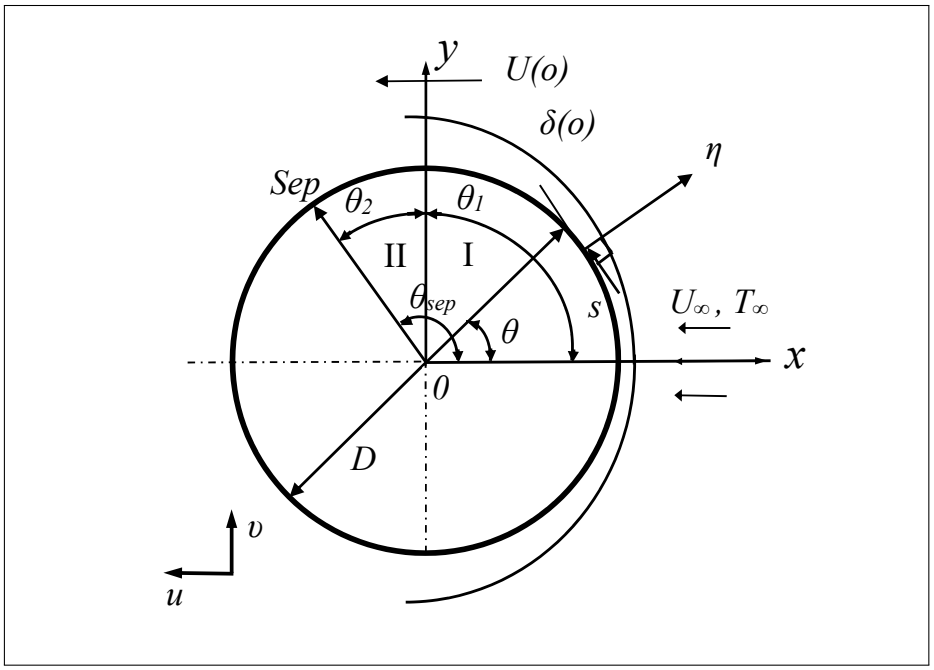

Figure A.1: Flow across a circular cylinder [162].

Thermal:

The cases of thermal boundary layer for the uniform wall temperature and uniform wall flux can be written as follows:

$$\eta = 0, \quad \begin{cases} T = T_w & \text{for the isothermal boundary condition} \\ \frac{\partial T}{\partial \eta} = -\frac{q}{k_f} & \text{or the isoflux boundary condition} \end{cases} \tag{A.8}$$

$$\eta = \delta_T, \quad and \quad T = T_\infty \quad and \quad \frac{\partial T}{\partial \eta} = 0 \tag{A.9}$$

Velocity and temperature distribution.

Velocity distribution

Using Pohlhausen's suggestion [163] who proposed a fourth order polynomial equation to describe the velocity profiles in the boundary layer around the cylinder as:

$$\frac{u}{U(o)} = (2\eta_H - 2\eta_H^3 + \eta_H^4) + \frac{\omega}{6}(\eta_H - 3\eta_H^2 + 3\eta_H^3 - \eta_H^4) \tag{A.10}$$

where $0 \leqslant \eta_H = \eta/\delta(o) \leqslant 1$ and ω is the pressure gradient parameter, given by

$$\omega = \frac{\delta^2}{v}\frac{dU(o)}{ds} \tag{A.11}$$

Schlichting [164] suggested to restricted ω to the range $-12 \leqslant \omega \leqslant 12$.

Temperature Distribution

By Assuming that the thermal boundary layer around the cylinder is thin, so a third order polynomial equation can be used to describe the temperature profiles in the thermal boundary layer around the cylinder, as following:

$$\frac{T - T_\infty}{T_w - T_\infty} = 1 - \frac{3}{2}\eta_T + \frac{1}{2}\eta_T^3 \qquad \text{for uniform wall temperature} \tag{A.12}$$

$$T - T_\infty = \frac{2q\delta_T}{3k_f}\left(1 - \frac{3}{2}\eta_T + \frac{1}{2}\eta_T^3\right) \qquad \text{for uniform wall flux} \tag{A.13}$$

Boundary layer characteristics

The momentum equation, can be written in the following dimensionless form:

$$\frac{U\delta_2}{v}\frac{d\delta_2}{ds} + \left(2 + \frac{\delta_1}{\delta_2}\right)\frac{\delta_2^2}{v}\frac{dU}{ds} = \frac{\delta_2}{U}\left.\frac{\partial u}{\partial \eta}\right|_{\eta=0} \tag{A.14}$$

where δ_1 and δ_2 are the displacement and momentum boundary layer thicknesses.

By solving the equation (A.14), Khan [87] got the local dimensionless boundary layer and momentum thicknesses:

$$\frac{\delta}{D} = \frac{0.5}{\sqrt{Re_D}}\sqrt{\frac{\omega}{\cos\theta}} \tag{A.15}$$

$$\frac{\delta_2}{D} = \frac{0.3428}{\sqrt{Re_D}}\sqrt{\frac{1}{\sin^6\theta}\int_0^\theta \sin^5\zeta\, d\zeta} \tag{A.16}$$

where Re_D is the Reynolds number, defined as

$$Re_D = \frac{U_\infty D}{v} \tag{A.17}$$

The values of pressure gradient parameter (ω) are obtained corresponding to each position along the cylinder surface.

Fluid flow

The most interest of fluid friction parameters is the drag force F_D, which is the sum of the pressure drag D_p and skin friction drag D_f. Pressure drag is due to the unbalanced pressures on both sides of the cylinder, where the relatively lower pressures on the downstream surfaces and high pressures on the upstream surfaces, it can be written in the following dimensionless form:

$$C_{Dp} = \int_0^{\pi} C_p \cos\theta d\theta \tag{A.18}$$

where C_p is the pressure coefficient and can be defined as following:

$$C_p = \frac{\Delta P}{\frac{1}{2}\rho U_\infty^2} \tag{A.19}$$

By integrating momentum equation with respect to θ, the pressure difference ΔP can be obtained as following:

$$\frac{\Delta P}{\frac{1}{2}\rho U_\infty^2} = 2(1-\cos\theta) + \frac{8}{Re_D}(1-\cos\theta) \tag{A.20}$$

So, the pressure drag coefficient for the cylinder up to the separation point will be

$$C_{Dp} = \int_0^{\theta_{sep}} C_p \cos\theta d\theta = 1.152 + \frac{1.26}{Re_D} \tag{A.21}$$

Because of viscous shear forces, skin friction drag is produced at the cylinder surface, Especially, at the attached boundary layer regions, it can be written in the following dimensionless form:

$$C_f = \frac{\tau_w}{\frac{1}{2}\rho U_\infty^2} = \frac{4}{3}\frac{\omega+12}{\sqrt{Re_D}}\sin\theta\sqrt{\frac{\cos\theta}{\omega}} \tag{A.22}$$

The friction drag coefficient can be defined as:

$$C_{Df} = \int_0^{\pi} C_f \sin\theta d\theta = \int_0^{\theta_{sep}} C_f \sin\theta d\theta + \int_{\theta_{sep}}^{\pi} C_f \sin\theta d\theta \tag{A.23}$$

After boundary layer separation, the shear stress is negligible, so the second integral will be zero and the equation (A.23) can be written as follows:

$$C_{Df} = \int_0^{\theta_{sep}} C_f \sin\theta d\theta = \frac{5.786}{\sqrt{Re_D}} \tag{A.24}$$

By collecting of both parts of drag coefficient C_D, the overall drag coefficient can be written as:

$$C_D = \frac{5.786}{\sqrt{Re_D}} + 1.152 + \frac{1.26}{Re_D} \tag{A.25}$$

Heat transfer

The dimensionless average heat transfer coefficient (Nu_D), is determined by limited integration for energy equation (A.5), from the cylinder surface to the thermal boundary layer edge. By assuming that a thin thermal boundary layer along the cylinder surface, the energy equation (A.5) for the isothermal boundary condition can be written as follows:

$$\frac{d}{ds}\int_0^{\delta_T} (T - T_\infty) u d\eta = -\alpha \frac{\partial T}{\partial \eta}\bigg|_{\eta=0} \tag{A.26}$$

Using velocity and temperature distribution equation (A.10) and (A.12), and assuming $\zeta = \delta_T/\delta$, equation (A.26) can be simplified to

$$\delta_T \frac{d}{ds}[U(o)\delta_T \zeta(\omega + 12)] = 90\alpha \tag{A.27}$$

This equation can be rewritten separately for the two regions, As shown in Figure A.1.

$$\delta_T \frac{d}{ds}[U(o)\delta_T \zeta(\omega_1 + 12)] = 90\alpha \qquad \text{For rigion I} \tag{A.28}$$

and

$$\delta_T \frac{d}{ds}[U(m)\delta_T \zeta(\omega_2 + 12)] = 90\alpha \qquad \text{For rigion II} \tag{A.29}$$

Local thermal boundary layer thicknesses can be obtained by integrating Equation A.28 and A.29, in the respective regions, with respect to s.

$$\left(\frac{\delta_T(\theta)}{D}\right).Re_D^{\frac{1}{2}} Pr^{\frac{1}{3}} = \begin{cases} \sqrt[3]{\frac{45 f_1(\theta)}{2(\omega_1+12)^2 \sin^2\theta}\sqrt{\frac{\omega_1}{\cos\theta}}} & \text{For rigion I} \\ \sqrt[3]{\frac{45 f_3(\theta)}{2\sin^2\theta}\sqrt{\frac{\omega_2}{\cos\theta}}} & \text{For rigion II} \end{cases} \tag{A.30}$$

where the functions $f_1(\theta)$ and $f_3(\theta)$ are given by

$$f_1(\theta) = \int_0^{\theta} \sin\theta(\omega_1 + 12)d\theta \tag{A.31}$$

and

$$f_3(\theta) = \frac{f_1(\theta)}{\omega_1 + 12} + \frac{f_2(\theta)}{\omega_2 + 12} \tag{A.32}$$

with

$$f_2(\theta) = \int_{\theta_1}^{\theta_{sep}} \sin\theta(\omega_2 + 12)d\theta \tag{A.33}$$

For the isothermal boundary condition, the local heat transfer coefficients, in both the regions can be written as follows:

$$h_1(\theta) = \frac{3k_f}{2\delta_{T_1}} \quad and \quad h_2(\theta) = \frac{3k_f}{2\delta_{T_2}} \tag{A.34}$$

Thus the dimensionless local heat transfer coefficients, for both the regions, can be written as

$$\frac{Nu_D(\theta)|_{isothermal}}{Re_D^{\frac{1}{2}} Pr^{\frac{1}{3}}} = \begin{cases} \frac{3}{2}\sqrt[3]{\frac{2(\omega_1+12)^2\sin^2\theta}{45f_1(\theta)}\sqrt{\frac{\cos\theta}{\omega_1}}} & \text{For rigion I} \\ \frac{3}{2}\sqrt[3]{\frac{2\sin^2\theta}{45f_3(\theta)}\sqrt{\frac{\cos\theta}{\omega_2}}} & \text{For rigion II} \end{cases} \tag{A.35}$$

The average heat transfer coefficient is defined as:

$$h = \frac{1}{\pi}\int_0^{\pi} h(\theta)d\theta = \frac{1}{\pi}\left\{\int_o^{\theta_{sep}} h(\theta)d\theta + \int_{\theta_{sep}}^{\pi} h(\theta)d\theta\right\} \tag{A.36}$$

The integral analysis is unable to predict heat transfer values for the second term of equation (A.36). However, the experiments' data [2, 4, 5] show that the heat transfer from separation point to the rear stagnation point increases with Reynolds numbers. Also, Zijnen [6] demonstrated that the heat transferred from this region can be determined from $Nu_D = 0.001Re_D$. The share of heat transfer from the rear portion of the cylinder can be included by integrated the local heat transfer coefficients to the separation point and averaged over the whole surface, as follows:

$$h = \frac{1}{\pi}\int_0^{\theta_{sep}} h(\theta)d\theta = \frac{1}{\pi}\left\{\int_o^{\theta_1} h_1(\theta)d\theta + \int_{\theta_1}^{\theta_{sep}} h_2(\theta)d\theta\right\} \tag{A.37}$$

Using equations (A.30)- (A.34), equation (A.37) can be solved for the average heat transfer coefficient which gives the average Nusselt number for an isothermal cylinder as

$$Nu_D|_{isothermal} = 0.593 Re_D^{\frac{1}{2}} Pr^{\frac{1}{3}} \tag{A.38}$$

For the iso-flux boundary case, the energy equation can be written as follows:

$$\frac{d}{ds}\int_0^{\delta_T} (T - T_\infty) u d\eta = \frac{q}{\rho c_p} \tag{A.39}$$

By assuming that constant heat flux and thermophysical properties, equation (A.39) can be rewritten as:

$$\frac{d}{ds}[U(o)\delta_T^2 \zeta(\omega + 12)] = 90\frac{v}{Pr} \tag{A.40}$$

This equation can be rewritten separately for the two regions in the same way as equation (A.27). Local thermal boundary layer thicknesses δ_{T_1} and δ_{T_2} can be obtained under iso-flux boundary condition. The local surface temperatures for the two regions can then be obtained from temperature distribution

$$\Delta T_1(\theta) = \frac{2q\delta_{T_1}}{3k_f} \tag{A.41}$$

and

$$\Delta T_2(\theta) = \frac{2q\delta_{T_2}}{3k_f} \tag{A.42}$$

The local heat transfer coefficient can now be obtained from its definition as follows:

$$h_1(\theta) = \frac{q}{\Delta T_1(\theta)} \quad and \quad h_2(\theta) = \frac{q}{\Delta T_2(\theta)} \tag{A.43}$$

which give the local Nusselt numbers at constant heat flux condition.

$$\frac{Nu_D(\theta)|_{isoflux}}{Re_D^{\frac{1}{2}}Pr^{\frac{1}{3}}} = \begin{cases} \frac{3}{2}\sqrt[3]{\frac{4(\omega_1+12)\sin\theta}{45f_4(\theta)}\sqrt{\frac{\cos\theta}{\omega_1}}} & \text{For rigion I} \\ \frac{3}{2}\sqrt[3]{\frac{4\sin\theta}{45f_6(\theta)}\sqrt{\frac{\cos\theta}{\omega_2}}} & \text{For rigion II} \end{cases} \tag{A.44}$$

By following the same procedure for an isothermal cylinder as mentioned above, the average Nusselt number for an iso-flux cylinder can be obtained as :

$$Nu_D|_{isoflux} = 0.632Re_D^{\frac{1}{2}}Pr^{\frac{1}{3}} \tag{A.45}$$

By comparing the results for both thermal boundary conditions, The average Nu number at the iso-flux cylinder is about 6% higher than an isothermal cylinder.

$$\frac{Nu_D}{Re_D^{\frac{1}{2}}Pr^{\frac{1}{3}}} = \begin{cases} 0.593 & \text{for an isothermal cylinder} \\ 0.632 & \text{For an iso-flux cylinder} \end{cases} \tag{A.46}$$

APPENDIX B

Characterizing Turbulence

Turbulent vortices generate oscillations in velocity, the vertical (v) and longitudinal (u). Both velocities change with time because of turbulent fluctuations, figure B.1.In laminar and steady flow, $v = \bar{v}$ and $u = \bar{u}$ for all time t, where the over-bar means a time average. If the flow were unsteady and turbulent then the velocity contains both a turbulent and a mean component, the flow is expressed as following.

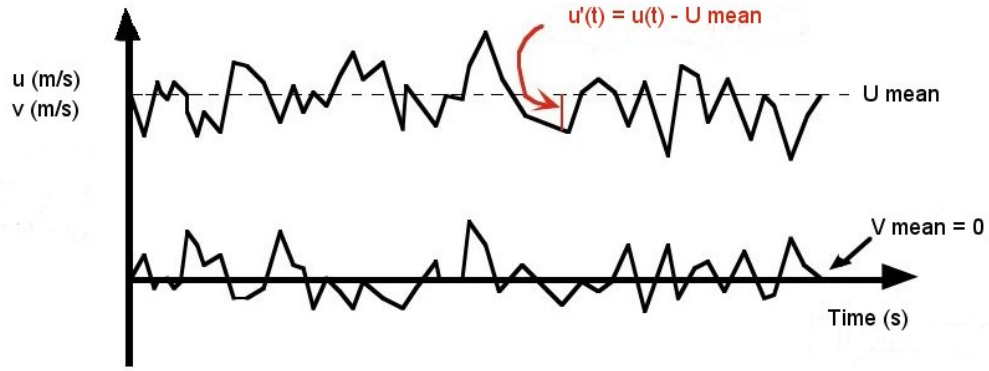

Figure B.1: Mean and a Turbulent Velocity Component

$$u(t) = U_{mean} + u'(t) \tag{B.1}$$

$$v(t) = V_{mean} + v'(t) \tag{B.2}$$

In following, an over-bar is used to indicate a time average over long time interval (from t to t+T), where T is longer than any turbulence time scale, and shorter than the time-scale for wave fluctuation.

Mean velocity:

$$U_{mean} = \int_{t}^{t+T} \mathrm{u(t)}\,\mathrm{d}t \tag{B.3}$$

Turbulent Fluctuation:

$$u'(t) = u(t) - U_{mean} \tag{B.4}$$

Turbulence Strength:

$$\bar{u} = \sqrt{\overline{u'(t)^2}} \tag{B.5}$$

Turbulence Intensity:

$$T_u = \frac{\bar{u}}{U_{mean}} \tag{B.6}$$

Turbulence Length Scales

During test rig operation, the hot wire anemometer voltages were collected and converted to velocity by using Labview software and by depending on the calibration curve. Figure B.2 shows an example of the velocity trace for plate No. 5. The mean velocity U_{mean} is about 15 m/s and turbulence strength of the velocity $\bar{u}$ is 0.77 m/s. thus the turbulence intensity is $Tu = 5.2\%$.

To transfer the data from the time domain to the frequency domain a fast Fourier transformation (FFT) was used. The Matlab software package was used for that purpose. The next section contains the Matlab script. The sampling frequency is 200 kHz for 5 sec, i.e. the U array (the velocity trace) consist of $1x10^6$ points.Figure B.3 is shown the amplitude spectrum of the velocity. The velocity in the frequency domain (aFData) is the fast Fourier transformation of the velocity, and (L) is the length of the signal.

$$aFData = fft(U)$$
$$L = length(aFData)$$

To determine the energy $E(f)$, power spectra of velocity has been divided by signal frequency, where power is known as:

$$Power = abs(fft(U)).^2/L$$

The energy density spectrum is shown in Figure B.4.

The integral length scale, (Lx) is used to measure of the largest eddy size in turbulent flow, the method that is described in [165, 166] was used in the calculations.

$$L_x = \left[\frac{E(f)U_{mean}}{4\bar{u}^2}\right]_{f\longrightarrow 0}$$

Where $\bar{u}$ is the turbulence strength of the velocity (standard deviation), while $E(f)$ is equal averaged of first hundred points of frequency when frequency approaches zero value (at the low frequencies). In this example, $E(f)$ is determined to be $1.8x10^{-3}$ as f approaches zero, and thus the length scale (Lx) is calculated to be:

$$L_x = \frac{\left(1.8x10^{-3}\frac{m^2}{s}\right)\left(14.96\frac{m}{s}\right)}{4\left(0.772^2\frac{m^2}{s^2}\right)} = 0.0111m = 11.1mm$$

The dissipation length scale, λ_x, is a measure of the average dimension of the eddies responsible for the turbulent energy dissipation.

$$\frac{1}{\lambda_x^2} = \frac{2\pi^2}{U^2\overline{u^2}}\int_0^\infty f^2.E(f).df$$

The trapezoid rule is used for the numerical integration; the integration yields $4.1733x10^6 m^2/s^4$

$$\frac{1}{\lambda_x^2} = \frac{2\pi^2}{\left(14.96^2 \frac{m^2}{s^2}\right)\left(0.772^2 \frac{m^2}{s^2}\right)}\left[4.1733x10^6 \frac{m^2}{s^4}\right] = 9.12x10^5 \frac{1}{m^2}$$

$$\lambda_x = 0.0013m$$

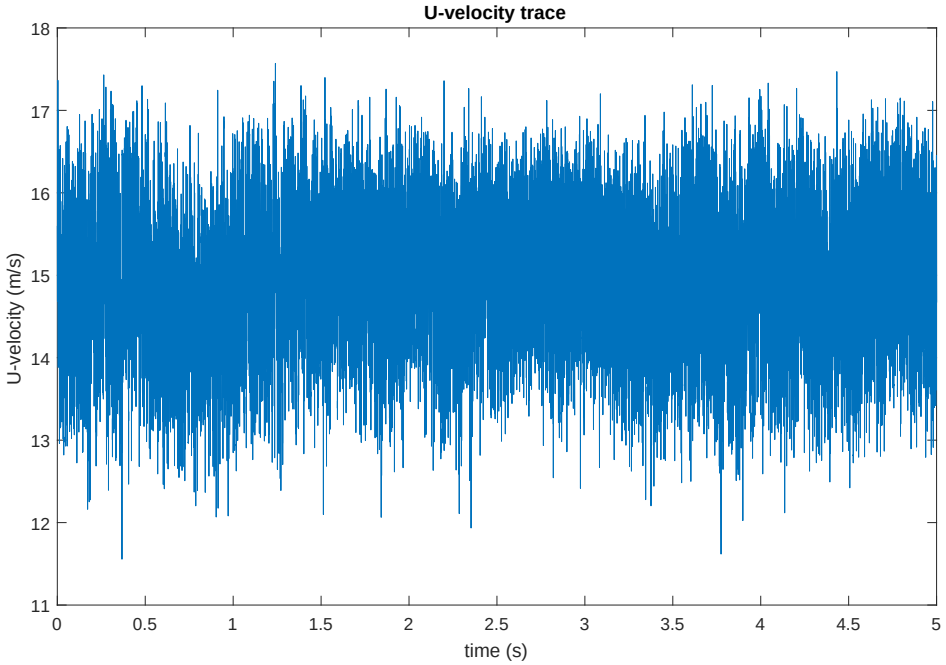

Figure B.2: The velocity trace for plate No. 5

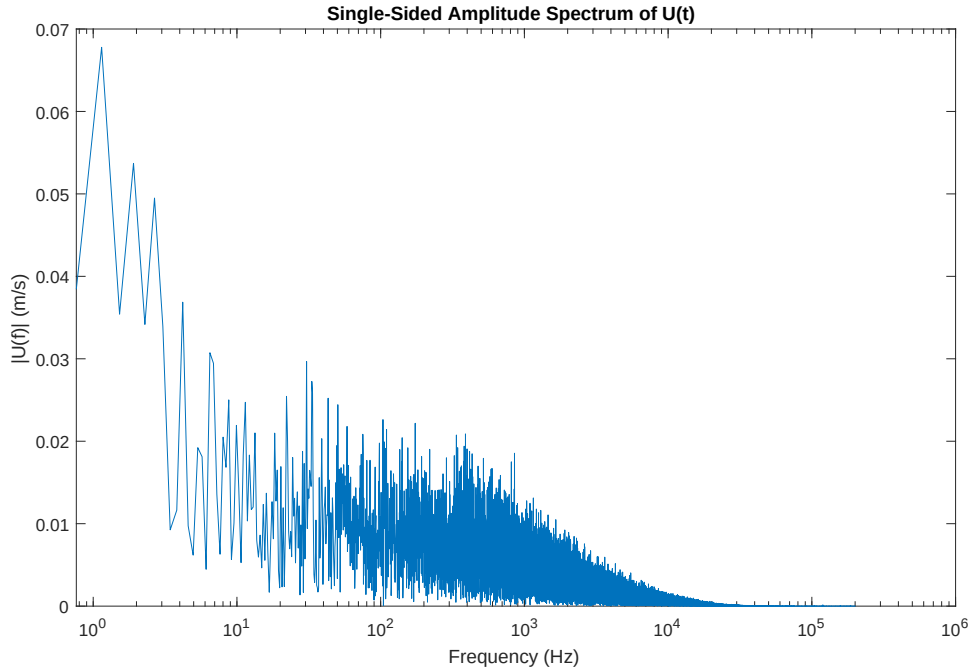

Figure B.3: the amplitude spectrum of the velocity.

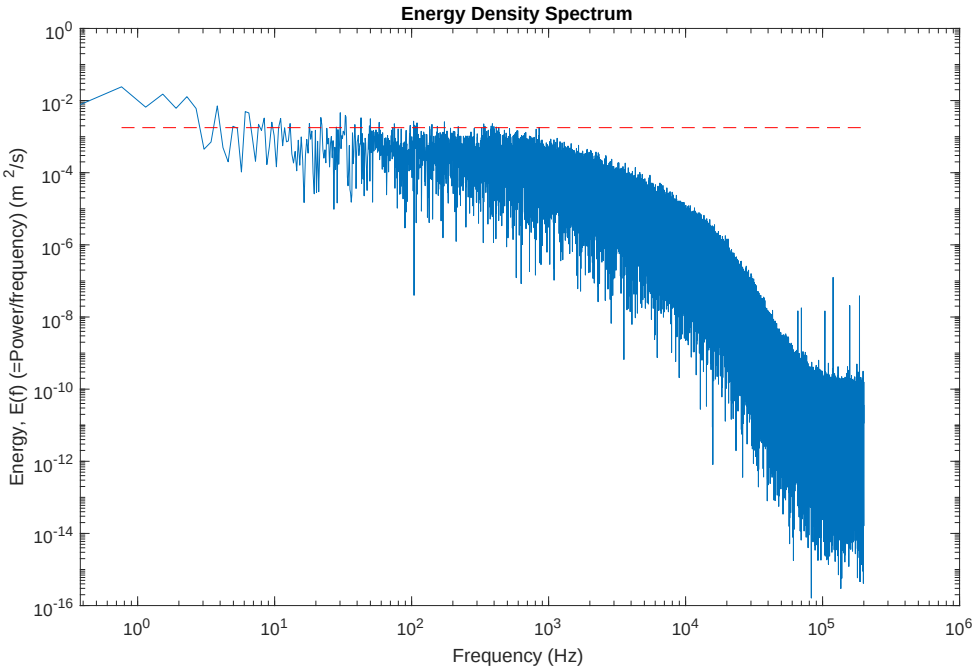

Figure B.4: The Energy density spectrum of velocity

MATLAB Script

```
% Read in the hot wire signal and process it to get velocity
U=vel(:,1,:)
% Plot the U-velocity trace
Fs=200000;          % Sampling frequency of 200 kHz
L=length(U);        % Number of samples
t=(0:L-1)/(Fs);     % Time vector
plot(t,U);          % Plot the velocity trace
title('U-velocity trace');
ylabel('U-velocity (m/s)');
xlabel('time (s)');

% Perform FFT analysis on the U-velocity signal and plot ...
    Amplitude spectrum
aFData=fft(U);                  % Take FFT of U signal
n=L/2;                          % FFT will yield half the ...
    number of unique points
aFreq=Fs*(1:n)/n;               % Frequency array (half the ...
    length of signal)
aFMag=abs(aFData(1:n)/L);       % Normalized Magnitude array ...
    (half the length of signal)
figure;
semilogx(aFreq(2:n),aFMag(2:n))  % Plot frequency against magnitude
title('Single-Sided Amplitude Spectrum of U(t)')
xlabel('Frequency (Hz)')
ylabel('|U(f)| (m/s)')
% Plot the energy density spectrum
Power=abs(fft(U)).^2/L;         %Power is the magnitude squared ...
    by L
Energy=Power/Fs;
Ef0=mean(Energy(2:100))
figure
loglog(aFreq,Energy(2:L/2+1))
hold on
X = Ef0 * ones(size(aFreq(2:n)));
```

```
plot(aFreq(2:n),X,'Color','red','LineStyle','--');
title('Energy Density Spectrum')
xlabel ('Frequency (Hz)')
ylabel ('Energy, E(f) (=Power/frequency) (m^{2}/s)')

% Calculate the integral length scale (macro scale) Roach Eqn 15
uprime=std(U)
uprimesquared=uprime^2;
Ubar=mean(U)
Tu=uprime/Ubar
IntegralLengthScale=Ef0*mean(U)/(4*uprimesquared)

% Calculate the dissipation length scale (micro scale) Roach Eqn 8
for i=1:length(aFreq)
Y(i)=aFreq(i)*aFreq(i)*Energy(i);
end
Z=trapz(aFreq,Y)            % Use trapezoid rule for integration
Z=Z*2*pi^2/(Ubar^2*uprimesquared);
DissipationScale=sqrt(1/Z)
```

APPENDIX C

C.1 Infrared (IR) Material Windows

Infrared (IR) Material Windows (Polymer Film) are moulded in an extremely thin and flexible 0.457 mm thickness, milky white plastic. The thin design consistent across the window surface, large apertures, and minimal thermal expansion coupled with low absorption from 8 - 14 μm make them ideal for a range of infrared applications.

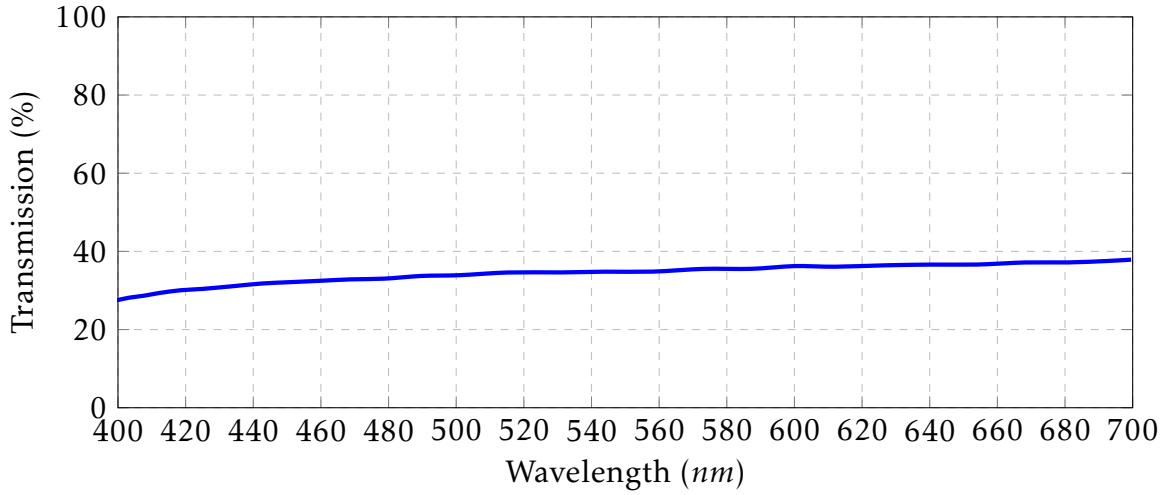

Figure C.1: IR windows in the visible spectrum [167].

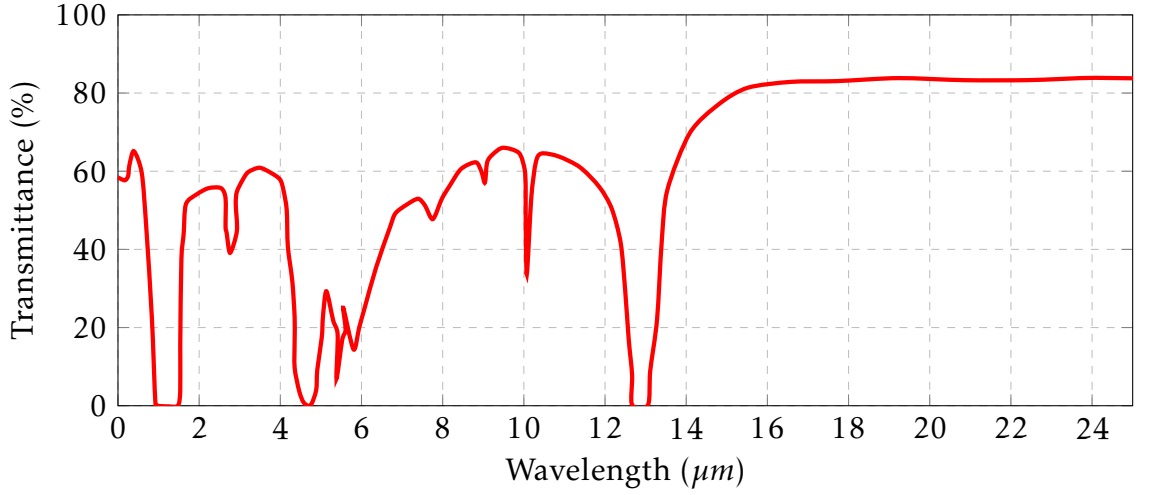

Figure C.2: IR windows in the IR spectrum [167]

C.2 Safe Operating Procedure

Starting up the Rig

1. Check connections, between the (Heat flux, Temperature, and Hot wire) sensors to Signal Box 1,2 and 3 for proper functioning.
2. Connect a Standard voltage source to the Centrifugal Fans and the Heater Transformer, Note the indicated power (zero) on the Heater multi-meter.
3. Align the heater rod in the required test cylinder and locate it at a fixed distance in the test section.
4. Record laboratory temperature and atmospheric pressure. Check manometer upright position.
5. Turn-on the Pico-logger and LabVIEW software in the selected lab computer.
6. Switch-on Heater Power, adjust the variable transformer to the desired voltage (max voltage 120 v).
7. Turn - On both switches (Switch Fan A) and (Switch Fan B) in a sequence. Wait till stabilization (about 5 min).
8. Allow about 1 hour for stabilization. Note, the steady-state read-out gives constant temperature value at cylinder surface.
9. Record the output signals for (Hot Wire for about 5 min, heat flux for about 3 min, and thermocouples).
10. Repeat the previous step for 180^o (increments of 10^o) around the cylinder.
11. Change the perforated plate.
12. Follow Steps (8) to (10) to obtain data for different free stream turbulence.
13. Set the gate valve, to control the fans flow-rate.
14. Follow Steps (8) to (13) till completion the range of mass flow rates.
15. Follow Steps (8) to (14) when changing the test cylinder (roughness).

Emergency Shut Down

1. Switch-off the Heater Power, adjust the variable transformer to the minimum voltage (zero volts).

2. Allow some time for heat dissipation from the test cylinder. Note, minimum read-out gives temperature value equal to ambient temp.
3. Turn-off the Pico-logger and LabVIEW software in the PC.
4. Turn-off both switches (Switch Fan A) and (Switch Fan B) in a sequence.
5. Shut down the computers following standard procedure in the Laboratory.